Ultrafast study of Dirac fermions in topological insulators

Lama Khalil

université PARIS-SACLAY

NNT : 2018SACLS344

Thèse de doctorat

UNIVERSITÉ PARIS SUD
Comprendre le monde, construire l'avenir

Ultrafast study of Dirac fermions in topological insulators

Thèse de doctorat de l'Université Paris-Saclay
préparée à l'Université Paris-Sud

Ecole doctorale n°564 Physique en Île-de-France (EDPIF)
Spécialité de doctorat : Physique

Thèse présentée et soutenue à Saint-Aubin, le 28 septembre 2018, par

LAMA KHALIL

Composition du Jury :

Claude PASQUIER Professeur, Université Paris-Sud (LPS)	Président
Christine RICHTER Professeur, Université de Cergy-Pontoise (LPMS)	Rapportrice
Andrea PERUCCHI Chercheur, Synchrotron ELETTRA	Rapporteur
Pascal MARTIN Maître de conférence, Université Paris-Diderot (ITODYS)	Examinateur
Marino MARSI Professeur, Université Paris-Sud (LPS)	Directeur de thèse
Amina TALEB-IBRAHIMI Directrice de recherche, Synchrotron SOLEIL	Co-directrice de thèse

To the memory of my father and to my mother

Acknowledgments

First of all, I would like to express my sincere and warm gratitude to my thesis director, Marino Marsi, for his valuable guidance and continuous support I received throughout the research work. I greatly appreciate the freedom and confidence he provided me. He was always present to answer my questions and discuss whenever I needed. The realization of this thesis would not have been possible without his essential intervention and insightful remarks.

My deep gratitude goes to my thesis co-director, Amina Taleb-Ibrahimi, who has been working from the shadows. Thanks for giving me advice, both on the scientific and personal level, which I markedly appreciated. I admire her exceptional kindness and true dedication to her work, which was a source of inspiration to me.

I am delighted to have defended my Ph.D. in front of: Claude Pasquier, Christine Richter, Andrea Perucchi and Pascal Martin. I would like to thank them for being members of my thesis committee, for their presence, and for their contribution to this manuscript.

I sincerely wish to thank the FemtoARPES team members. In particular, I express my special thanks to Evangelos Papalazarou for always been willing to help me out with pump-probe experiments and data analysis. I thank him for his help, as well as for his humor and kindness. In addition, I would like to acknowledge Luca Perfetti for sharing with me his knowledge and for the fruitful discussions we had, which made me admire his motivation and his enthusiasm for his research work.

My thanks are extended to the director of the Laboratoire de Physique des Solides, Sylvain Ravy, and the "Lumière Ultrabrève, Cohérence et Electrons" team, namely, Antonio Tejeda, Vincent Jacques, David Le Bolloc'h, Nicolas Moisan and Luc Ortega for their interesting discussions, as well as for the casual day to day conversations at lunch time.

I am very thankful for Marcin Konczykowski (Laboratoire des Solides Irradiés) for providing the bismuth telluride samples that were studied in chapter 4 and for the transport measurements that he performed during this thesis work. I also acknowledge the collaboration with Lia Krusin-Elbaum (CUNY, New York).

During these years of Ph.D., I spent a fair amount of time at the Elettra synchrotron. I would like to thank Alexey Barinov for his help during the experimental work that I

performed on the Spectromicroscopy beamline. I am also grateful to the permanent staff of the APE beamline, Ivana Vobornik and Jun Fujii, for their technical support and their helpful discussions.

My warm thanks are further going to the past and present doctoral and post-doctoral colleagues in the lab. In particular, I thank Niloufar Nilforoushan for her unending support and help that meant a lot to me, especially during the tough times. Nilou, I cannot thank you enough for your presence, encouragement and friendship that, believe me, are very precious to me. You were not just a colleague but also a real friend. I am also thankful to Min-I Lee, Isabel Gonzalez-Vallejo, Maya Narayanan and Arlensiú Celis for all the support, the cheerful moments inside and outside the lab, and the insightful conversations that most of the time had nothing to do with physics. I am grateful to Marco Caputo for the many helpful and fruitful discussions, especially during beamtimes at Elettra. I thank Emilie Tisserond, Jonathan Caillaux and Ewen Bellec for the interesting discussions. You made my stay at LPS very pleasing.

My heartfelt gratefulness also goes to my amazing Lebanese friends in France. In particular, I am infinitely thankful to Claude, Hanane, Bakhos and Charbel for their endless love and support in all times. I thank you all for your great spirit and kind heart that made me see the beauty in everything around me. Words cannot describe how dear you are to me. I will never forget that you have been there during my ups and downs. I also thank Perla, Rami, Elie, Joe and Layal for their support and for the wonderful moments we spent together. My special gratitude is extended to Hanne Yammine who was my mother in France. Everything you did has made me feel at home when home was so far away. Thank you all for being my family in France.

Finally, my biggest and warmest gratitude goes to my beloved parents, brother and sisters, Elias, Lana, Elio, Monica and Andrea, to whom I dedicate this Ph.D. Your unwavering support has given me strength to succumb the challenges that I have faced in my life. Without your unconditional love, endless sacrifices, generosity on all levels, faith in me, encouragement for me to pursue my dreams, protection, patience and kindness I would not be where I am today. To my father, to whom I promised to dedicate this thesis before he left this world, I want you to know that I love you from the bottom of my heart and I am proud to be your daughter in a way beyond words can ever describe! Thank you Dad!

Lama KHALIL
Orsay, September 2018

List of publications

1. E. Tisserond, N. Nilforoushan, M. Caputo, P. Alemany, E. Canadell, **L. Khalil**, I. Vobornik, J. Fujii, P. K. Das, C. Mézière, P. Batail, J.-P. Pouget, C. Pasquier, M. Marsi, and M. Monteverde, *"Electronic structure of the α-(BEDT-TTF)$_2I_3$ surface by photoelectron spectroscopy"*, (submitted).

2. **L. Khalil**, E. Papalazarou, M. Caputo, N. Nilforoushan, L. Perfetti, A. Taleb-Ibrahimi, M. Konczykowski, A. Hruban, A. Wołoo, L. Krusin-Elbaum, and M. Marsi, *"Bulk defects and surface state dynamics in topological insulators: the effects of electron beam irradiation on the ultrafast relaxation of Dirac fermions in Bi_2Te_3"*, (submitted)[1].

3. E. Papalazarou, **L. Khalil**, M. Caputo, L. Perfetti, N. Nilforoushan, H. Deng, Z. Chen, S. Zhao, A. Taleb-Ibrahimi, M. Konczykowski, A. Hruban, A. Wołoo, A. Materna, L. Krusin-Elbaum, and M. Marsi, *"Unraveling the Dirac fermion dynamics of the bulk-insulating topological system Bi_2Te_2Se"*, Phys. Rev. Mater. 2, 104202 (2018).

4. M. Caputo, **L. Khalil**, E. Papalazarou, N. Nilforoushan, L. Perfetti, A. Taleb-Ibrahimi, Q. D. Gibson, R. J. Cava, and M. Marsi, *"Dynamics of out-of-equilibrium electron and hole pockets in the type-II Weyl semimetal candidate WTe_2"*, Phys. Rev. B 97, 115115 (2018).

5. **L. Khalil**, E. Papalazarou, M. Caputo, N. Nilforoushan, L. Perfetti, A. Taleb-Ibrahimi, V. Kandyba, A. Barinov, Q. D. Gibson, R. J. Cava, and M. Marsi, *"Electronic band structure for occupied and unoccupied states of the natural topological superlattice phase Sb_2Te"*, Phys. Rev. B 95, 085118 (2017)[2].

6. M. Caputo, M. Panighel, S. Lisi, **L. Khalil**, G. Di Santo, E. Papalazarou, A. Hruban, M. Konczykowski, L. Krusin-Elbaum, Z. S. Aliev, M. B. Babanly, M. M. Otrokov, A. Politano, E. V. Chulkov, A. Arnau, V. Marinova, P. K. Das, J. Fujii, I. Vobornik,

[1] Results are presented in chapter 4 of this thesis.
[2] Results are presented in chapter 5 of this thesis.

L. Perfetti, A. Mugarza, A. Goldoni, and M. Marsi, *"Manipulating the Topological Interface by Molecular Adsorbates: Adsorption of Co-Phthalocyanine on Bi_2Se_3"*, Nano Lett. 16, 3409 (2016).

7. **L. Khalil**, C. Eid, M. Bechelany, N. Abboud, A. Khoury, and P. Miele, *"Design of $CoFe_2O_4$/Co_3O_4 nanofibers with tunable morphology by Electrospinning"*, Mater. Lett. 140, 27 (2015).

Contents

Acknowledgments **i**

List of publications **iii**

1 Introduction **1**

2 Topological matter **5**

2.1 Birth of a new quantum state in condensed matter physics 5

2.2 Quantum Hall effect 7

2.3 2D topological insulators 9

2.3.1 Quantum spin Hall effect 9

2.3.2 $\mathbb{Z}_2$ topological insulators 11

2.3.3 HgTe/CdTe quantum wells: the first 2D topological insulator . . . 14

2.4 3D topological insulators 18

2.4.1 From 2D to 3D topological insulators 18

2.4.2 $Bi_{1-x}Sb_x$: the first 3D topological insulator 21

2.4.3 Bi_2Te_3: a 3D topological insulator 23

2.5 Conclusion 28

3 Experimental techniques based on photoemission spectroscopy **29**

3.1 Photoemission spectroscopy (PES) 29

3.2 X-ray photoemission spectroscopy (XPS) 31

3.2.1 Fundamental concepts 31

3.2.2 XPS spectral features 32

3.2.3 Synchrotron radiation 34

3.2.4 XPS on the APE beamline at Elettra 39

3.3 Angle-resolved photoemission spectroscopy (ARPES) 40

3.3.1 Fundamental concepts 40

3.3.2 Three-step model 43

3.3.3 Experimental aspects 47

3.4 Time-resolved ARPES (trARPES) . . . 49
3.4.1 Fundamental concepts . . . 49
3.4.2 FemtoARPES setup . . . 51
3.4.3 Ultrafast carrier dynamics . . . 52
3.5 Scanning photoemission microscopy (SPEM) . . . 58
3.5.1 Fundamental concepts . . . 58
3.5.2 SPEM on the Spectromicroscopy beamline at Elettra . . . 58
3.6 Conclusion . . . 60

4 Bulk defects and surface state dynamics in Bi_2Te_3 61
4.1 Bulk-insulating topological insulators . . . 61
4.1.1 Low irradiation dose . . . 63
4.1.2 High irradiation dose . . . 64
4.2 Technique and experimental details . . . 66
4.3 Spectral effects of the induced bulk defects . . . 66
4.4 Dynamical effects of the induced bulk defects . . . 67
4.4.1 Ultrafast relaxation regime . . . 68
4.4.2 Long lasting relaxation regime . . . 74
4.4.3 Visualization of the two relaxation regimes . . . 75
4.5 Tuning the topological surface state dynamics . . . 75
4.6 Conclusion . . . 77

5 Electronic band structure for occupied and unoccupied states of Sb_2Te 79
5.1 Natural topological superlattices . . . 79
5.2 Technique and experimental details . . . 82
5.3 Occupied electronic band structure . . . 82
5.3.1 Imaging study . . . 82
5.3.2 μ-XPS study . . . 84
5.3.3 μ-ARPES study . . . 84
5.3.4 XPS study . . . 87
5.4 Unoccupied electronic band structure . . . 90
5.5 Bulk contribution . . . 95
5.6 Conclusion . . . 97

6 Conclusion and perspectives 99

A Résumé étendu en français 101

Bibliography 107

Chapter 1

Introduction

The complexity of certain materials is reflected by the appearance of unconventional electronic states, possessing fascinating and emergent properties, that could contribute to answering major societal challenges of the 21^{st} century related to electronics, energy and environment. Today, understanding these complex systems remains a challenge for the scientific community. However, since the beginning of the 20^{th} century, the electronic properties of the materials have been at the heart of condensed matter physics problems and have been the subject of intense investigations: the Drude model and the band theory by Wigner, Seitz and Bloch. These properties involve not only the electrons, and hence the orbitals and spins, but also all the charges of the system and more generally the atomic lattice. All these degrees of freedom of matter and their couplings should be taken into account to understand the electronic properties. This makes the problem extremely complex. Today, we understand the properties of conventional materials such as copper, silicon and diamond, classified according to their conducting, semiconducting and insulating band structures. The challenge now is to understand complex systems with unconventional electronic states like those observed in the presence of strong electron correlations, or also because of topological effects.

Unconventional electronic states in compounds without electronic correlations are observed in the presence of surface and interface effects. For example, since 2005, it has been predicted theoretically and then verified experimentally that certain systems have "topological" phases, insulating in the bulk but supporting metallic surface states. These surface states are spin polarized, and are very robust in the presence of nonmagnetic impurities. These systems are called topological insulators and can appear in massive materials like bismuth telluride Bi_2Te_3, but also in superlattices such as diantimony tellurium Sb_2Te.

The presence of metallic surfaces on an insulator, with a special topological protection, is a new phenomenon and is not found in other materials. There are many ideas and

suggestions for future applications for these metallic surfaces ranging from spintronics to quantum computation [1]. But before these applications can be realized, many fundamental questions remain to be answered, and problems to be resolved. The main challenge in electrical utilization of the surfaces is that the interior of a topological insulator is often not nearly as insulating as predicted. Owing to a multitude of electrically active crystal defects, the interior is often so conductive that electrical current passes not only through the metallic surfaces but through the entire material, preventing many potential applications. This problem is one of the main challenges to be overcome by employing new approaches such as irradiation by high-energy electron beams, which allows to compensate the crystal defects responsible for the conductivity of the bulk. More recently, an experimental study has proved that the bulk conductivity in the three-dimensional topological insulator Bi_2Te_3 can be decreased by orders of magnitude to the charge neutrality point by the controlled use of ($\sim$2.5 MeV energy) electron beams [2]. Consequently, irradiation with electron beams is a very promising approach to obtain bulk-insulating topological insulators.

Moreover, possible applications depend on the ability to control and engineer the electronic band structure of the topological surface states. In this context, it has been proposed that multilayer heterostructures, made of an ordered stacking sequences of topological insulators interlaced with other compounds, sandwiched in a superlattice, present new topological properties. Recently, a theoretical and experimental study has demonstrated the possibility of topological surface state band structure engineering in the naturally occurring homologous series of topological superlattices $(Sb_2)_m$-Sb_2Te_3, composed of an ordered stacking of integer numbers of Sb_2 bilayers and Sb_2Te_3 quintuple layers [3]. The results have revealed that the topological states are remarkably robust and that their dispersion can be tuned in the explored range (m = 0–3). Therefore, these materials provide an exciting avenue to engineer the topological states, which is a crucial requisite for realizing different quantum phenomena and spintronics applications.

The work of this thesis aims at studying the unconventional electronic states of two topological materials, namely, the irradiated topological insulator Bi_2Te_3 and the natural topological superlattice phase Sb_2Te, which constitutes the most representative material in the topological superlattice series $(Sb_2)_m$-Sb_2Te_3 (m = 2). Both systems were investigated by techniques based on photoemission spectroscopy, which represents a powerful experimental method to directly visualize the electronic band structure in solids. In this thesis, I will present a photoemission study mainly via two modalities: the first one is time- and angle-resolved photoemission spectroscopy (trARPES) employed to investigate the unoccupied topological surface states of the irradiated Bi_2Te_3 and Sb_2Te; the second one is scanning photoemission microscopy (SPEM) used to assess the heterogeneity of

the cleaved surface of Sb_2Te by comparing the electronic structure in regions possessing different surface terminations. In addition, the X-ray photoemission spectroscopy (XPS) was also used to probe the Sb_2Te core levels in order to reveal the significant importance of the SPEM study.

The manuscript is structured as follows:

Chapter 2 provides an introduction to the physics of topological insulators. I first describe the two-dimensional topological insulators to later discuss the three-dimensional state. In particular, I present previous experimental and theoretical studies on the three-dimensional system Bi_2Te_3, which is the investigated material in this thesis.

Chapter 3 describes the experimental techniques, based on photoemission spectroscopy, and instruments employed in the frame of this work to investigate the electronic properties of the studied topological materials. Specifically, I present the basic principles of XPS, angle-resolved photoemission spectroscopy (ARPES), trARPES and SPEM and emphasize the importance of synchrotron radiation sources in the development of high spatial resolution photoemission spectroscopy techniques.

Chapter 4 presents a trARPES study of a series of Bi_2Te_3 samples in various conditions of electronic irradiation. Thanks to the combination of time, momentum and energy resolution, my results show the influence of the swift electron irradiation on the scattering and carrier relaxation dynamics in response to ultrafast optical excitation.

Chapter 5 investigates the occupied and unoccupied electronic band structure of the natural topological superlattice phase Sb_2Te by means of SPEM, XPS and trARPES. By combining these techniques, I provide a clear evidence of the coexistence of distinct terminations on the same cleaved surface and a precise description of their electronic properties.

Chapter 6 summarizes the results in a general conclusion while proposing future perspectives for further experiments and theoretical revisions.

Chapter 2

Topological matter

Topological insulators are electronic materials that have a bulk bandgap like an ordinary insulator but possess protected conducting states on their edge or surface. These states are possible due to the combined action of spin-orbit coupling and of time-reversal symmetry. The two-dimensional topological insulator is a quantum spin Hall insulator. A three-dimensional topological insulator supports novel spin-polarized two-dimensional Dirac fermions on its surface. In this chapter, I provide an overview on the two- and three-dimensional topological insulators. Transport experiments on HgTe/CdTe quantum wells are described that demonstrate the existence of the edge states predicted for the quantum spin Hall insulator. Experiments on $Bi_{1-x}Sb_x$, and Bi_2Te_3 are then discussed that establish these materials as three-dimensional topological insulators and directly probe the topology of their surface states.

2.1 Birth of a new quantum state in condensed matter physics

In the quantum world, atoms and their electrons can constitute diverse phases of matter, such as crystalline solids, magnets and superconductors. A recurring subject in condensed matter physics has been the classification of these phases by the principle of spontaneous symmetry breaking [4], using Landau's approach. For the previous examples, the translational, rotational and gauge symmetries are respectively broken. All these examples have in common that at high temperatures the physical system is in a disordered phase. Upon decreasing the temperature, the system acquires order due to spontaneous symmetry breaking below a critical temperature T_c [5]. Before 1980, all states of matter in condensed matter systems were classified by the principle of broken symmetry. However, in 1980, von Klitzing *et al.* [6] discovered the first example of a quantum state that does

not exhibit any symmetry breaking: the integer quantum Hall state. In this quantum state, the sample, possessing an insulating bulk, present unidirectional electric current carried only along the edges of the sample. The circulating edge states of the quantum Hall state are different from ordinary states of matter because they persist even in the presence of disorder. In addition, the flow of this unidirectional current gives rise to a quantized Hall effect in which the Hall conductance takes quantized values. In 1982, Thouless and coworkers [7] showed that the precise quantization of the Hall conductance is described by the fact that it is a topological invariant, which can only take integer values in units of e^2/h (e is the electric charge and h is the Planck constant), independent of the material details. The concept of topological invariance was introduced by the mathematicians to classify distinct geometrical objects into wide classes. For example, two-dimensional (2D) surfaces are classified by the number of holes in them, or genus. For instance, the surface of a perfect sphere is topologically identical to the surface of an ellipsoid, since these two surfaces can be smoothly deformed into each other without creating any holes. Similarly, a coffee cup is topologically equivalent to a doughnut, since both of them contain a single hole (see figure 2.1). In mathematics, topological classification focuses on the fundamental variation of geometrical shapes. In physics, precisely quantized physical quantities, such as the Hall conductance, also have a topological origin and are insensitive to small changes in the material [8]. Therefore, the study of the quantum Hall effect has led to a classification paradigm based on the notion of *topological order*.

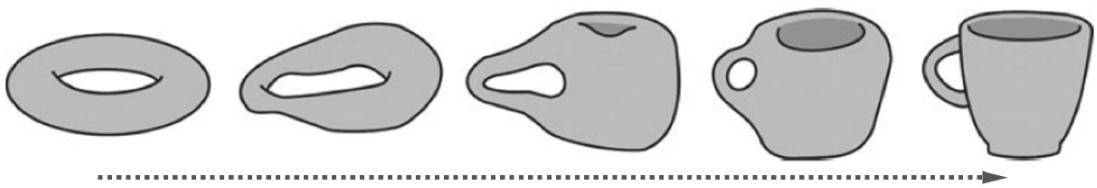

Figure 2.1: A doughnut transforming into a coffee cup via smooth deformations. Both of them possess a single hole.

The quantum Hall experiments require specific conditions: sufficiently low temperatures and strong magnetic fields. Consequently, the quantum Hall states belong to a topological class which explicitly breaks the time reversal symmetry by the presence of the magnetic field. Although Haldane [9] constructed a model of the quantum Hall effect without an external magnetic field, such state still breaks the time reversal symmetry. More recently, a new class of topological states has emerged, called quantum spin Hall states or topological insulators, which is time reversal invariant and does not require an

applied field. This 2D class of materials is topologically different from all other states of matter, including the quantum Hall states, and has been theoretically predicted [10] and experimentally observed in mercury telluride quantum wells [11, 12]—the first experimentally realized quantum spin Hall state. Quantum spin Hall systems belong to a class where the spin-orbit coupling plays a crucial role[1]. These systems are insulating in the bulk—they have an energy gap separating the valence and conduction bands—but they present robust conducting edge states that are topologically protected and immune to impurities. In 2007, a three-dimensional (3D) form of the topological insulator with conducting surface states was predicted by Fu and Kane [13] in the $Bi_{1-x}Sb_x$ alloy in which the spin-orbit interactions are large. Soon after, angle-resolved photoemission spectroscopy (ARPES) measurements of the surface of $Bi_{1-x}Sb_x$ supported this picture [14], indicating that $Bi_{1-x}Sb_x$ is the first experimental realization of a topological insulator in three dimensions and that its topological surface is a metal in two dimensions. Then, 3D topological insulators were theoretically predicted in Bi_2Te_3, Sb_2Te_3 [15] and Bi_2Se_3 [15, 16] compounds. Note that these systems possess gapless topological surface states with a single Dirac cone, while they are narrow-band semiconductors in the bulk. The Dirac-type linear energy-momentum electronic dispersion of these surface states was indeed observed by means of ARPES experiments [16, 17, 18]. These pioneering theoretical and experimental studies opened up the exciting field of topological insulators, and the field is now expanding at a rapid pace. Therefore, the discovery of the topological insulators has revolutionized modern condensed matter physics.

In the following section, I will describe the quantum Hall effect to later discuss the quantum spin Hall effect.

2.2 Quantum Hall effect

In 1980, von Klitzing *et al.* [6] discovered the quantum Hall effect, which can be considered as the mother state of all topological states of matter. The quantum Hall effect takes place when electrons confined to two dimensions are subject to a strong magnetic field at low temperature. While Drude theory predicts a linear dependence of the transverse resistivity on the magnetic field strength, at sufficiently low temperatures and strong magnetic fields plateaus were observed instead (see figure 2.2). The resulting system is a bulk insulator, being reflected in a vanishing longitudinal conductivity $\sigma_{xx} = 0$. At the same time, unlike an insulator, the transverse or Hall conductivity σ_{xy} is quantized [5]:

$$\sigma_{xy} = n\frac{e^2}{h}, \quad n \in \mathbb{Z} \tag{2.1}$$

[1] Spin-orbit effects take the role of an external magnetic field.

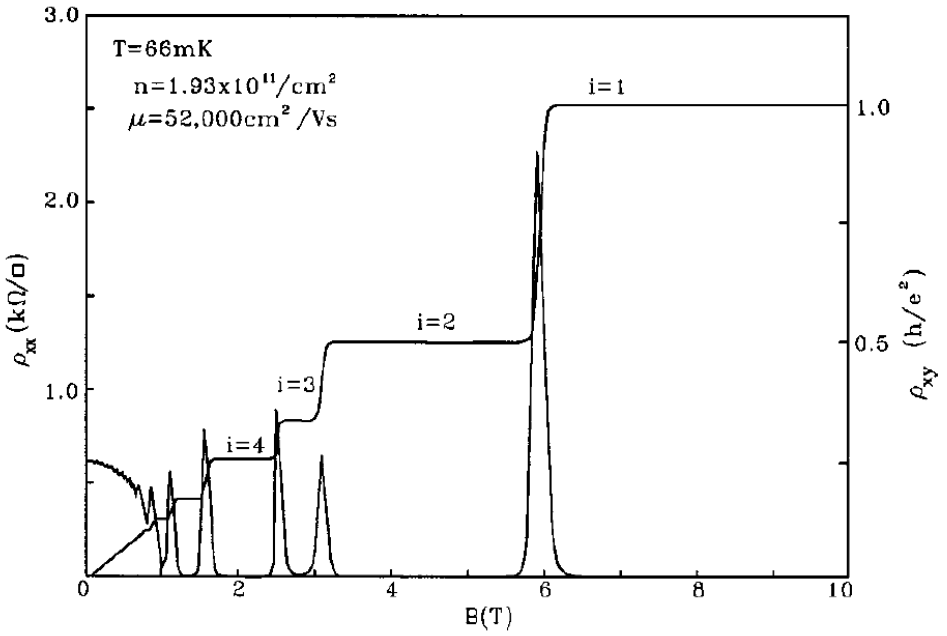

Figure 2.2: Magnetotransport coefficients ρ_{xx} and ρ_{xy} versus the magnetic field B for a relatively low mobility 2D electron gas in $GaAs/Al_xGa_{1-x}As$. The plateaus in ρ_{xy} are quantized in the natural conductance unit e^2/h with integer quantum numbers ($i = n =$ 1,2, 3...), while ρ_{xx} is equal to zero at these plateaus. From [19].

where $\mathbb{Z}$ denotes the integers, e is the electric charge and h is the Planck constant. Note that n is a topological invariant known as the Chern number. The quantization of σ_{xy} has been measured to 1 part in 10^9. This accuracy is a manifestation of the topological nature of σ_{xy}. Since the system is insulator in the bulk, the finite Hall conductivity must be related to the edge transport. In fact, the integer number n corresponds to the number of chiral edge modes where each mode carries a unit of conductance e^2/h.

A semi-classical approach of the magnetic field effect on a 2D electron gas is shown in figure 2.3. In the absence of an electric field, the electrons are forced to follow closed circular orbits when placed in a magnetic field, unless they meet an interface with an insulator, e.g. the vacuum, on which they will be reflected. This will make them follow the edges of the sample. This approach makes it possible to visualize the notion of edge channels generated by the quantum Hall effect.

The quantization of the electrons' circular orbits, with cyclotron frequency ω_c, leads to quantized Landau levels with energy $E_m = \hbar\omega_c\,(m + 1/2)$ (m = 0, 1, 2,...). How to connect the semi-classical approach to the Landau levels? The electrons that participate in the electrical conduction are those located at the Fermi level. Figure 2.4(a) represents the distribution of the Landau levels, separated by the same energy $\hbar\omega_c$, filled under

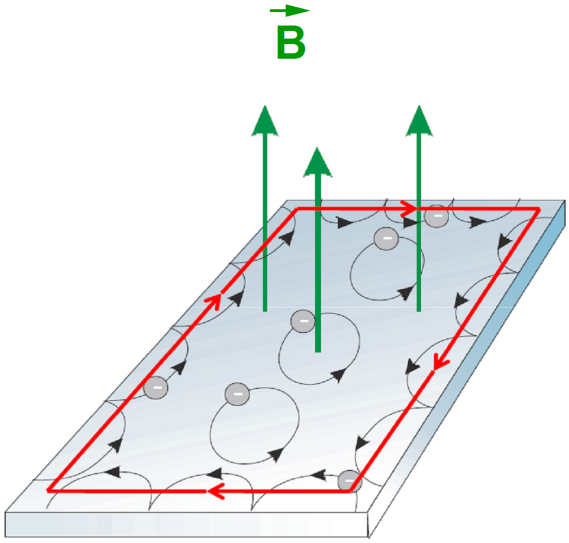

Figure 2.3: The magnetic field effect on a 2D electron gas.

the Fermi energy and empty above. None of the Landau levels crosses the Fermi level. Therefore, none of them participates in the conduction. However, this approach is valid only far from the edges of the material. Let us now consider a conductor delimited by an insulator on the boundaries at x_1 and x_2. A confinement effect has to be taken into account, which makes the Landau levels at $E_m = \hbar\omega_c(m+1/2)$ strongly bent upwards near the edges of the sample [20]. As a consequence, the Landau levels below the Fermi level cross the latter at the edges of the sample and thus bring electrons to the Fermi level, producing edge channels that participate in the conduction (see figure 2.4(b)).

As shown in figure 2.3, the edge channels are unidirectional, i.e. an electron can travel only in one direction. No backscattering due to the presence of impurities is allowed [21]. This leads to a protection of the edge channels.

2.3 2D topological insulators

2.3.1 Quantum spin Hall effect

In the quantum Hall effect, the spin of the electrons was not taken into account. Let us now take figure 2.3 and let us modify it in order to relate the spin to the direction of propagation of the electrons (as shown in figure 2.5). If we consider a 2D electron gas with all spins up (figure 2.5, right), placed in a magnetic field directed upwards, a quantum Hall effect will occur, generating edge channels all circulating in the same direction. Similarly, when the electron gas undergoes a magnetic field directed downwards, all edge channels will

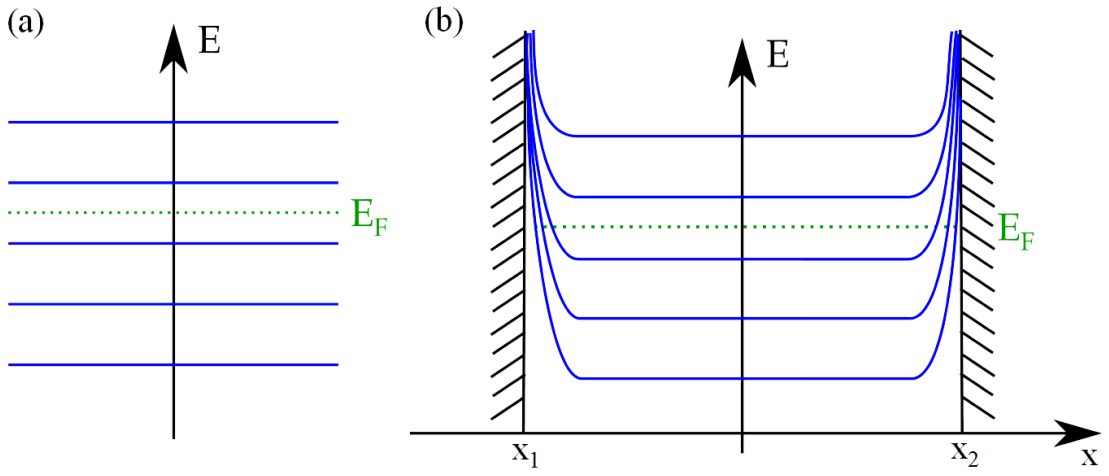

Figure 2.4: Energy spectrum of the Landau levels. (a) The Landau levels are separated by an energy $\hbar\omega_c$ away from the edges of a 2D electron gas subjected to a strong perpendicular magnetic field. (b) Landau levels are bent upwards at the edges of the sample due to the confinement. They cross the Fermi level, opening conduction channels at the edges of the specimen.

rotate in the opposite direction with respect to the previous spin current (figure 2.5, left). By superposing these two images, we obtain the quantum spin Hall effect, which can be thought of as the spin counterpart to the classical "charge" Hall effect. Roughly speaking, the quantum spin Hall state can be viewed as two copies of the quantum Hall state with opposite spins, magnetic fields and Hall conductances. Obviously, it is impossible to apply an external magnetic field acting only on a specific type of spin. Nevertheless, this effect can be obtained without an external magnetic field in materials composed of heavy atoms with a strong spin-orbit coupling, which constitutes the key ingredient in the quantum spin Hall effect. In fact, due to the strong spin-orbit coupling, the electrons are subject to an effective magnetic field depending on their spin, which generates the quantum spin Hall effect. In contrast to the quantum Hall effect, which breaks the time reversal symmetry due to the applied magnetic field, the quantum spin Hall effect does not break the time reversal symmetry.

Are the channels still protected as in the case of the quantum Hall effect? In fact, the channels propagating in opposite directions are spatially close, and one can imagine that an electron can diffuse from one channel to another by an impurity. This is not possible. Figure 2.6 illustrates why single-particle backscattering is forbidden. One should note that in the quantum spin Hall state, spin and wave vectors are locked, i.e. their directions are strongly related to each other. Since the spin and the wave vector are perpendicular, when an electron goes around an impurity to reverse its direction, both its wave vector

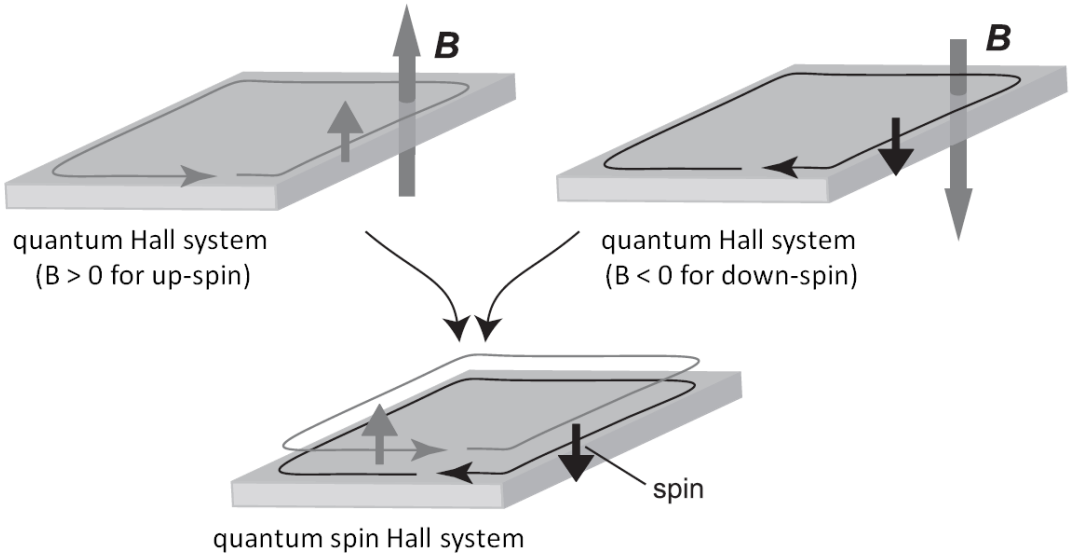

Figure 2.5: The superposition of two quantum Hall systems generates a quantum spin Hall system. From [22].

and its spin rotate by an angle of π. As illustrated in figure 2.6, an electron in the quantum spin Hall edge state can take either a clockwise or a counterclockwise turn around the impurity, and during that turn, the spin rotates by an angle of π or -π to the opposite direction, respectively. As a consequence, the two paths, related by the time reversal symmetry, differ by a full π-(-π) = 2π rotation of the electron spin, i.e. the phase difference between the two paths is a full 2π rotation of the electron spin. However, the wave function of a spin-1/2 particle acquires a minus sign under a full 2π rotation. Thus, the two backscattering paths, related by time reversal symmetry, always interfere destructively, leading to a perfect transmission. If the impurity carries a magnetic moment, the time reversal symmetry is broken and the two reflected waves no longer interfere destructively. In this way, the robustness of the quantum spin Hall edge state is protected by the time reversal symmetry [23].

2.3.2 $\mathbb{Z}_2$ topological insulators

The quantum spin Hall system, described in the preceding paragraph, has a single pair of edge states (a forward and a backward moving channel). If we assume that there are two pairs of edge states in the system, i.e. two forward movers and two backward movers on a given edge, then an electron can be scattered from a forward to a backward moving channel without reversing its spin. This spoils the destructive interference described previously and leads to dissipation. Therefore, to get a robust quantum spin Hall state, the

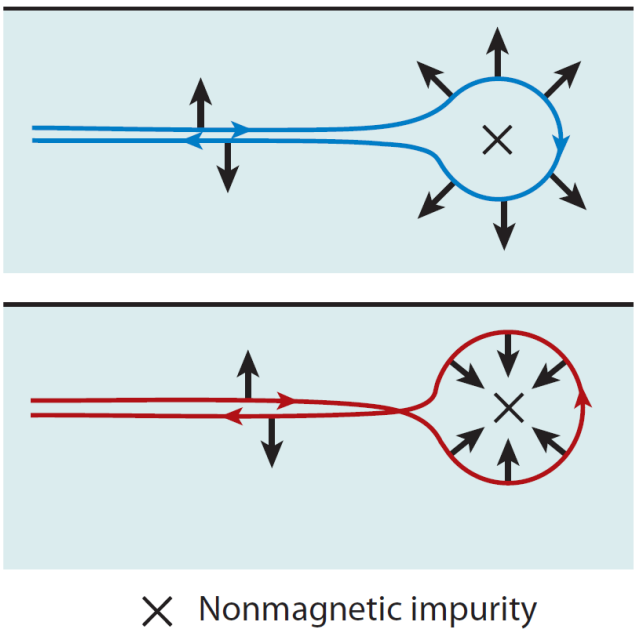

Figure 2.6: A quantum spin Hall edge electron can be scattered in two possible paths by a nonmagnetic impurity. Going clockwise along the blue curve, the spin rotates by π; counterclockwise along the red circle, by -π. A geometrical phase factor related to the rotation of the spin leads to a destructive interference between the two paths—the backscattering of electrons on the quantum spin Hall edges is suppressed. From [24].

edge states must have an odd number of forward movers and an odd number of backward movers. This even-odd effect, characterized theoretically by a so-called $\mathbb{Z}_2$ topological quantum number [25, 26] (which is also used for 3D topological systems[2]), is at the heart of the quantum spin Hall state. For this reason, the quantum spin Hall insulator is also referred to as a topological insulator.

The alternative way to understand the qualitative difference between an even or odd number of edge states is given in terms of Kramers' theorem. This theorem states that: *"For a system which is time-reversal symmetric and composed of an odd number of particles with half-integer spins, there are at least two degenerate states."*
The proof goes as follows. Consider the eigenvalue problem:

$$\hat{H} \mid E_n \rangle = E_n \mid E_n \rangle. \tag{2.2}$$

If the Hamiltonian commutes with the time reversal operator $[\hat{T}, \hat{H}] = 0$, there are two eigenstates $\{ \mid E_n \rangle, \hat{T} \mid E_n \rangle \}$ for the energy E_n. I will show that these are distinct states.

[2] A 3D topological insulator is characterized by four $\mathbb{Z}_2$ topological numbers.

If the two states were the same, they would differ at most by a phase factor:

$$\hat{T} \mid E_n \rangle = e^{i\delta} \mid E_n \rangle, \tag{2.3}$$

hence,

$$\hat{T}^2 \mid E_n \rangle = \hat{T} e^{i\delta} \mid E_n \rangle = e^{-i\delta} \hat{T} \mid E_n \rangle = \mid E_n \rangle. \tag{2.4}$$

However, since $\hat{T}^2 = -1$[3]:

$$\hat{T}^2 \mid E_n \rangle = - \mid E_n \rangle. \tag{2.5}$$

This is a contradiction to the assumption that $\mid E_n \rangle$ is an eigenstate (in particular, it is nonzero). Consequently, every energy eigenvalue is at least twice degenerate in the presence of time reversal symmetry and the corresponding eigenkets are orthogonal. Note that the two distinct degenerate states connected by time-reversal symmetry form a so-called Kramers pair, i.e. the two counterpropagating edge states at each boundary with opposite spin-polarization. In addition, the scattering probability of a state into its Kramers partner for a time reversal Hamiltonian is zero. However, $\mid E_n \rangle$ is a single particle state. For a two-particle state, such property has no reason to hold. If we stick to single-particle description as in band theory, a state described by the product of an even number of single particle excitations has in general a non-zero scattering amplitude into its time reversal partner.

Time reversal symmetry and the resulting Kramers' theorem have consequences on the electronic band structure of the material. In figure 2.7, the electronic states of a time reversal invariant 2D insulator as a function of the wave vector k_x along the edge are shown. Only half of the Brillouin zone $0 < k_x < \pi/a$ is represented because time reversal symmetry implies that the other half $-\pi/a < k_x < 0$ is a mirror image. The shaded regions depict the bulk conduction and valence bands separated by an energy bandgap. Depending on the details of the Hamiltonian near the edge, there may or may not be states bound to the edge inside the gap. If they are present, the Kramers' theorem requires that they are twofold degenerate at the time reversal invariant wave vectors $k_x = 0$ and $k_x = \pi/a$; these two special points are labeled $\Gamma_{a,b}$. Away from these two specific points, a spin orbit interaction will split the degeneracy. There are two ways by which the states at Γ_a and Γ_b can connect. As one can see in figure 2.7(a), they connect pairwise. In this case, the edge states can be eliminated by pushing all of the bound states out of the gap, and the bands intersect the Fermi level E_F an even number of times between $k_x = 0$ and $k_x = \pi/a$. On the contrary, in figure 2.7(b) the edge states cannot be eliminated, and the bands intersect the

[3]The time reversal operator is an antiunitary operator that squares to (+1) in the case of integer total angular momentum and (-1) in the case of half integer total angular momentum. In our case, we are interested in spin-1/2 fermions. Therefore, $\hat{T}^2 = -1$.

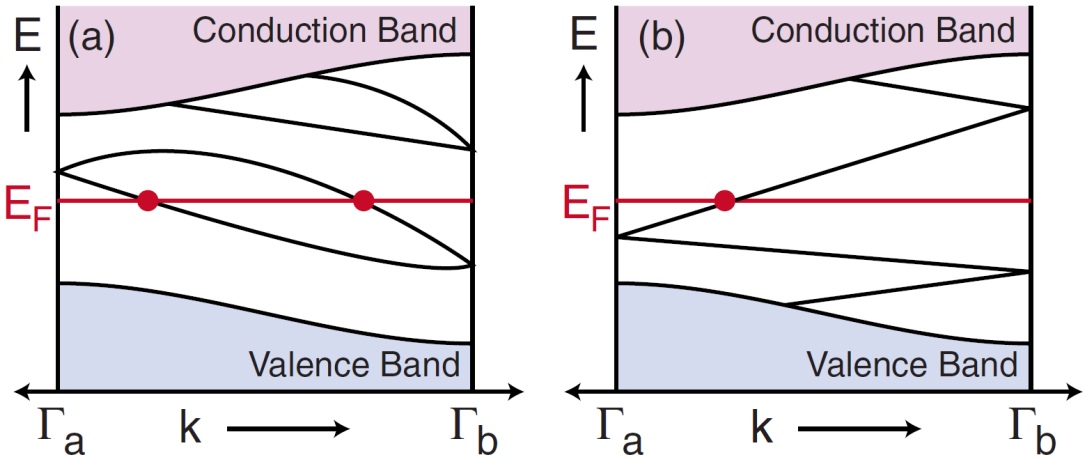

Figure 2.7: Electronic dispersion between two boundary Kramers degenerate points Γ_a = 0 and $\Gamma_b = \pi/a$. In (a) the number of surface states crossing the Fermi energy E_F is even, while in (b) it is odd. An odd number of intersections corresponds to topologically protected metallic boundary states. From [27].

Fermi level an odd number of times. Since each band intersecting E_F at k_x has a Kramers partner at -k_x, the bulk-boundary correspondence relates the number N_K of Kramers pairs of edge modes intersecting E_F to the change in the $\mathbb{Z}_2$ invariants ν across the interface by:

$$N_K = \Delta\nu \; mod 2. \tag{2.6}$$

Therefore, an odd number of crossings leads to topologically protected metallic boundary states in a 2D topological insulator [27].

2.3.3 HgTe/CdTe quantum wells: the first 2D topological insulator

Kane and Mele proposed graphene—a monolayer of carbon atoms—as a possible candidate for the quantum spin Hall effect [28]. Unfortunately, this proposal turned out to be unrealistic because the quantum spin Hall state is extremely difficult to observe in graphene due to the actual weakness of the spin-orbit interaction [29]. This led to a search for candidate quantum spin Hall systems composed of heavy elements for which spin-orbit coupling is typically much stronger. In 2006, Bernevig, Hughes and Zhang (BHZ) predicted that mercury telluride quantum wells are topological insulators beyond a critical thickness d_c [11]. Their prediction was soon followed by the experimental observation of conducting edge states by König *et al.* [12] and Roth *et al.* [30]. This experimental confirmation has triggered a great deal of excitation in the condensed matter community [8, 23, 27, 31].

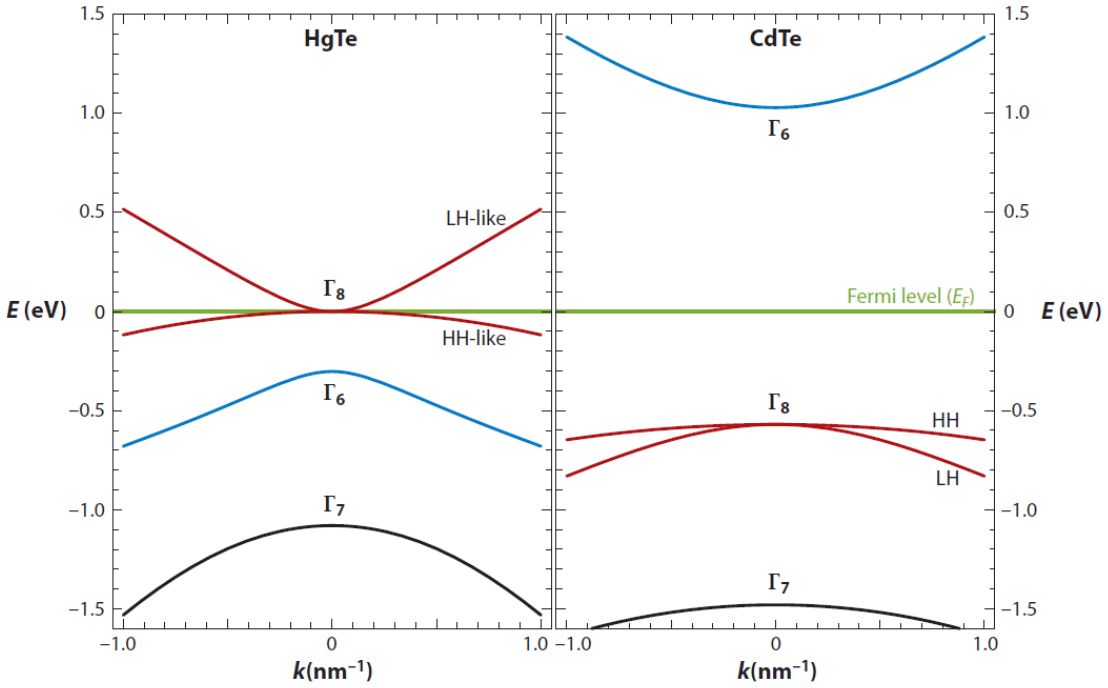

Figure 2.8: Bulk energy bandstructure for 3D HgTe (left) and CdTe (right) near the Γ point. The Fermi level E_F is represented by a green line. From [24].

Mercury telluride (HgTe) and cadmium telluride (CdTe) are 3D semimetal and semiconductor, respectively. Both HgTe and CdTe crystallize in the zinc-blende band structure, which is similar to diamond but with different atoms occupying the two inequivalent sites. For both HgTe and CdTe, the important bands near the Fermi level are close to the Γ point in the reciprocal space and can therefore be indexed according to the Γ point representations of the cubic group. They are the *s*-type antibonding (parity odd) Γ_6 band and the *p*-type bonding (parity even) band that is split into a $J = 3/2$, Γ_8 band and a J = 1/2, Γ_7 band by spin-orbit coupling. Note that due to the strong-spin orbit coupling, the total angular momentum J is a good quantum number at least near $\boldsymbol{k} = 0$. As represented in the right part of figure 2.8, CdTe is characterized by a band ordering following that of GaAs, with a *p*-type (Γ_8, Γ_7) valence bands and a *s*-type (Γ_6) conduction band separated by a large direct energy gap of ∼1.6 eV. On the contrary, HgTe (composed of heavy elements), as a bulk material, can be considered as a symmetry-induced semimetal (figure 2.8, left). Its negative energy gap of -300 meV reveals that the Γ_8 band, which usually forms the valence band, lies above the Γ_6 band. The light-hole (LH) Γ_8 band becomes the conduction band, the heavy-hole (HH) Γ_8 band becomes the topmost valence band, and the *s*-type Γ_6 band is pushed below the Fermi level to lie between the HH band and the spin-orbit split-off Γ_7 band. Due to this unusual sequence of states, such an electronic band structure

with the associated negative bandgap is termed inverted. Eventually, because HgTe and CdTe are structurally similar materials with bandgaps of opposite sign, the quantum spin Hall state can be realized in HgTe/CdTe quantum wells [24]. It should be noted that the Γ_7 band can be ignored because it does not participate in the band inversion between the band structures of HgTe and CdTe.

BHZ considered a quantum well structure where HgTe is sandwiched between layers of CdTe, which has similar lattice contant but much weaker spin-orbit coupling. Using the envelope function method, subband structure of such quantum wells have been derived from the six-band Kane model of HgTe and CdTe [32]. The corresponding six states are denoted: $|E1\pm\rangle$, $|H1\pm\rangle$ and $|L1\pm\rangle$, where, $\pm$ stands for the two Kramers partners. It turns out that the degenerate levels electron-like $|E1\pm\rangle$ have a band crossing with the degenerate heavy-hole like $|H1\pm\rangle$. In contrast, $|L1\pm\rangle$ does not participate to the crossing, and therefore can be ignored. In addition, when the thickness of the HgTe layer is $d < d_c$, CdTe has the dominant effect and the 2D electronic states bound to the quantum well have a normal band order: the *s*-like conduction subband E1 is located above the *p*-like valence subband H1 (figure 2.9(a), left). However, for $d > d_c$, the 2D bands invert (figure 2.9(a), right). Note that d_c is the critical thickness for band inversion and is theoretically predicted to be around 6.5 nm. Moreover, the explicit solution of the model for the E1 and the H1 subbands that describes the quantum spin Hall state in HgTe gives one pair of edge states for $d > d_c$ in the inverted regime (figure 2.9(b), right), and no edge states for $d < d_c$ (figure 2.9(b), left). The pair of edge states carry opposite spins and disperse all the way from the valence band to the conduction band. The crossing of the dispersion curves is required by time reversal symmetry. This constitutes one of the topological signatures of the quantum spin Hall insulator.

Within a year of the theoretical proposal, a team at the University of Würzburg led by Laurens Molenkamp, experimentally observed the quantum spin Hall effect in HgTe quantum wells grown via molecular beam epitaxy [12]. The edge states present a direct way to experimentally discern the quantum spin Hall insulator from the trivial insulator. The two edge states of the quantum spin Hall insulator act as two conducting one-dimensional channels, which each contribute one quantum of the conductance, e^2/h (figure 2.9(c), right). In contrast, a trivial insulator phase provides a vanishing conductance (figure 2.9(c), left). Furthermore, the resistance plateau, shown in figure 2.9(c), right, is identical for samples with distinct widths, from 0.5 μm (red) to 1.0 μm (blue), i.e. the width of the devices differs by a factor of 2, revealing that only the edges are conducting.

To conclude, the 2D topological insulator material, was first experimentally observed in HgTe/CdTe quantum wells. The quantum spin Hall effect is realized only for $d > d_c$,

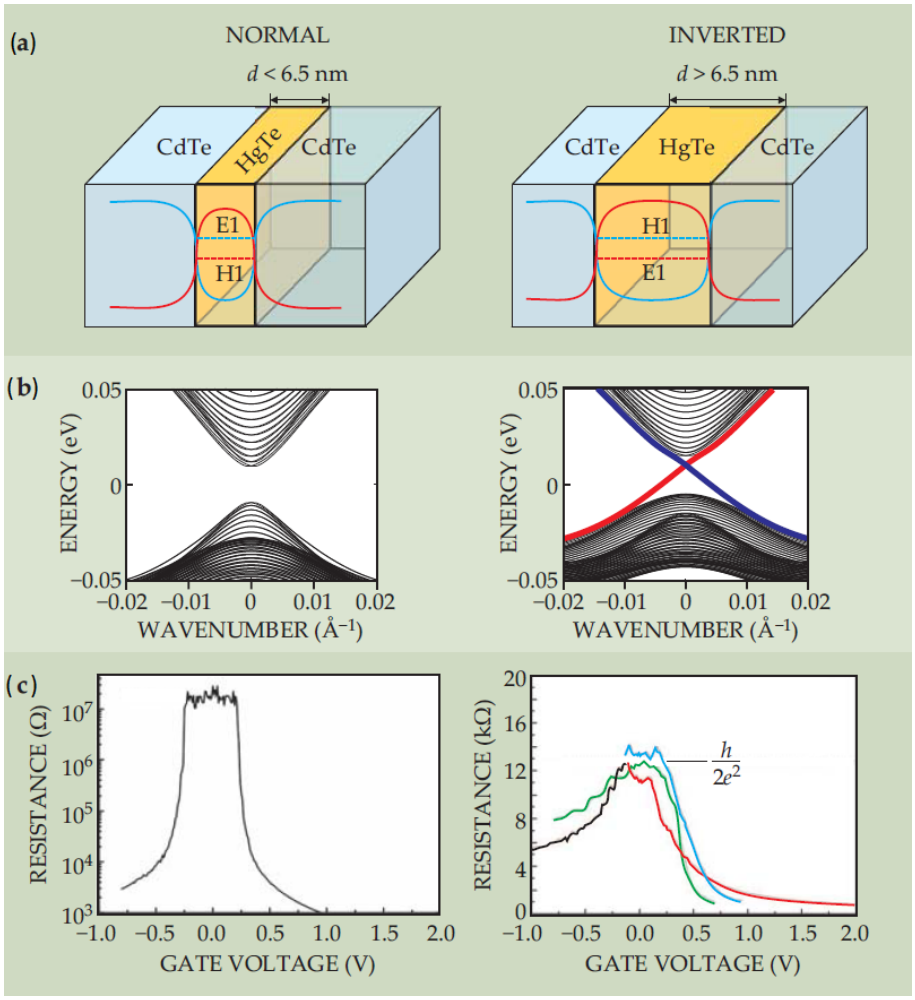

Figure 2.9: Mercury telluride quantum wells are the first 2D topological insulators. (a) The behavior of the mercury telluride quantum well varies as a function of the HgTe layer thickness d. The blue curve represents the potential-energy experienced by electrons in the conduction band; The red curve is the barrier for holes in the valence band. The carriers are trapped laterally by those potentials but are free in the other dimensions. For a quantum well thickness $d < d_c$, the energy of the lowest energy conduction subband, labeled E1, is higher than that of the highest energy valence subband, labeled H1. But for $d > d_c$, those bands are inverted. (b) The electronic band structure of the quantum wells shows that the system is a trivial insulator for thin quantum wells (left), while for thick wells, gapless edge states emerge inside the gap, revealing that the system is a quantum spin Hall insulator (right). (c) Experimentally measured resistance as a function of a gate voltage for thin and thick quantum wells. A quantum well with $d < d_c$, shows insulating behavior, while samples with $d > d_c$ show quantized transport associated with edge states. From [23].

when the quantum well bandstructure is inverted, whereas there is no quantum spin Hall effect (trivial state) for $d < d_c$.

2.4 3D topological insulators

2.4.1 From 2D to 3D topological insulators

A 2D topological insulator is a material supporting a quantum spin Hall effect. It is an insulator in the bulk, but possesses conducting edge states topologically protected by time reversal symmetry. Near the time reversal points in the Brillouin zone, the electronic dispersion resembles the linear dispersion of massless relativistic particles (see figures 2.9(b), right and 2.10(a)), described by the Dirac equation. The linear dispersion relation is the following:

$$E(\mathbf{k}) = \pm \hbar v |\mathbf{k}| \tag{2.7}$$

where v is the electron velocity.

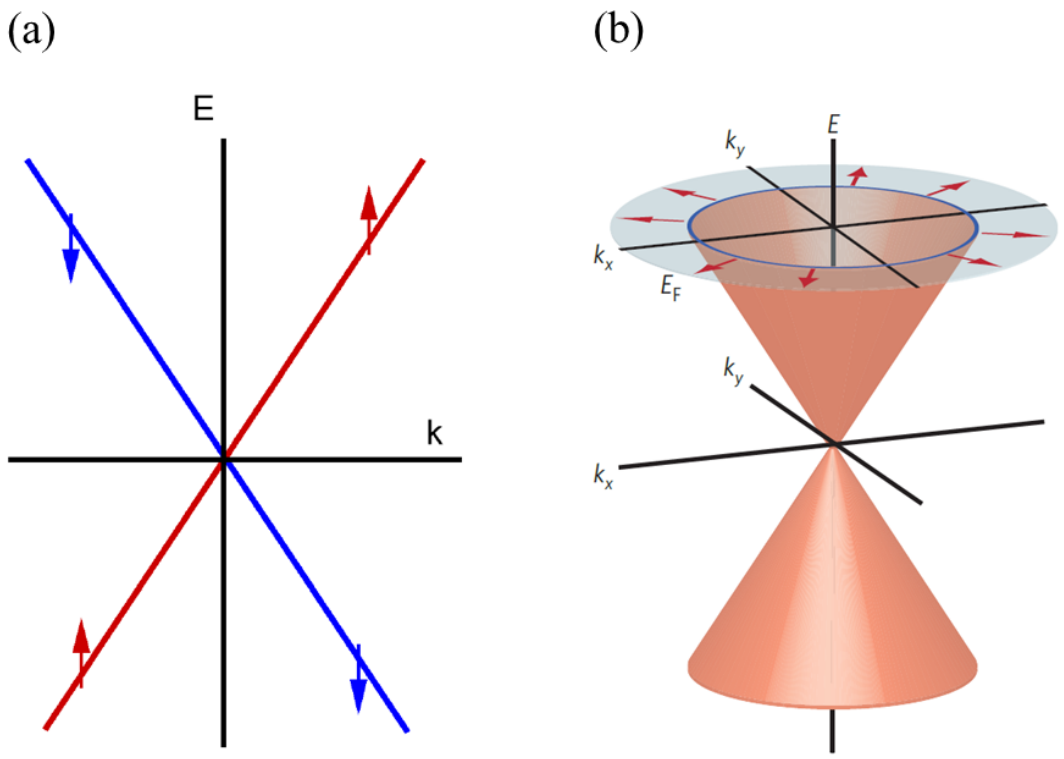

Figure 2.10: Theoretical idealization of the electronic structure of a 2D topological insulator and a strong 3D topological insulator. (a) The edge state disperse linearly in a 2D topological insulator in which up and down spins propagate in opposite directions. (b) The rotation of the spin degree of freedom (red arrows) as an electron (with energy E) moves around the Fermi surface (with Fermi energy E_F). From [1].

Is there a three-dimensional generalization of the topological insulator? In 2006, the next significant theoretical development was the comprehension that even though the

quantum Hall effect does not generalize to a veritably 3D state, the topological insulator does, in a subtle way. One can form a 3D "weak" topological insulator by layering 2D versions of the quantum Hall state. The resulting state is not stable to disorder, and its physics is generally identical to that of the 2D state. However, a "strong" topological insulator exists. Its 3D band structure respects time reversal symmetry, is not layered and is topologically nontrivial. This strong topological insulator has protected metallic surfaces and has been the focus of experimental studies. In strong topological insulators, the spin–orbit coupling is also necessary and must mix all components of the spin. In other words, there is no way to obtain the 3D strong topological insulator from separate spin-up and spin-down electrons, unlike in the 2D case. The planar metallic surface of the strong topological insulators "inherits" topological properties from the bulk insulator. The simplest manifestation of this bulk-surface relation takes place at a smooth surface, where momentum along the surface remains well determined: each momentum along the surface has only a single spin state at the Fermi level, and the spin direction rotates as the momentum moves around the Fermi surface (figure 2.10(b)). By adding non-magnetic disorder or impurities at the surface, there will be scattering between these surface states but, essentially, the topological properties of the bulk insulator do not allow the metallic surface state to disappear—it cannot become localized or gapped. These theoretical predictions, about the electronic structure and the robustness to disorder of the metallic surface state, have led to several experimental investigations on 3D topological insulators in the past years [1].

If we now consider the surface states inside a bulk band gap of a 3D material with time reversal symmetry, there will be four points in the reciprocal space with Kramers degeneracy. For instance, in a rectangular Brillouin zone they could occur at (k_x, k_y) = (0, 0), (π/a, 0), (0, π/b), and (π/a, π/b). As shown in figures 2.11(a) and 2.11(b), these time reversal invariant points are labeled Γ_i in the surface Brillouin zone, where i = 1, 2, 3 and 4. Surface states that cross these points must do so in pairs, but elsewhere spin-orbit coupling can lift the degeneracy. The questions, just as in the 2D case, are: how these Kramers degenerate points at the different time reversal invariant points connect to each other? Does a line at a constant energy, connecting Γ_i with Γ_j, cross through an even or an odd number of surface states? The answer to this questions (in all permutations of i and j) will define four $\mathbb{Z}_2$ invariants, typically labeled (ν_0; $\nu_1\nu_2\nu_3$) [33, 34]. ν_0 describes the number of Kramers points inside a Fermi surface (modulo 2) while ($\nu_1\nu_2\nu_3$) can be interpreted as Miller indices, describing the orientation of the layers.

As above-mentioned, a simple way to achieve a nontrivial topology in three dimensions is by stacking layers of 2D quantum spin Hall insulators, creating a system known as a weak topological insulator. The helical edge states of the layers then become anisotropic

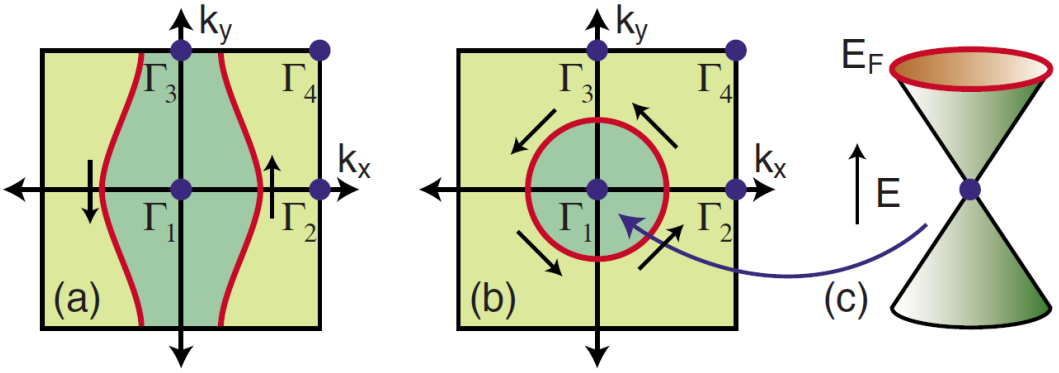

Figure 2.11: Surface states in 3D time reversal invariant systems. (a) A weak topological insulator in which pairs of Kramers degenerate points are separated from each other by an odd number of surface states. (b) A strong topological insulator in which the Fermi surface encloses a single Kramers point. (c) Dirac cone surface states for a strong topological insulator. From [27].

surface states. A possible Fermi surface for weakly coupled layers, stacked along the y direction, is shown in figure 2.11(a). The result is a single surface band separating $\Gamma_{1,3}$ and $\Gamma_{2,4}$ that inherits the spin character of the parent quantum spin Hall system along x. However, we have $\nu_0 = 0$, and the term "weak" refers to the fact that these states are not necessarily topologically protected against disorder.

A strong topological insulator has $\nu_0 = 1$, so that an odd number of Kramers points are enclosed by the surface states in a Fermi cut. A maximally symmetric example is represented in figure 2.11(b), with a circular Fermi surface centered around the Γ point. For time reversal symmetry to be valid on a single surface state, spins must flip when reversing $\boldsymbol{k}$, which is only possible if the spin is locked to momentum direction (arrows in figure 2.11(b)). Moreover, each state on the surface must intersect with its spin-orbit partner to form a degeneracy at the Γ point, so that (at least over some energy scale) it forms a Dirac cone (figure 2.11(c)). The result is the simple surface Hamiltonian which is of the form:

$$H_{surface} = \hbar v_F \, \boldsymbol{\sigma} \cdot \mathbf{k}. \tag{2.8}$$

Here σ refers to Pauli matrices for spin, in contrast to graphene, where it refers to sublattice occupation. There is also no spin or valley degeneracy, but instead just a single Dirac cone.

These surface states have various interesting properties arising from this spin momentum locking. A loop around the Dirac cone results in a π Berry phase due to the full 2π procession of the spin, similar to graphene and the pseudospin. Although arbitrary scattering angles are possible, direct backscattering is not allowed without breaking time

reversal symmetry, just as in the quantum spin Hall effect. These characteristics and their topological nature ensure that even in the presence of a strong disorder, surface states cannot be localized, even though, in general, diffusive transport will still take place [27].

To summarize, the four $\mathbb{Z}_2$ invariants $(\nu_0;\ \nu_1\nu_2\nu_3)$ provide a complete classification of the three dimensional time reversal symmetry insulators. When all four invariants are even, then we have a topologically trivial insulator or an ordinary insulator (e.g. vacuum). If at least one of ν_1, ν_2, or ν_3 is odd while ν_0 is even, then we have a weak topological insulator. For this reason, ν_1, ν_2, and ν_3 are called weak topological invariants. Finally, when ν_0 is odd, we have a strong topological insulator or simply a topological insulator. ν_0 is referred to as the strong topological invariant.

2.4.2 $Bi_{1-x}Sb_x$: the first 3D topological insulator

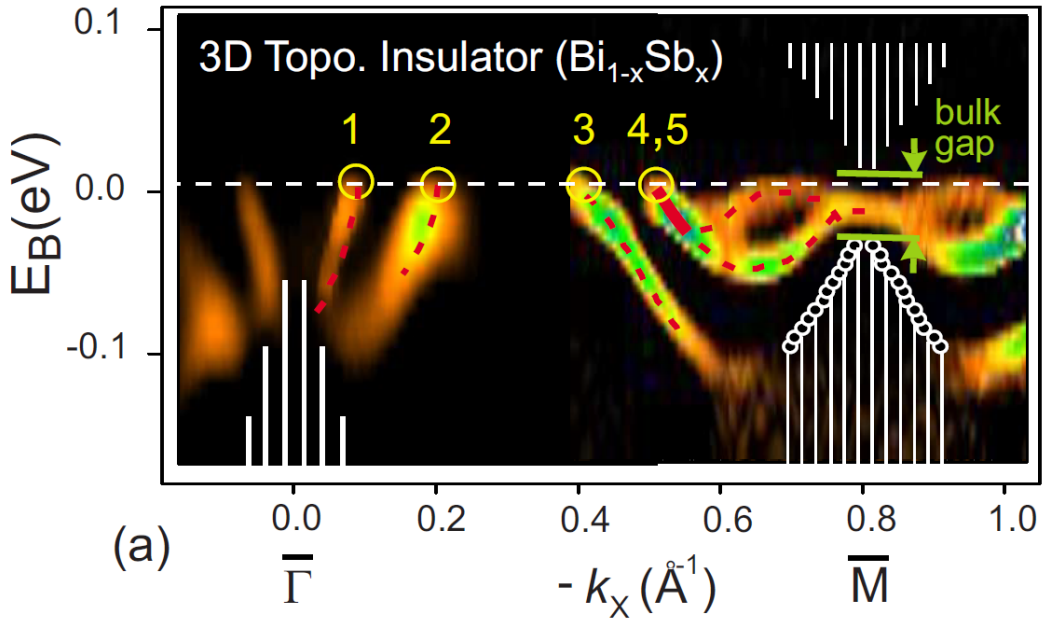

Figure 2.12: ARPES data on the (111) surface of $Bi_{0.91}Sb_{0.09}$ which probes the occupied surface states as a function of momentum on the line connecting the high symmetry points $\bar{\Gamma}$ and $\bar{M}$ in the surface Brillouin zone. The surface bands cross the Fermi energy five times, which establishes that the semiconducting alloy of $Bi_{0.91}Sb_{0.09}$ has topologically protected surface states. From [14].

After being predicted by Fu and Kane [13], the first 3D topological insulator to be identified experimentally was the semiconducting alloy $Bi_{1-x}Sb_x$, whose unusual surface bands were mapped in an ARPES experiment by Hsieh *et al.* [14]. ARPES measurements offer several advantages in comparison to other experimental approaches. Charge

transport experiments, which were successful for identifying the 2D topological insulators [12], are problematic in 3D materials. The difficulty is due to the fact that separating the surface contribution to the conductivity from that of the bulk is extremely hard. On the other hand, the ARPES measurements allow for a clear isolation of surface states from that of the bulk 3D band structure because surface states do not disperse along a direction perpendicular to the surface whereas the bulk states do (this will be further discussed in the coming chapter).

Experiments by Hsieh *et al.* [14] probed both the bulk and surface electronic structures of $Bi_{0.91}Sb_{0.09}$ with ARPES. Figure 2.12 shows the ARPES spectrum, which can be interpreted as a map of the energy of the occupied electronic states as a function of momentum along the line connecting $\bar{\Gamma}$ to $\bar{M}$ in the projected surface Brillouin zone. The experiments observed several surface states that span the bulk gap. The observed surface bands cross the Fermi energy five times between $\bar{\Gamma}$ and $\bar{M}$. This odd number of crossings is analogous to figure 2.7(b) and indicates that these surface states are topologically protected. As previously discussed in section 2.3.2, Kramers' theorem requires surface states to be doubly degenerate at the high symmetry points of the surface Brillouin zone $\bar{\Gamma}$ and each of the three equivalent $\bar{M}$ points. Such a Kramers point is indeed observed at $\bar{M}$ approximately 15 ± 5 meV below the Fermi level E_F. As expected for a system with strong spin-orbit interactions, the degeneracy is lifted away from $\bar{M}$. Accounting for the threefold rotational symmetry and mirror symmetry of the (111) surface, these data show that the Fermi surface encloses $\bar{\Gamma}$ an odd number of times, while it encloses the three equivalent $\bar{M}$ points an even number of times. This establishes $Bi_{1-x}Sb_x$ as a strong topological insulator, with $\nu_0 = 1$. The data are consistent with the predicted (1; 111) topological class. Note that later, spin-sensitive measurements demonstrated the predicted spin texture of these bands, confirming the topological order of the material [35], and the absence of direct backscattering was demonstrated using scanning tunneling microscopy [36].

The surface structure of $Bi_{1-x}Sb_x$ was rather complicated and the bandgap was rather small. This motivated a search for topological insulators with a larger bandgap and simpler surface spectrum. A second generation of 3D TI materials offer a much more vivid demonstration of topological physics. Example materials in this family include Bi_2Te_3, Bi_2Se_3 and Sb_2Te_3, which have a crystal structure composed of quintuple layers. Compared to $Bi_{1-x}Sb_x$, they have a simpler band structure, a larger bulk bandgap and a different topological phase (1; 000) rather than (1; 111) [27]. In the following section, I will present the crystallographic and electronic structures of one compound in this family, namely bismuth telluride Bi_2Te_3.

2.4.3 Bi_2Te_3: a 3D topological insulator

In chapter 4, I will present an experimental study of Bi_2Te_3 compounds under several electron irradiation conditions. For this reason, I will illustrate in this section some previous experimental and theoretical works on Bi_2Te_3.

2.4.3.1 Crystallographic structure

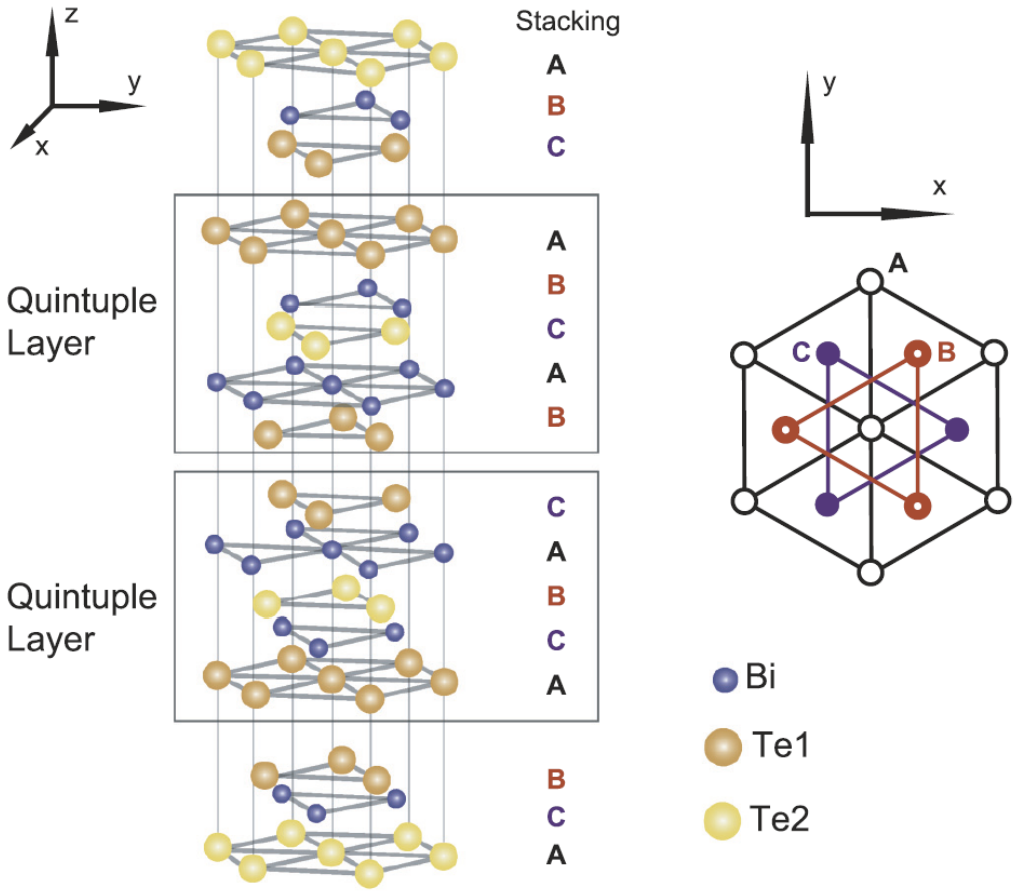

Figure 2.13: Hexagonal unit cell of the Bi_2Te_3 crystal comprised of three quintuple layers. The Te2 layer within each quintuple layer is a center of inversion symmetry. From [37].

The Bi_2Te_3 primitive cell is shown in figure 2.13. Bi_2Te_3 crystals belong to the rhombohedral crystal system with a layer structure. The bulk structure consists of alternating hexagonal monatomic crystal planes stacking in ABC order. Units of Te-Bi-Te-Bi-Te form quintuple layers: bonding between atomic planes within a quintuple layer is covalent, whereas bonding between adjacent quintuple layers is predominantly of the van der Waals type. This weak bonding between quintuple layers allows the crystal to be easily

cleaved along an inter-quintuple layer plane. The crystal structure belongs to the space group $R\bar{3}m$, while the point group contains a binary axis (with twofold rotation symmetry), a bisectrix axis (appearing in the reflection plane), and a trigonal axis (with threefold rotation symmetry). A unit cell in the hexagonal basis contains three quintuple layers and thus fifteen atoms, whereas the actual primitive cell in the rhombohedral basis contains five atoms [37, 38].

2.4.3.2 Electronic structure

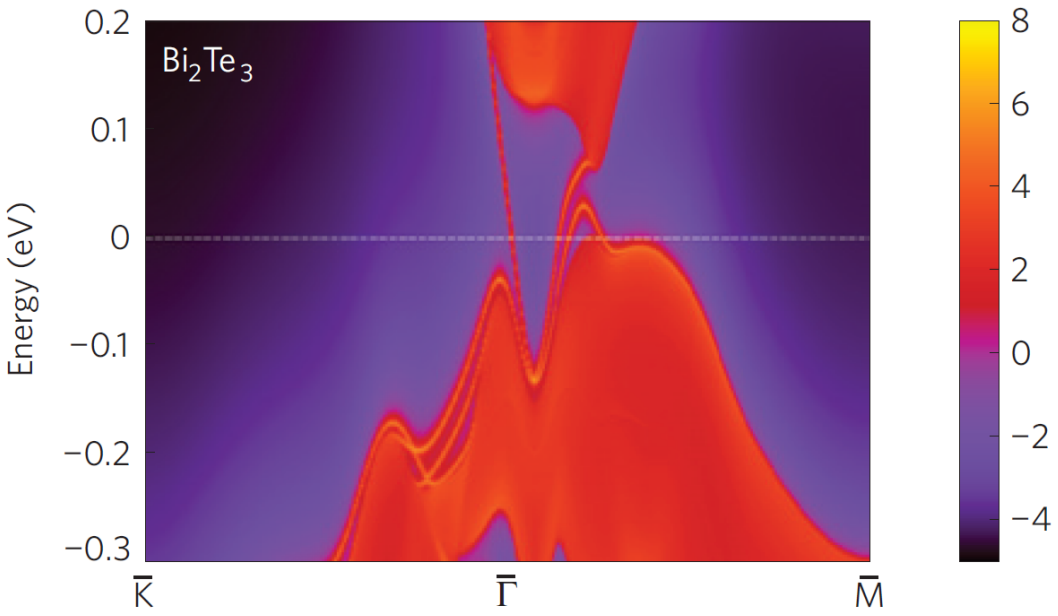

Figure 2.14: The calculated electronic band structure of Bi_2Te_3. The red regions correspond to bulk energy bands and the blue regions indicate bulk energy gaps. The surface states can be clearly seen around the $\bar{\Gamma}$ point as red lines dispersing in the bulk gap. From [15].

Figure 2.14 shows the calculated electronic band structure for Bi_2Te_3 on the [111] surface obtained by Zhang *et al.* in 2009 [15]. These calculations predicted that Bi_2Te_3 is a topological insulator with robust surface states, consisting of a single Dirac cone at the Γ point. The presence of these topological surface states can be directly verified by various experimental techniques, such as ARPES and scanning tunnelling microscopy (STM). As it will be explained in the next chapter, ARPES constitutes a powerful technique to experimentally measure the electronic band structure in solids, specifically the one of the surface states. Evidence of surface states has been observed for Bi_2Te_3 in ARPES experiments performed by Noh *et al.* [40] and Chen *et al.* [17]. Figure 2.15(a) illustrates the

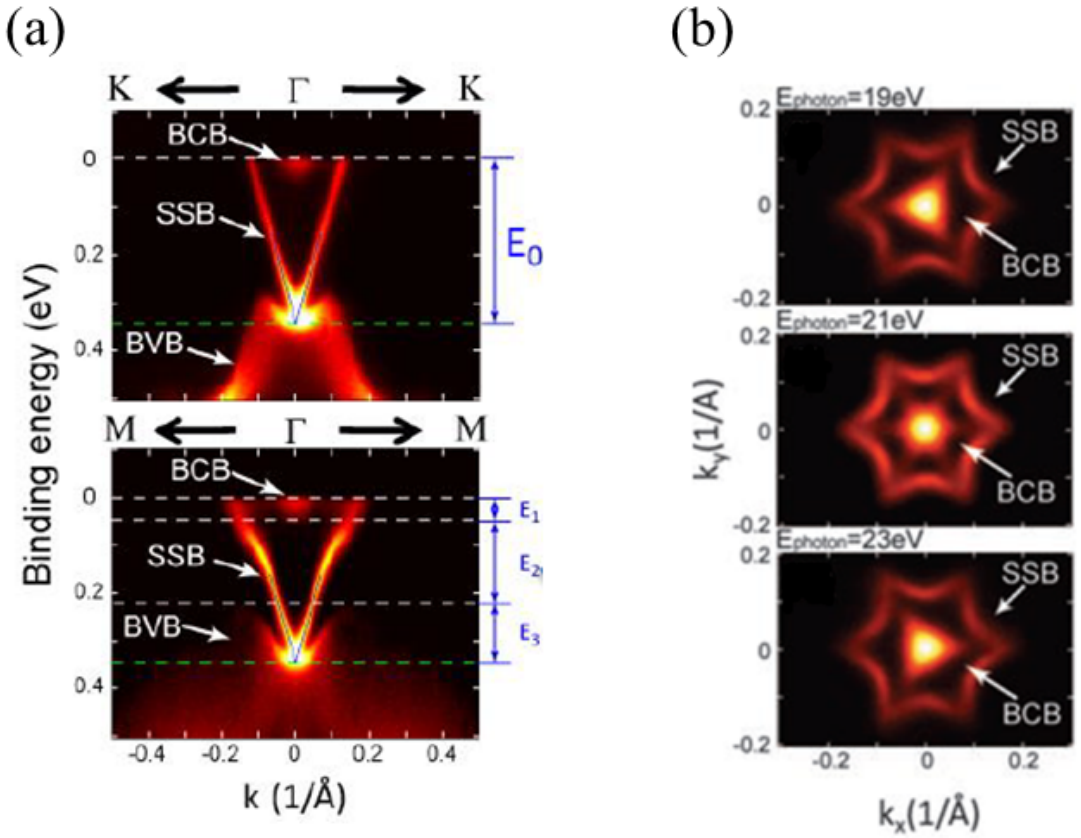

Figure 2.15: Electronic structure of Bi_2Te_3. (a) ARPES measurements of the electronic band dispersions along the ΓK (top) and the ΓM (bottom) directions. Energy scales of the band structure are labeled as follows: E_0: binding energy of Dirac point (0.34 eV); E_1: BCB bottom binding energy (0.045 eV); E_2: bulk energy gap (0.165 eV); and E_3: energy separation between BVB top and Dirac point (0.13 eV). (b) Photon energy–dependent Fermi surface maps. The shape of the inner Fermi surface clearly changes with photon energies, indicating a strong k_z dependence due to its bulk nature, whereas the nonvarying shape of the outer hexagram Fermi surface confirms its surface state origin. From [17].

ARPES measurements, performed by Chen *et al.* [17], of Bi_2Te_3 band dispersions along the ΓK (top) and the ΓM (bottom) high symmetry directions, confirming the existence of topological surface state band (SSB) structure that consists of a single Dirac cone at the Γ point. In addition, the broad bulk band (the bulk conduction band (BCB) and the bulk valence band (BVB)) dispersions and the sharp V-shape SSB dispersion are identical to those in figure 2.14. Note that the apex of the V-shape dispersion is the Dirac point. As shown in figure 2.15(a), Bi_2Te_3 has a bulk energy gap of 0.165 eV, designated as E_2. It should be pointed out that stoichiometric Bi_2Te_3 has an indirect bulk bandgap, i.e. the valence band maximum exhibits an indirect gap with the conduction band minimum. Furthermore, figure 2.15(b) reveals the Fermi surface maps of Bi_2Te_3 obtained at different

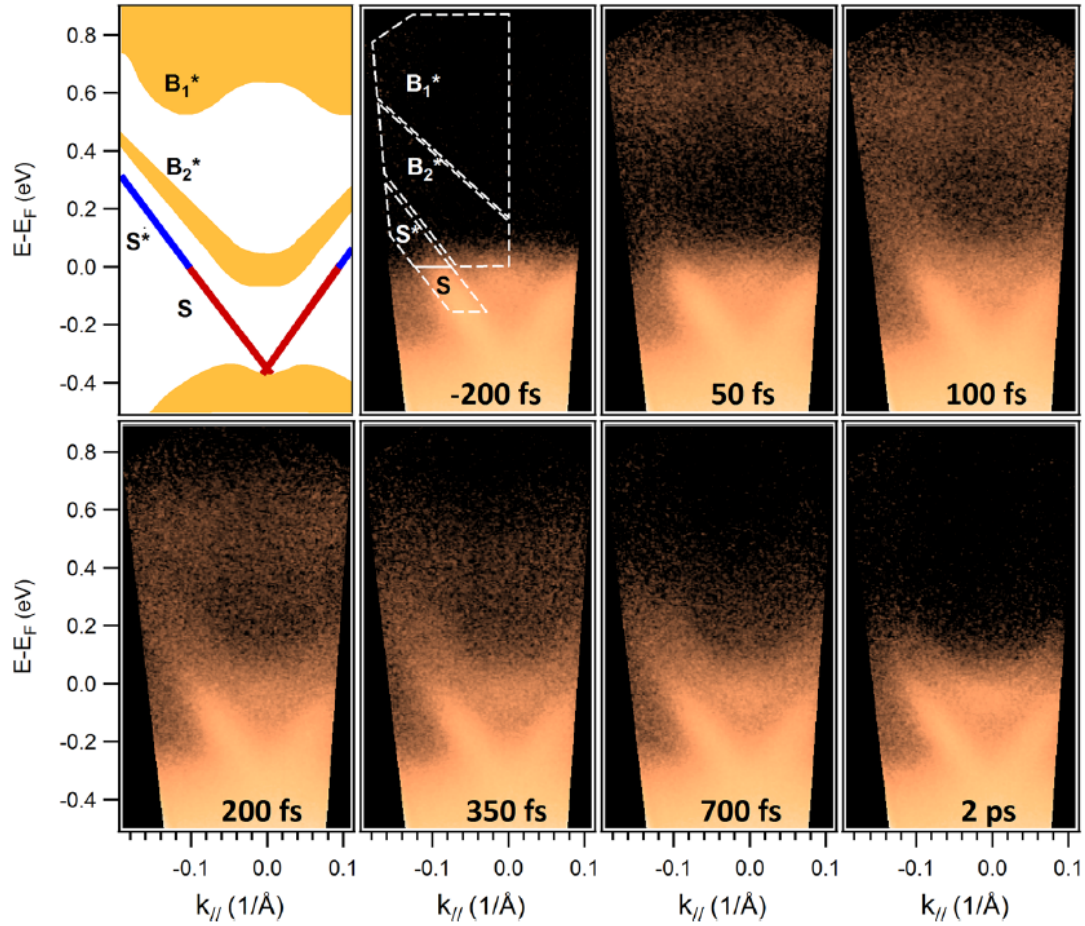

Figure 2.16: trARPES sequence obtained after photoexcitation from the femtosecond laser pump pulses. The color intensity is presented in logarithmic scale to make the signal from the transient electronic states more evident. In the upper left corner, a schematic view of the bands involved in the process, namely the projections of the bulk bands B_1* and B_2* and the surface Dirac cone, is presented. From [39].

photon energies. By varying the excitation photon energy, the shape of the snowflake-like bulk Fermi surface changes from a left-pointing triangle (figure 2.15(b), upper panel) to a right-pointing triangle (figure 2.15(b), lower panel) as a result of the k_z dispersion of the 3D bulk electronic structure. In contrast, the shape of the hexagram-like Fermi surface does not vary with the incident photon energy, confirming its 2D nature and its surface state origin (i.e., no k_z dispersion). Consequently, the combination of theoretical calculations and photoemission spectroscopy has proved that Bi_2Te_3 is a bulk band gap semiconductor whose surface is characterized by a single topological Dirac cone.

In 2012, the unoccupied electronic band structure of Bi_2Te_3 (n-type) and its ultra-fast temporal evolution have been investigated by Hajlaoui *et al.* [39]. Using time- and angle-resolved photoemission spectroscopy (trARPES), a direct real-time visualization

of the transient carrier population of both the surface states and the bulk conduction band has been provided in this study (figure 2.16). Note that the trARPES technique will be explained in details in the coming chapter. The ultrafast dynamics of the carriers in the surface Dirac cone were found to be delayed with respect to the bulk, because the bulk acts as a reservoir that keeps providing a relevant charge flow for more than 0.5 ps; subsequently, few picoseconds were necessary for the Dirac cone nonequilibrium electrons to recover a Fermi-Dirac distribution, while their relaxation were extended over more than 10 ps. In chapter 4, I will present a trARPES study of Bi_2Te_3 compounds under several irradiation conditions and I will show that the long-lived surface state population is probably a general property of the Bi_2Te_3 system.

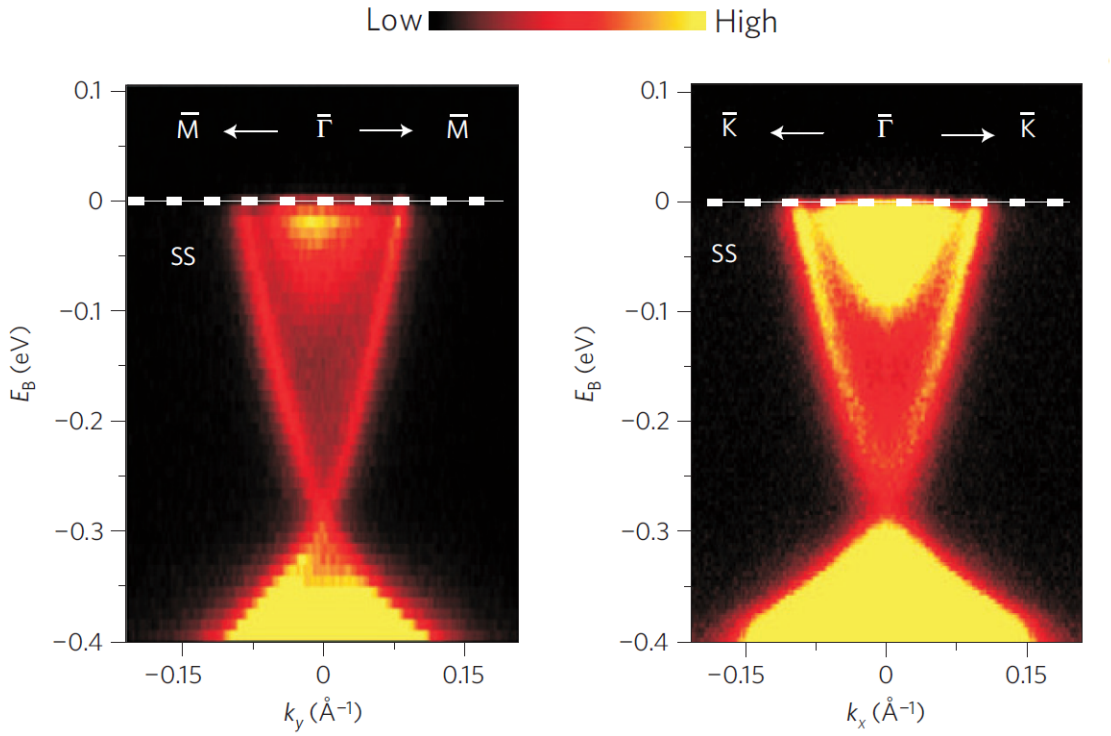

Figure 2.17: High-resolution ARPES intensity maps of Bi_2Se_3, acquired with an incident photon energy of 22 eV, along the $\overline{\Gamma M}$ (left) and the $\overline{\Gamma K}$ (right) high symmetry directions, illustrating the presence of a single Dirac cone on the surface centered at the $\bar{\Gamma}$ point. From [16].

Besides Bi_2Te_3, the other prototype compound belonging to the second generation of 3D topological insulator materials and revealing numerous interesting properties is bismuth selenide Bi_2Se_3. Bi_2Se_3 share the same rhombohedral structure of Bi_2Te_3, which is presented in figure 2.13, and has a topologically nontrivial energy gap of 0.3 eV. In 2009, Xia *et al.* [16] have used ARPES and theoretical calculations to study the surface band structure of Bi_2Se_3 and observe the characteristic signature of a topological insulator in

the form of a single Dirac cone (figure 2.17). Concurrent theoretical work by Zhang *et al.* [15] has used electronic structure methods to show that Bi_2Se_3 is a topological insulator with robust surface states consisting of a single Dirac cone at the Γ point. Detailed and systematic surface investigations of Bi_2Se_3 by Hsieh *et al.* [41] and Park *et al.* [42] have confirmed the topological band structure of this material. In addition, trARPES has also been employed by Sobota *et al.* [43, 44] and Crepaldi *et al.* [45, 46] to investigate the out-of-equilibrium electronic structure and dynamics of Bi_2Se_3. In particular, Sobota *et al.* [43] have found that optical excitation leads to a metastable population at the bulk conduction band edge, which feeds a nonequilibrium population of the surface state persisting for more than 10 ps. These results, showing an unusually long-lived population of the metallic Dirac surface states, are in a good agreement with our results presented in chapter 4. Finally, the out-of-equilibrium spin and electronic properties of Bi_2Se_3 have been probed by Cacho *et al.* [47] by means of spin-, time-, and angle-resolved photoemission spectroscopy (STAR PES). In this study, the band structure in the unoccupied density of states was fully mapped and a spin-polarized surface resonance state with a topologically trivial character was identified. This newly discovered surface resonance state was shown to play a key role in the spin-dependent relaxation of the photoexcited electrons, by partially decoupling the bulk conduction band from the topological surface states. Therefore, all these studies confirm that Bi_2Se_3 is a topologically nontrivial compound.

In conclusion, the electronic structures of Bi_2Te_3 and Bi_2Se_3 have been extensively investigated both experimentally and theoretically. These studies on their robust topological surface states, forming a single Dirac cone at the Γ point, revealed many interesting properties of 3D topological insulators, both at equilibrium and out-of-equilibrium.

2.5 Conclusion

To conclude, advances in the physics of topological insulators have been driven by a rich interplay between theoretical insight and experimental discoveries. There is reason for optimism that this field will continue to develop in exciting new directions. The field of topological insulators is at an early stage in its development. There is much work to be done to realize the potential of these novel and fascinating materials. In this chapter, I have discussed the basic properties of topological insulators which have been established as a result of several previous works. In chapter 4 and 5, I will present my experimental work based on a photoemission study of the irradiated topological insulator Bi_2Te_3 and the natural topological superlattice phase Sb_2Te.

Chapter 3

Experimental techniques based on photoemission spectroscopy

In this chapter, I provide an overview on the experimental methods and instruments employed in this thesis to investigate the electronic properties of the studied topological materials. I first introduce photoemission spectroscopy. Then, I present the basic principles of X-ray photoemission spectroscopy and highlight the characteristics of high brightness synchrotron radiation sources. Further, I describe angle-resolved photoemission spectroscopy and the pump-probe technique, and discuss in detail the ultrafast carrier dynamics in solids after a photoexcitation with femtosecond laser pulses. Finally, I illustrate scanning photoemission microscopy capabilities and emphasize the importance of synchrotron radiation sources in the development of high spatial resolution photoemission spectroscopy techniques.

3.1 Photoemission spectroscopy (PES)

PhotoEmission (also known as PhotoElectron) Spectroscopy (PES) has been established as one of the most important experimental methods to study the electronic structure of solids and their surfaces [48]. The experiment is based on the photoelectric effect originally observed by Hertz in 1887 [49]. This was later explained as a manifestation of the quantum nature of light by Einstein in 1905 [50], who introduced the concept of the photon and recognized that when light is incident on a sample, an electron can absorb a photon and escape from the matter with a maximum kinetic energy, hν - ϕ, where hν is the photon energy and ϕ is the work function of the material. Note that the work function, a physical quantity characterizing several materials, is the minimum energy required to remove an electron from a solid [51], typically around 4–5 eV for metals. In this spectroscopic technique, the solid surface is irradiated by mono-energetic photons

and emitted electrons, called photoelectrons, are analyzed with respect to their kinetic energy. When photons in the ultraviolet spectral range are used, the technique is called Ultraviolet Photoemission Spectroscopy (UPS); By means of X-ray radiation, it is called X-ray Photoemission Spectroscopy (XPS) or Electron Spectroscopy for Chemical Analysis (ESCA). With a synchrotron light source, discussed in detail in section 3.2.3, one can tune the photon energy and cover the whole wavelength range from the near-UV to the far X-ray regime.

XPS is mainly employed to probe the core level states. Since core levels of atoms have well defined binding energies, an element identification can be performed by locating these core levels [52]. Whereas by means of UPS, we can investigate the valence band states. In order to study the dispersion of valence electronic bands $E(\boldsymbol{k})$ for bulk and surface states in the reciprocal space, a determination of the electron wave vector is required. Thus, besides the kinetic energy, one also need to determine the emission angle. This can be done by means of an electron analyzer with small angular aperture. The method is then known as Angle-Resolved Ultraviolet Photoemission Spectroscopy (ARUPS) or Angle-Resolved PhotoEmission Spectroscopy (ARPES) [53, 54]. Therefore, ARPES constitutes a highly advanced tool to explore the wave vector-dependent filled electronic band structure of solids.

Moreover, one of the most exciting opportunities is the investigation of a system using ultrafast light. The term "ultrafast" is used to indicate photon pulses with a femtosecond duration (1 fs = 10^{-15} s). The femtosecond is the typical time scale for the motion of electrons in matter, and the most advanced laser sources make it nowadays possible to reach this time scale. When ARPES is performed via two photon laser pulses in a pump-probe combination, i.e. a pump pulse and a probe pulse, a time-resolved ARPES (trARPES) study of the dispersion and the evolution of the occupied and unoccupied electronic bands of matter can be performed with a femtosecond time resolution [55, 56, 57].

Finally, photoemission experiments with high spatial resolution, obtained by focusing the radiation in a small spot on the sample by means of light focusing optics, can be performed using Scanning PhotoEmission Microscopy (SPEM). This technique makes it possible to obtain much-wanted and difficult-to-obtain information on the electronic structure of distinct microscopic domains for non homogeneous samples [58, 59].

In this thesis, I present a photoemission experimental study via two modalities: the first one is trARPES used to investigate the unoccupied topological surface states of the irradiated topological insulator Bi_2Te_3 and the natural topological superlattice phase Sb_2Te; the second one is SPEM employed to assess the heterogeneity of the cleaved surface of Sb_2Te by comparing the electronic structure in regions possessing different surface terminations. Note that the XPS technique was also used to probe the Sb_2Te core levels in order

to reveal the significant importance of the SPEM study. In the following, I introduce the XPS technique to later provide an extended description on ARPES, trARPES and SPEM methods.

3.2 X-ray photoemission spectroscopy (XPS)

3.2.1 Fundamental concepts

XPS is the high-energy version of the photoelectric effect. It is basically employed for identifying chemical elements at the sample surface. As above-mentioned in the preceding section 3.1, in XPS, the photons that interact with core level electrons are X-rays. When a surface is irradiated with X-ray photons of sufficient energy, exceeding the binding energy of the electrons, photoelectrons of inner shells can be ejected (as shown in figure 3.1). Even though the principle of XPS had been known for a long time, implementation had to await the introduction of a high-resolution spectrometer for the detection of the low-energy XPS electrons in the 1960s by Siegbahn and coworkers in Sweden [60, 61]. He coined the term "electron spectroscopy for chemical analysis", but since other methods also provide chemical information, it is more commonly known as XPS today. The early history and development of XPS has been well described by Jenkin *et al.* [62].

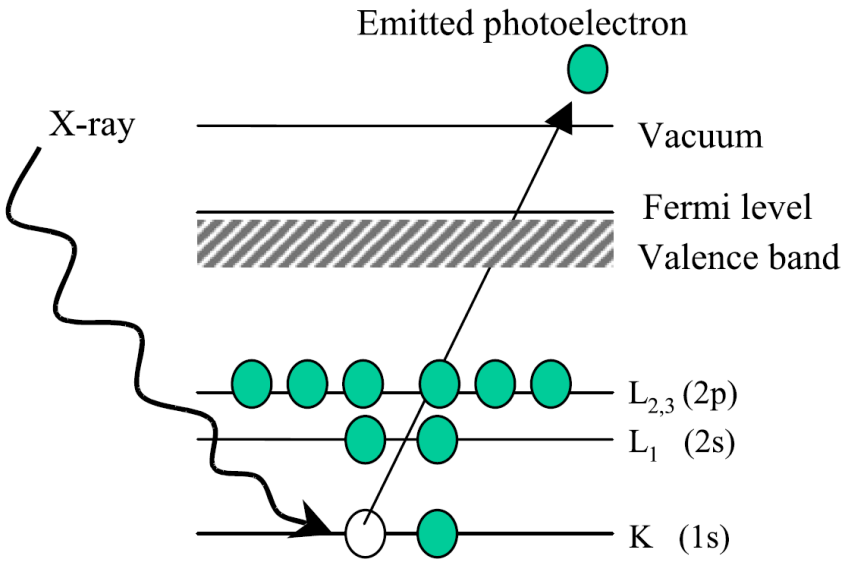

Figure 3.1: Schematic illustrating the emission of a photoelectron from an atom irradiated with X-ray photons. From [63].

The experimental quantity measured by the spectrometer is the kinetic energy E'_{kin} of

the emitted electron, which is related to the electron binding energy E_B, referenced to the Fermi level E_F, by:

$$E_B = h\nu - E'_{kin} - \phi' \tag{3.1}$$

where $h\nu$ is the energy of the primary X-rays and ϕ' is the work function of the spectrometer (3 to 4 eV). With E_B depending on the X-ray energy, it is essential that the incoming X-ray energy to be monochromatic. The spectrometer and the sample are connected forcing their Fermi levels to line up. This will be further discussed in the coming section 3.3.3.2. Note that E_F for metals is well determined. Whereas for semiconductors and insulators, E_F can change from one sample to another.

E_B is not only characteristic for each element but also for its electronic surrounding. This is a significant strength of XPS; it is used to investigate quantitatively the elemental composition and its chemical environment. Handbooks and graphs of E_B for elements and compounds are available [64, 65]. It is sometimes claimed that XPS generates no charging. For insulating specimens, while it is true that X-rays possess no charge, a positive sample charging occurs. This is due to electron emission from the sample and can be compensated with an electron flood gun. In XPS studies, Auger electron emission also takes place. Auger lines can interfere with XPS lines. By varying the incident X-ray photon energy, the energy of XPS electrons varies while the one of Auger electrons remains stable.

XPS is a surface sensitive technique because the ejected electrons originate from the upper 0.5–5 nm of the sample [66]. The electron escape depth is related to the electron inelastic mean free path. This will be more detailed in section 3.3.2. The electrons excited deeper within the crystal are unable to exit the surface.

It should be pointed out that the major use of XPS is for identification of compounds using energy shifts due to changes in the chemical structure of the sample atoms. In fact, in XPS spectra, the E_B of a particular peak depends not only on the element but also on the chemical environment and energy state of the atoms. Any change of the chemical environment and state, which perturbs the energy level of the atom, will cause a variation in the XPS spectrum. This variation in E_B is called chemical shift.

3.2.2 XPS spectral features

3.2.2.1 Spin orbit splitting

The observed photoelectrons are represented by means of their quantum numbers. Transitions are usually labeled according to the scheme nl_j. The first part of this notation is the principal quantum number, n, which takes integer values of 1,2, 3 etc. The second part of the nomenclature is l, the angular quantum number, which takes integer values of 0, 1,

2, 3 etc. However, this quantum number is usually given a letter rather than a number as shown in table 3.1.

Table 3.1: Notation given to the quantum numbers which describe orbital angular momentum.

Value of l	Usual notation
0	s
1	p
2	d
3	f

All orbital levels, except the s levels, give rise to a doublet with two possible states, having different binding energies in the XPS spectra. This is known as spin-orbit splitting (or j-j coupling) and is a result of the interaction of the electron angular momentum due to its spin with its orbital angular momentum. Each electron has a quantum number coupled with its spin angular momentum, s. The value of s can be either +1/2 or -1/2. The two angular momenta are added vectorially to provide the quantity j in the expression nl_j, i.e. $j = |l + s|$. Thus, an electron from a p orbital can have a j value of 1/2 (l - s) or 3/2 (l + s); identically, electrons from a d orbital can have j values of either 3/2 or 5/2. The relative intensity of the components of the doublets formed by the spin orbit coupling is determined by the occupation probability of the two different energy states, which is expressed as the multiplicity, $M = 2j + 1$. For example, for an electron from a d orbital, the relative intensities of the 3/2 and 5/2 peaks are 2:3. The spacing between the components of the doublets depends upon the strength of the spin orbit coupling. For a given value of both n and l, the separation increases with the atomic number of the atom. For a given atom, it decreases both with increasing n and with increasing l [67].

3.2.2.2 Peak width

The width of XPS peaks is considerably determined by the natural linewidth (or the core hole lifetime broadening), and by the instrumental resolution which depends on the resolution of the electron energy analyzer and the wavelength spread in the incident X-ray beam. Note that sample inhomogeneity and satellite features can also lead to peak broadening, especially if the instrumental resolution is insufficient to resolve the latter from the main photoemission feature. Thus, the resolution of XPS is provided by the natural

linewidth of the level under study ΔE_{nat}, the broadening due to the analyzer ΔE_{an}, and the linewidth of the X-ray radiation source $\Delta E_{h\nu}$. These three factors are related as follows:

$$\Delta E = \sqrt{(\Delta E_{nat})^2 + (\Delta E_{an})^2 + (\Delta E_{h\nu})^2} \tag{3.2}$$

where ΔE is the width of the XPS peak at half maximum.

According to the Heisenberg uncertainty relation, the natural linewidth, ΔE_{nat}, and the core hole lifetime, Δt, are related by:

$$\Delta E_{nat} \,.\, \Delta t \approx \frac{h}{2\pi} \tag{3.3}$$

where h is the Planck constant.

The core hole lifetime generally decreases for inner shell orbitals (deeper core holes) because inner shell core holes are filled by higher lying electrons. Similarly, for a given energy level, the lifetime decreases (the linewidth increases) as the atomic number increases. The lifetime broadening produces a Lorentzian contribution to the spectral line shapes. The analyzer width, ΔE_{an}, depends on the pass energy used during the experiment. For lower pass energies, ΔE_{an} is smaller and thus the resolution is better. The analyzer resolution function has a Gaussian line shape [68].

3.2.3 Synchrotron radiation

3.2.3.1 Principle of operation

The best and most advanced source for X-rays is synchrotron radiation. Its main advantages are tunability over the whole electromagnetic spectrum, in particular in the XUV and X-ray region. Third generation synchrotron radiation sources like SOLEIL, the French synchrotron light source (see figure 3.2), are the best X-ray sources in terms of brightness.

When electrons traveling at relativistic speeds, close to the speed of light c, are forced by applied magnetic fields, perpendicular to the direction of their motion, to follow curved trajectories, they emit electromagnetic radiation with peculiar characteristics in the direction of their motion (figure 3.3). This radiation is called synchrotron radiation. Relativistic positrons also emit synchrotron radiation in the magnetic field by the same principle.

The "natural" man-made sources of this radiation are circular electron- or positron-accelerators like storage rings in which the particles move with relativistic energies. The storage rings consist of circular evacuated pipes where the electrons are forced to follow circular paths under the action of bending magnets placed along the circumference. The electrons enter the storage ring only after they have been accelerated by a linear acceler-

Figure 3.2: An aerial view of the SOLEIL synchrotron located on the Plateau de Saclay in Saint Aubin.

ator, the linac, until their energy attains several millions of electron volts (MeV) and then by a booster ring that boosts their energies from millions to billions or giga electron volts (GeV); at that point, they are transferred to the final circular accelerator (see figure 3.4). Here, the electrons, if required, may be further accelerated to higher energies by the radio frequency (RF) electric fields. When the electrons reach the appropriate energy, they are forced to follow circular paths by the magnetic field of the bending magnets. During each turn, electrons loose part of their energy emitting synchrotron radiation. When passing through the RF cavities, the energy losses due to synchrotron radiation are fully compensated [69]. The synchrotron radiation generated in the bending magnets and insertion devices (wigglers or undulators) is diverted, selected and shaped by optic systems in experimental stations called beamlines. Each beamline is a specialized laboratory equipped to prepare and analyze samples to be investigated.

3.2.3.2 Technical elements

Vacuum system

To avoid particle losses due to scattering on residual gas atoms, the electron beam must be enclosed in a vacuum chamber where the air pressure is decreased to 10^{-9} mbar or lower. Once injected into the storage ring, the electrons are expected to circulate and generate synchrotron radiation for several hours with a minimum rate of loss. This low pressure is reached by putting many vacuum pumps along the circular path.

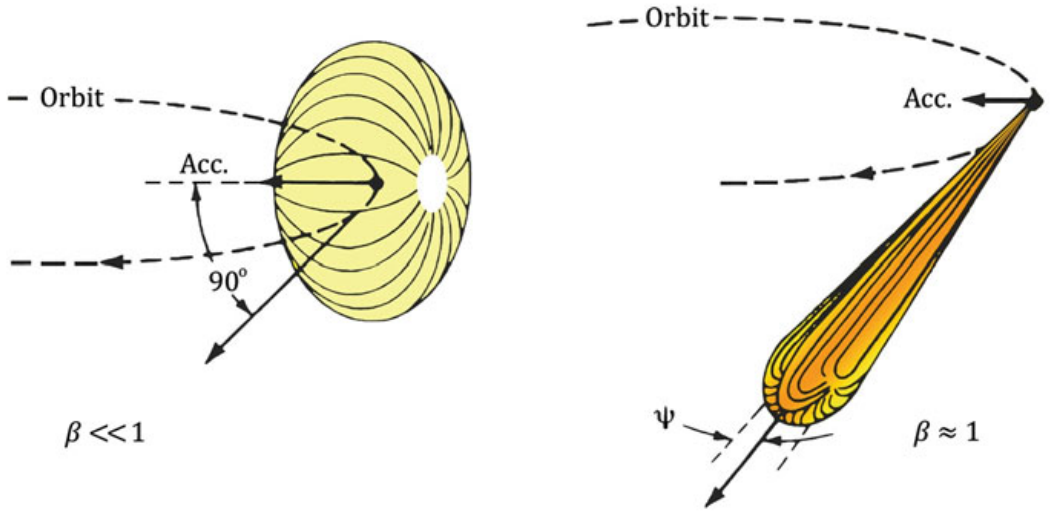

Figure 3.3: Qualitative electromagnetic radiation patterns associated to charged particles traveling in a circular orbit. The dipole pattern achieved for slow particles (left), moving at velocities that are small compared to the speed of light β = v/c « 1, is distorted into a narrow cone when $\beta \approx 1$ (right). ψ is the vertical half-opening angle ($\psi \approx mc^2/E$). From [69].

Bending magnets

The bending magnets, placed in a well organized order to form a closed ring, are employed to deflect and force the electron beam to follow a closed trajectory along the circular accelerator. In fact, the bending magnets apply to each electron a Lorentz force perpendicular to its vector velocity. This force does not modify the energy of the electrons, but it causes a centripetal acceleration that changes the direction of the velocity. The geometry of the storage ring is determined by the position and the deflection angle of the bending magnets. Even though we call this a circular accelerator, the shape is actually not circular. A series of arc sections (bending magnets) are connected by straight sections to make space for other systems. Bending magnets are also used as sources of synchrotron radiation [70].

Insertion devices

In order to provide the desired radiation characteristics, periodic magnetic structures, called insertion devices, are inserted in the straight sections within the storage ring. Insertion devices are of two kinds: wigglers and undulators. When passing through such alternating magnetic field structures, the Lorentz force causes the electrons to wiggle in the transverse direction. The motion is thus accelerated and stimulates the emission of

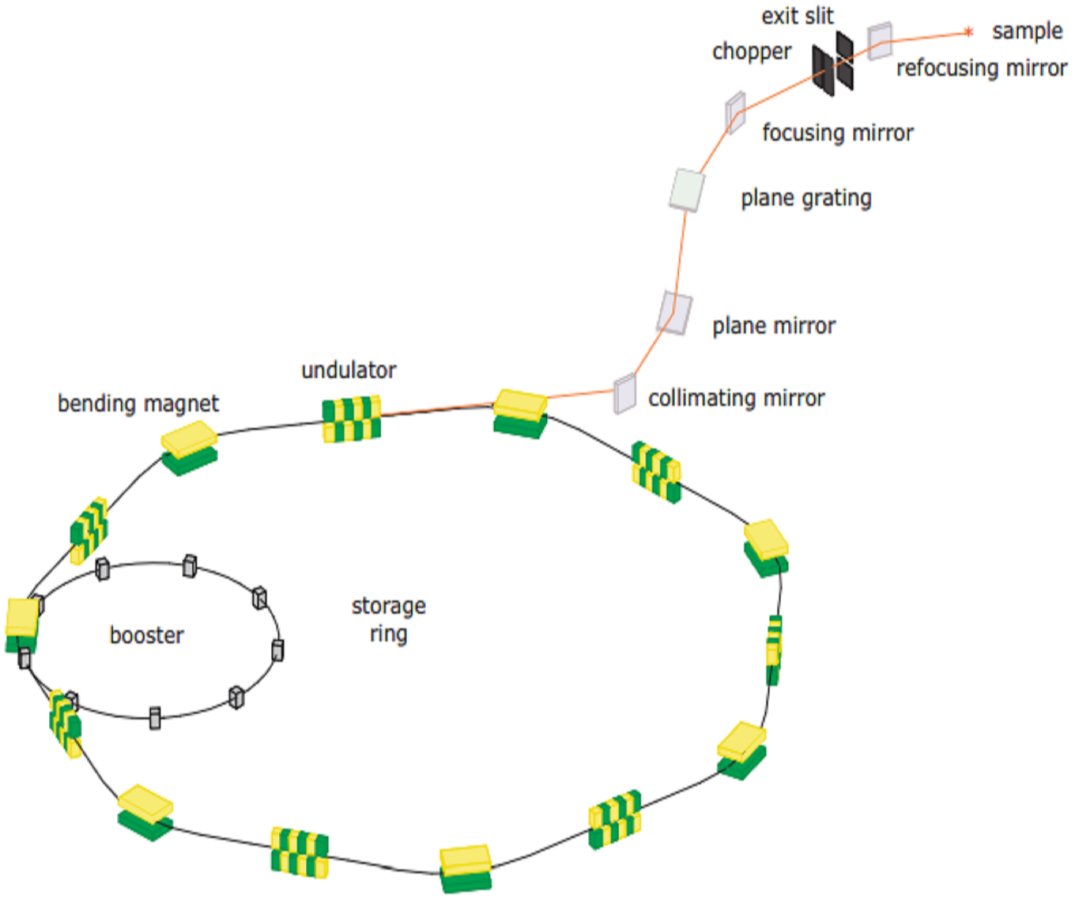

Figure 3.4: Schematic view of a synchrotron radiation facility.

synchrotron radiation during each individual wiggle. The effects of the insertion devices are the following [69]:

- shift of the critical energy to higher values due to the smaller bending radius with respect to the bending magnets;
- increase of the intensity of the radiation by a factor related to the number of wiggles induced by the many poles of the magnetic structure;
- relevant increase of the spectral brightness[1].

Radio frequency system

In order to replenish the energy dissipated due to the emission of radiation at the bending magnets and insertion devices and keep the electrons at a constant energy, special accelerating cavities, called radio frequency (RF) cavities, are used. The RF cavities are

[1]The brightness is expressed as a function of the $number\,of\,photons/second/mm^2\,source\,area/mrad^2/0.1\%\,bandwidth$.

placed along the storage ring, producing an accelerating electric field in synchronism with the arrival of electrons. Note that the acceleration precisely compensates the energy lost with the emission of synchrotron radiation. The electric fields oscillate at frequencies of the order of 500 MHz and proper acceleration takes place only when electrons pass through the cavity at a specific time which is the reason for the bunched character of the circulating electron beam. The circulating beam is made of one or more electron clusters, called bunches, where the distance between bunches is an integer multiple of the RF wavelength. For the same reason, the circumference also must be an integer multiple of the RF wavelength [70].

3.2.3.3 Synchrotron radiation properties

Synchrotron radiation has a number of properties:

- a wide spectral range from infrared to hard X-rays;
- high intensity;
- collimation of the emitted radiation in the instantaneous direction of flight of the emitting particles;
- high degree of polarization: linear polarization with the electric vector parallel to the plane of the orbit and circular polarization above and below the plane of the orbit;
- high brightness of the source because of the small cross section of the electron beam;
- a time structure with pulse lengths down to 100 ps and less;
- all the properties of the source are quantitatively calculable;
- ultrahigh vacuum environment and high beam stability.

Due to the advanced designs and beam control of third generation light sources, source size and divergence have been greatly improved. Nowadays for many experiments, like the ones involving imaging or microscopy, the beam has to be focused down to very small spots and so a relevant synchrotron radiation property becomes its spectral brightness. Undulators are excellent sources of high brightness radiation. This is shown in figure 3.5, where the gain in brightness achieved by the new synchrotron radiation sources, as a function of time, is shown; its increase of many orders of magnitude gives an idea of the spectacular progress obtained in beam quality by third generation sources. Therefore, these photon sources are of ultimate interest for photoemission spectroscopy due to the outstanding characteristics of the synchrotron radiation.

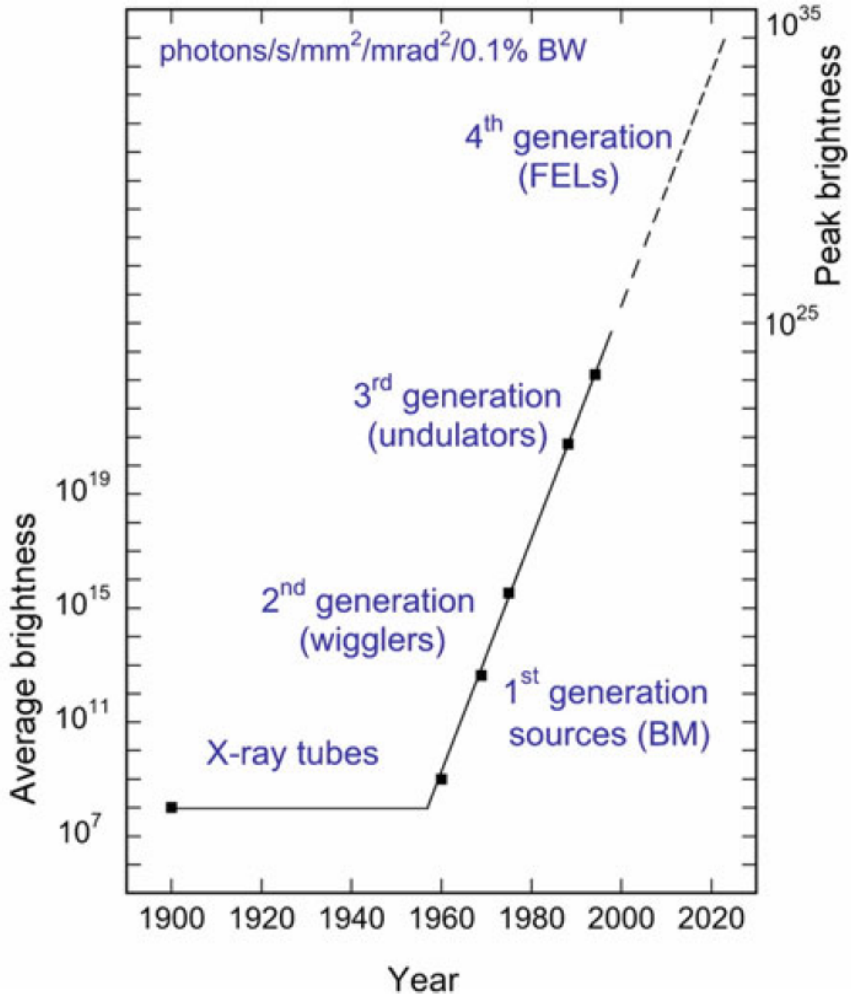

Figure 3.5: Comparison between the average brightness of storage rings of different generations. From [69].

3.2.4 XPS on the APE beamline at Elettra

Advanced photoelectric effect (APE) experiment beamline is located at the Elettra synchrotron radiation facility in Italy. The beamline has been designed with the specific target of matching the characteristics of a surface science laboratory with a fully optimized synchrotron radiation source, resulting in a facility for advanced experiments on solid surfaces. The APE beamline uses photons with chosen polarization emitted simultaneously by two noncollinear insertion devices and delivered in two distinct branches able to work independently. The branch dedicated to high resolution PES uses low energy (LE) photons ($h\nu$ = 8–120 eV) (APE-LE). The second branch exploits photons in the range of $h\nu$ = 150–1600 eV (APE-HE, HE = high energy) and is mainly dedicated to perform soft X-ray absorption (XAS), magnetic dichroism (XMCD, XMLD) and XPS

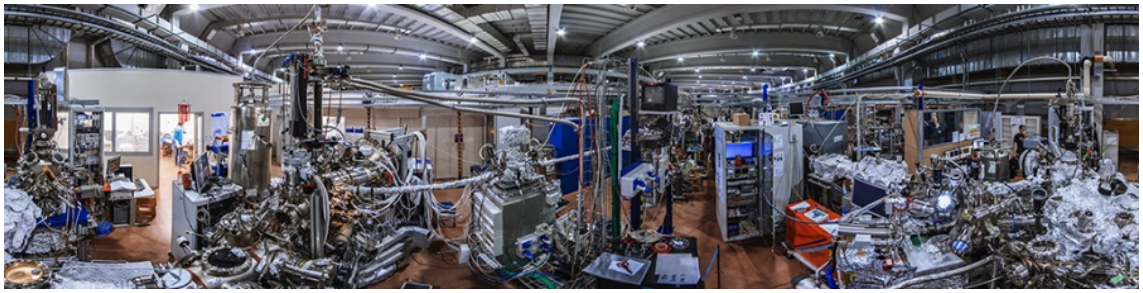

Figure 3.6: A panoramic photography of APE beamline at Elettra synchrotron.

studies. The two branches are shown in figure 3.6. The sample can be cooled down to 16 K (30 K) via a liquid-He flow cryostat at APE-LE (APE-HE).

In the LE end station, the monochromatic light is focused onto a $50 \times 150\ \mu m^2$ spot on the sample. Core level photoemission is possible up to 120 eV. The photon flux at best resolution (10 μm slits) is $> 2 \times 10^{11}$ photons/s on the sample. The LE end station hosts a VG-Scienta DA30 electron energy analyzer that operates in deflection mode and allows for detailed k-space mapping at fixed sample geometry (fixed angle). The overall energy resolution (photons + analyzer + temperature) is $\sim$6 meV, while the angular resolution is $< 0.2^{\circ}$.

In this manuscript, the shallow core XPS study on the Sb_2Te system was performed on the LE branch with the experimental setup illustrated in figures 3.7(a) and 3.7(b).

3.3 Angle-resolved photoemission spectroscopy (ARPES)

3.3.1 Fundamental concepts

The geometry for an ARPES experiment is shown in figure 3.8(a): an incoming photon with energy $h\nu$ impinge on the surface of a sample causing the emission of an electron with a kinetic energy E_{kin}. An electron energy analyzer, characterized by a finite acceptance angle, collects the photoelectrons and measures the kinetic energy E_{kin} of the detected electrons for a given emission direction described by the angles ϑ and φ. The aim is then to determine the electronic dispersion relations for the solid, i.e. the relation between: (i) binding energy E_B, and (ii) wave vector $\boldsymbol{k}$ of the electrons propagating *inside* the crystal, starting from the kinetic energy E_{kin} and the emission angles of the ejected electrons on the *vacuum* side.

(i) **Binding energy:** Within the non-interacting electron picture and according to the energy conservation law, the relation between the kinetic energy E_{kin} of the emitted electron and the binding energy E_B of the electronic-state inside the solid is

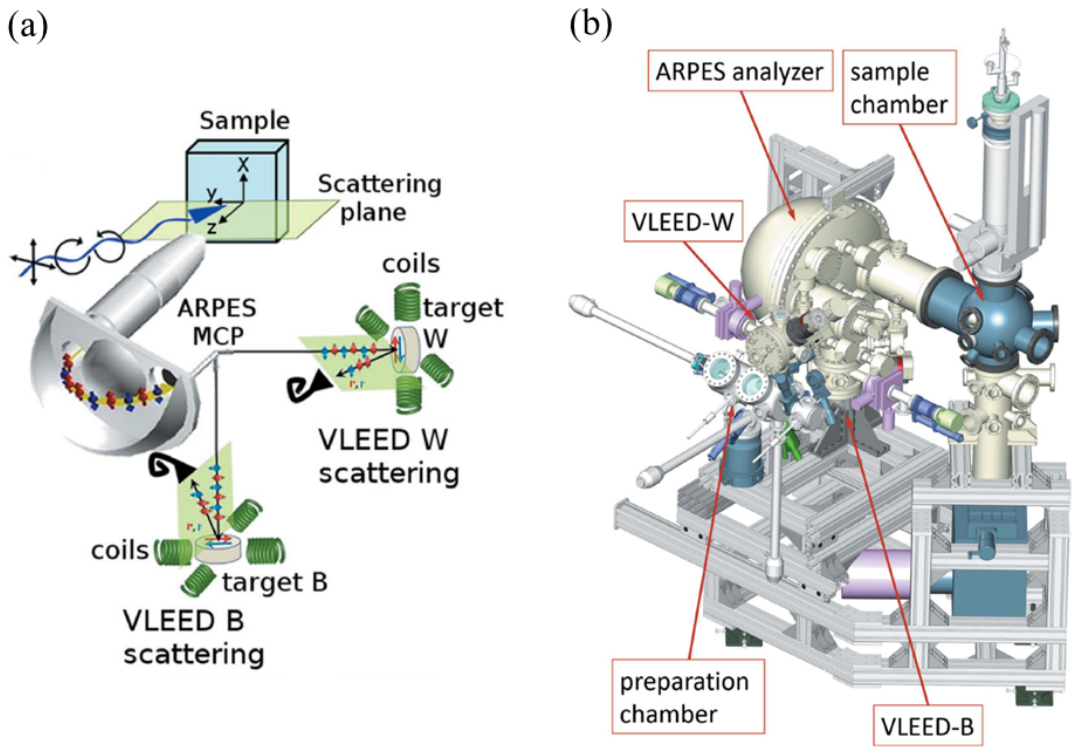

Figure 3.7: Experimental geometry scheme of the APE-LE end station. (a) Polarized monochromatic synchrotron radiation is traveling at 45° with respect to the analyzer lens axis, in the horizontal plane of the storage ring, while the analyzer slit is perpendicular to it. (b) Three dimensional view of the APE-LE end station. From [71].

pictorially illustrated in figure 3.8(b) and quantitatively described by:

$$E_{kin} = h\nu - \phi - |E_B| \tag{3.4}$$

where ϕ = E_V - E_F is the work function of the material, E_V is the vacuum level and E_B is the (positive) binding energy referred to the Fermi level E_F.

(ii) **Wave vector *k*:** The wave vector $\boldsymbol{K}$ of the external electrons on the vacuum side is determined by: its modulus $K = \sqrt{2mE_{kin}/\hbar^2}$, and its components parallel ($\boldsymbol{K}_{||}$ = $\boldsymbol{K}_x$ + $\boldsymbol{K}_y$) and perpendicular ($\boldsymbol{K}_{\perp}$ = $\boldsymbol{K}_z$) to the surface of the crystal which are calculated in terms of the polar (ϑ) and azimuthal (φ) emission angles specified by the experimental set up:

$$K_x = \sqrt{\frac{2m}{\hbar^2} E_{kin}} \sin\vartheta \cos\varphi, \tag{3.5}$$

$$K_y = \sqrt{\frac{2m}{\hbar^2} E_{kin}} \sin\vartheta \sin\varphi, \tag{3.6}$$

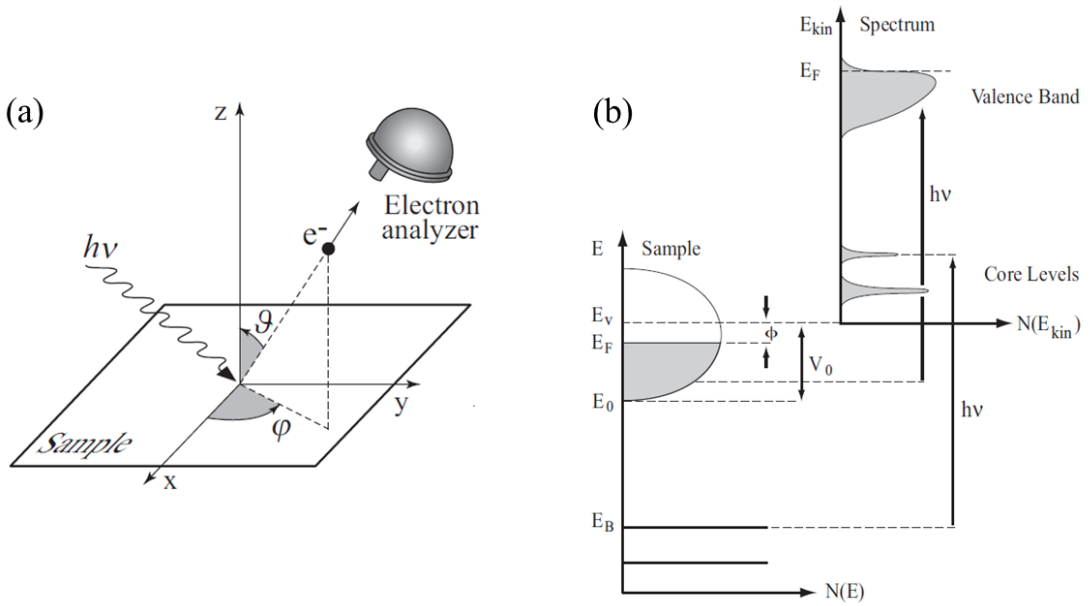

Figure 3.8: Description of an ARPES experiment. (a) Geometry of the ARPES technique in which the emission angles, i.e. the polar (ϑ) and the azimuthal (φ), of the photoelectron are defined. (b) Electrons with binding energy E_B can be excited into free-electron states above the vacuum level E_V by incident photons with energy hν. The electron energy distribution measured as a function of the kinetic energy E_{kin} of the ejected electrons (right) constitutes an image of the occupied density of states N(E_B) inside the solid (left). From [53].

$$K_z = \sqrt{\frac{2m}{\hbar^2} E_{kin}} \cos\vartheta. \tag{3.7}$$

Because of the 2D translational symmetry, the transmission of the electrons across the surface into the vacuum side requires the conservation of the wave vector component parallel to the surface:

$$\boldsymbol{K}_{||} = \boldsymbol{k}_{||} + \boldsymbol{G}_{||} \tag{3.8}$$

where $\boldsymbol{G}_{||}$ is the reciprocal-lattice vector.

If we consider the first Mahan cone $\boldsymbol{G}_{||} = 0$ [72], as $K_{||} = K \sin\vartheta$ one obtains:

$$K_{||} = k_{||} = \sqrt{\frac{2m}{\hbar^2} E_{kin}} \sin\vartheta \tag{3.9}$$

which numerically gives:

$$k_{||} = 0.512\,(\text{Å}^{-1}) \sqrt{E_{kin}\,(\text{eV})} \sin\vartheta. \tag{3.10}$$

Note that at low photon energies in the ultraviolet ($h\nu < 100$ eV), one can completely neglect the photon wave vector in equation 3.9, as it is much smaller than the typical Brillouin-zone dimension 2π/a of a solid [73].

On the other hand, the wave vector component normal to the surface $\boldsymbol{k}_\perp$ of the electrons inside the solid, which is not conserved upon transmission through the surface due to the inner microscopic potential V_0, is also needed in order to map the electronic dispersion $E(\boldsymbol{k})$. The calculation of $k_\perp$ requires the determination of V_0, which can be obtained either experimentally[2] or from theoretical calculations of the band structure. The electron energy within the crystal $\hbar^2k^2/2m$ is equal to the sum of the kinetic energy E_{kin} outside the solid, referenced to the vacuum level E_V, and the inner potential V_0:

$$\frac{\hbar^2}{2m}(k_{||}^2 + k_\perp^2) = E_{kin} + V_0 \tag{3.11}$$

which makes it possible to obtain, using the equation 3.9, the perpendicular wave vector in the final state:

$$k_\perp = \sqrt{\frac{2m}{\hbar^2}(E_{kin}\cos^2\vartheta + V_0)}. \tag{3.12}$$

A special case where the uncertainty in $\boldsymbol{k}_\perp$ is less relevant is that of the low-dimensional materials in which the electronic structure is usually anisotropic and the electronic dispersion perpendicular to the surface, i.e. along the z axis, is almost negligible.

Therefore, ARPES is the main experimental technique to measure simultaneously the binding energy and the wave vector of electrons in a solid, namely, the electronic band dispersion.

3.3.2 Three-step model

A rigorous theoretical approach to the photoemission process requires a full quantum-mechanical description of the entire coherent process in which an electron is removed from an occupied electronic state within the crystal and deposed at the detector. Theoretical approaches of this kind treat the *one-step model* [74, 75, 76]. The less accurate but simpler approach is the so-called *three-step model* in which the photoemission pro-

[2] The most appropriate experimental method is to detect photoelectrons ejected along the surface normal ($\boldsymbol{K}_{||} = 0$) while varying the incident photon energy and, in turn, the E_{kin} of the emitted electrons and thus K_z (see equation 3.7).

cess is artificially broken up into three independent and sequential steps [77, 78, 79] (see figure 3.9):

(i) Optical excitation of the electron from an initial into a final electronic state within the solid.

(ii) Propagation of the excited electron to the surface.

(iii) Escape across the surface: emission of the electron from the crystal into the vacuum.

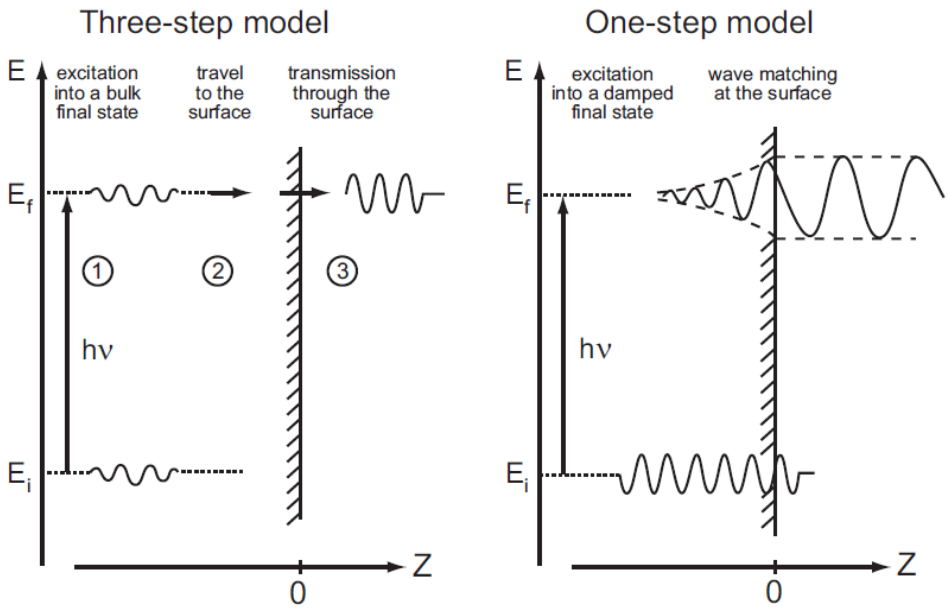

Figure 3.9: Illustration of the three-step and the one-step model in the photoemission process. The three-step model consists of three successive steps: optical absorption, electron transport, and transmission across the surface into the vacuum. In the one-step process, one considers the excitation from an initial state (Bloch wave in the solid) into a damped final state near the surface, the damping taking care of the short mean free path of the electrons in the crystal. From [80].

In principle, these distinct steps are not independent of each other. However, the one-step theory actually gives results that are not very different from the three-step model. In the following, I will discuss each step in detail.

Step (i): Optical excitation of the electron in the solid

In first-order perturbation theory, the photoexcitation of an electron is described by the transition probability w_{fi}, given by Fermi's Golden Rule, for an optical excitation between the N-electron initial state Ψ_i^N and one of the feasible final states Ψ_f^N:

$$w_{fi} = \frac{2\pi}{\hbar} |\langle \Psi_f^N \mid H_{int} \mid \Psi_i^N \rangle|^2 \delta(E_f^N - E_i^N - h\nu) \tag{3.13}$$

where E_i^N and E_f^N are respectively the energies of the initial and the final state of the N-particle system. H_{int}, the Hamiltonian for the interaction between an electron and electromagnetic radiation, is given by the electronic momentum operator **p** and the vector potential **A** of the incident electromagnetic wave:

$$H_{int} = \frac{e}{2mc}(\mathbf{A}\cdot\mathbf{p} + \mathbf{p}\cdot\mathbf{A}) = \frac{e}{mc}\mathbf{A}\cdot\mathbf{p}. \tag{3.14}$$

In equation 3.14, we made use of the commutator relation [**p**, **A**] = $-i\hbar\nabla\cdot\mathbf{A}$ and dipole approximation, i.e. **A** is nearly constant in the long wavelength limit (in UPS: $\lambda > 100$ Å) and therefore **A** can be assumed to commute with **p** ($\nabla\cdot\mathbf{A} = 0$).

Step (ii): Propagation of the electron to the surface

A large number of electrons lose part of their energy E_f by undergoing inelastic scattering mechanisms, i.e. electron-electron, electron-phonon and electron-plasmon interactions. These electrons have lost the information about their initial electronic level E_i; they contribute to the continuous background in the photoemission spectrum, called the true secondary background, which is usually subtracted. The probability that an excited electron will reach the surface without inelastic scattering and thus without suffering any change in its kinetic energy and momentum is obtained phenomenologically by the inelastic mean free path (IMFP) λ.

Assuming that the scattering frequency $1/\tau$ (τ is the lifetime) is isotropic and depends only on the energy E (which involves adjusting the energy window of the electron analyzer), the electron inelastic mean free path $\lambda(E)$, which represents the mean distance between successive inelastic collisions, is given by:

$$\lambda(E) = \tau v_g = \frac{\tau}{\hbar}\frac{dE}{dk} \tag{3.15}$$

where v_g is the group velocity in the final state.

The inelastic scattering results in an energy dependence of λ, which is described by the well-known "universal curve" having a broad minimum on the order of few Å for kinetic energies of electrons between 20 and 100 eV (figure 3.10). This dependence is quite similar for a large number of different materials. Since the probability that an electron, created at the distance z from the surface, travel in the sample without undergoing a scattering process varies in terms of $\exp(-z/\lambda)$, the photoemission only probes a thickness in the order of λ under the surface which makes it a surface sensitive technique[3]. On the other hand, the knowledge that λ depends on the energy allows tuning of the electron

[3] The surface sensitivity has important technical consequences as it requires surface preparation and ultrahigh vacuum technology to maintain the surfaces clean as long as possible (section 3.3.3.1).

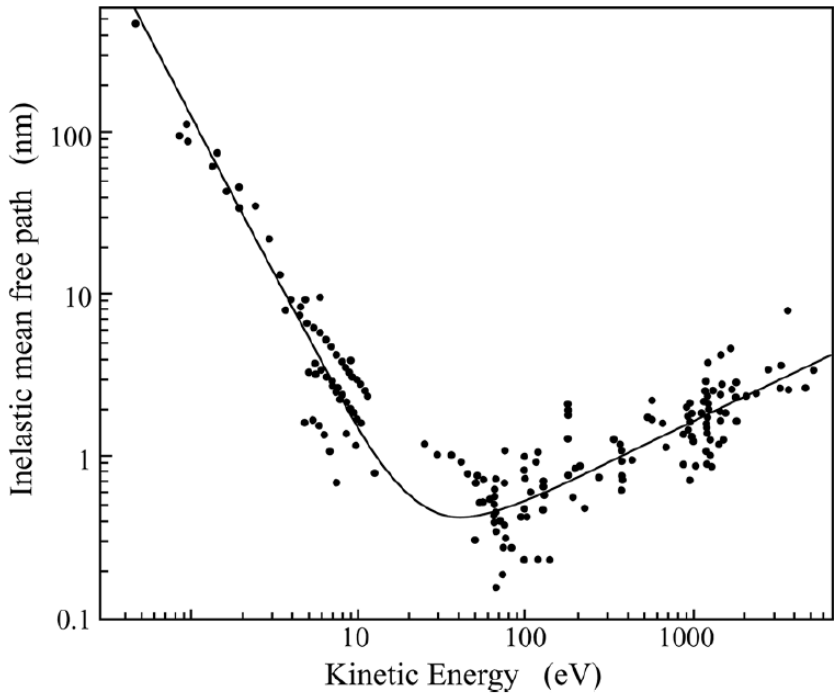

Figure 3.10: Inelastic mean free path of excited electrons in solids as a function of their kinetic energy. From [81].

kinetic energy to enhance or suppress the surface or bulk contributions. Thus, to be less surface sensitive, it is necessary to use either high energy photons (several keV) or very low energy photons[4] (less than 10 eV).

Step (iii): Escape of the electron across the surface into the vacuum

In the third step, the transmitted electrons into the vacuum are those for which the component of the kinetic energy normal to the surface is sufficient to overcome the surface potential barrier; the other electrons are completely reflected back into the bulk. Inside the solid, the electron travels in an inner potential V_0 of depth $|E_0| + \phi$, where E_0 (< 0) is the energy of the bottom of the valence band (as shown in figure 3.8(b)). In order to have any finite escape probability, the electrons must satisfy the condition:

$$\frac{\hbar^2}{2m} k_\perp^2 \geq V_0. \tag{3.17}$$

[4] From equation 3.10, one can determine the wave vector resolution:

$$\Delta k_{||} = 0.512\,(\text{Å}^{-1})\,\sqrt{E_{kin}\,(\text{eV})}\,\cos\vartheta\,\Delta\vartheta. \tag{3.16}$$

The equation 3.16 shows that, at the same finite acceptance angle of the electron analyzer $\Delta\vartheta$, the wave vector resolution is better at lower photon energies (i.e. lower E_{kin}) which is the opposite for high energy photons.

To conclude, the three-step model makes the photoemission process quite comprehensible and easy to discuss, it is a very useful and accurate approximation.

3.3.3 Experimental aspects

3.3.3.1 Ultrahigh vacuum

In the UV regime, photoemission spectroscopy is highly surface sensitive and thus suitable for surface studies because of the limited escape depth of electrons. The preparation of "clean" surfaces, on which surface studies are typically performed, became possible only after the development of UltraHigh Vacuum (UHV) techniques. In order to keep the surface fairly fresh and clean at room temperature over a period of the order of an hour (experimental time allowing to measure a clean surface), it is therefore essential to have a vacuum with a residual gas pressure lower than 10^{-10} mbar. Under these UHV conditions, the contamination effects (monolayers of adsorbate) can be neglected for experiments on clean "virgin-like" solid-vacuum interfaces [82].

3.3.3.2 Hemispherical analyzer

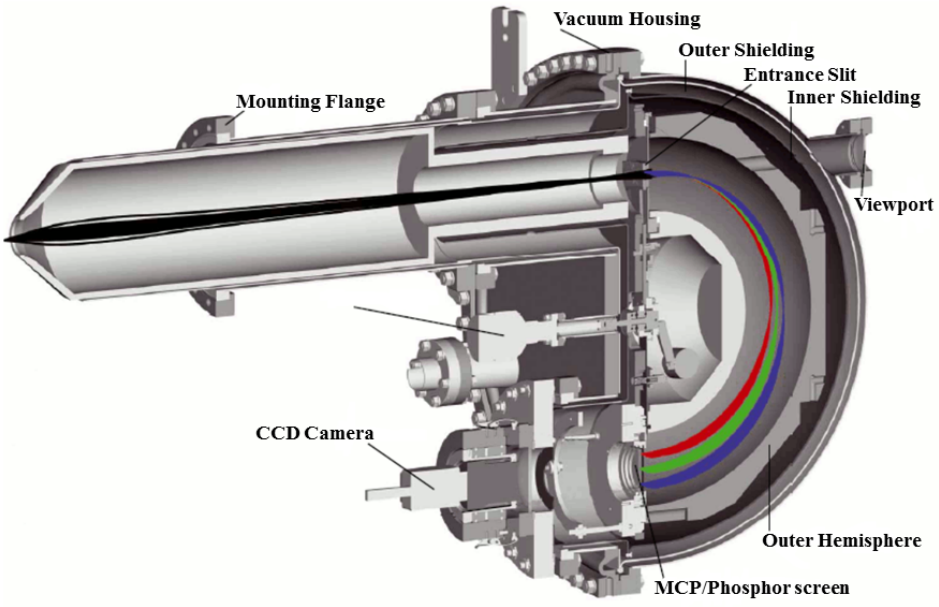

Figure 3.11: Illustration of an hemispherical analyzer.

One of the main equipment of an ARPES experiment is the hemispherical analyzer, illustrated in figure 3.11, which collects photoemitted electrons and performs spectroscopic

energy measurements due to energy dispersion. A conventional hemispherical analyzer, with a mean radius R_0, is equipped with a multi-element electrostatic input lens system, a hemispherical deflector with entrance and exit slits, and an electron detector (a multi-channel detector). Electrons entering through an entrance slit S_1 are deflected to elliptical trajectories by the radial electrical field between the inner R_{in} and the outer R_{out} hemispheres of the hemispherical analyzer. The entrance slit S_1 and exit plane S_2 are centered on:

$$R_0 = \frac{R_{in} + R_{out}}{2}. \tag{3.18}$$

For a fixed electrical field gradient, only electrons with kinetic energies in a certain energy range are allowed to pass the full deflection angle from the entrance slit and reach the exit slit and then the detector without colliding with the inner walls of the analyzer. Note that electrons with higher kinetic energy are deflected toward the outer hemisphere, whereas those with lower kinetic energy approach the inner hemisphere. The nominal pass energy E_{pass} of the electrons traveling through the hemispheres on the central circular trajectory is given by:

$$E_{pass} = (-q)\, k \Delta V \tag{3.19}$$

where q is the charge of the electron, the potential difference $\Delta V = V_{out}$ - V_{in} applied to the hemispheres, and k is the calibration constant defined by:

$$k = \frac{R_{in} R_{out}}{2R_0 (R_{out} - R_{in})}. \tag{3.20}$$

If the hemispherical analyzer accepts the half angle α in the dispersion direction, the electron analyzer energy resolution or full width at half maximum (FWHM) of the transmitted line ΔE_{an} is:

$$\frac{\Delta E_{an}}{E_{pass}} = \frac{S}{2R_0} + \frac{\alpha^2}{4} \tag{3.21}$$

where $S = (S_1 + S_2)/2$ [83]. This value is an analyzer constant.

In addition, the spectrometer and the sample are connected to ensure that their Fermi energies are at the same reference level (as represented in figure 3.12). An energy E'_{kin} is measured by the spectrometer. After calibrating the work function of the spectrometer, the binding energy of the specimen with respect to the Fermi level can be determined without knowing its work function because

$$E_{kin} + \phi = E'_{kin} + \phi' \tag{3.22}$$

where ϕ and ϕ' are the work functions of the material and the spectrometer, respectively.

In the FemtoARPES setup, described later in section3.4.2, we have an hemispherical

energy analyzer Phoibos 150 of Specs. This instrument records ARPES spectra with an angular resolution < 0.15° and energy resolution < 10 meV. The electrostatic lenses allow us to change the angular acceptance (from ±3° to ±14°) and the kinetic energy range.

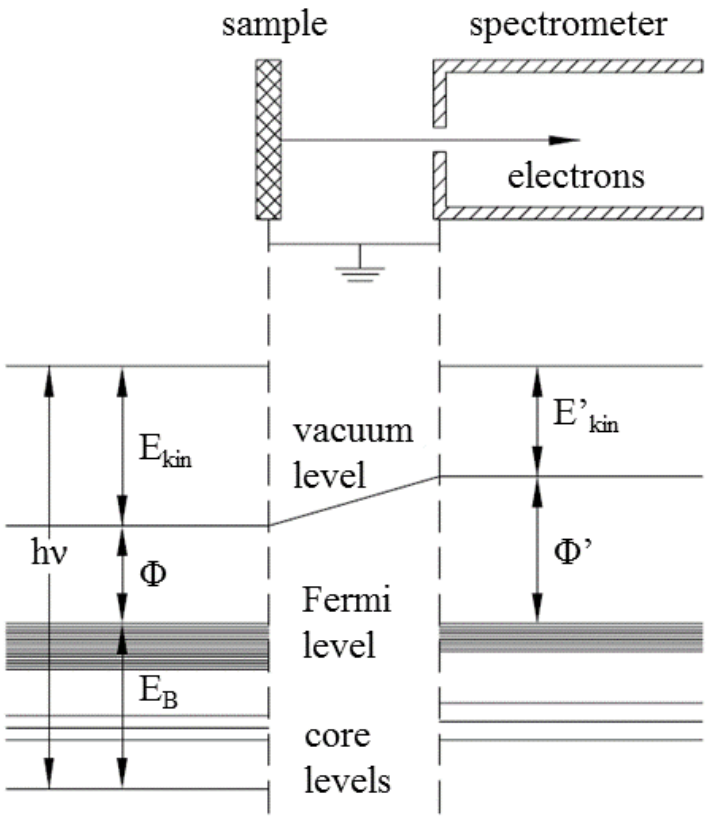

Figure 3.12: Energy level diagram for a sample in electrical contact with a spectrometer.

3.4 Time-resolved ARPES (trARPES)

3.4.1 Fundamental concepts

Recently, laser-based instruments have been developed to carry out photoemission. These compact laser based light sources possess characteristics and parameters that are out of reach for conventional sources of radiation used for ARPES, e.g. gas-discharge lamps offering continuous wave radiation or synchrotron sources providing pulsed beams with a duration on the order of 100 ps. First, lasers with very narrow linewidths have been employed for high energy resolution (better than 1 meV) photoemission studies [85]. Second, two femtosecond laser pulses can be used for performing time-resolved angle-resolved photoemission spectroscopy (trARPES) via a pump-probe configuration: as de-

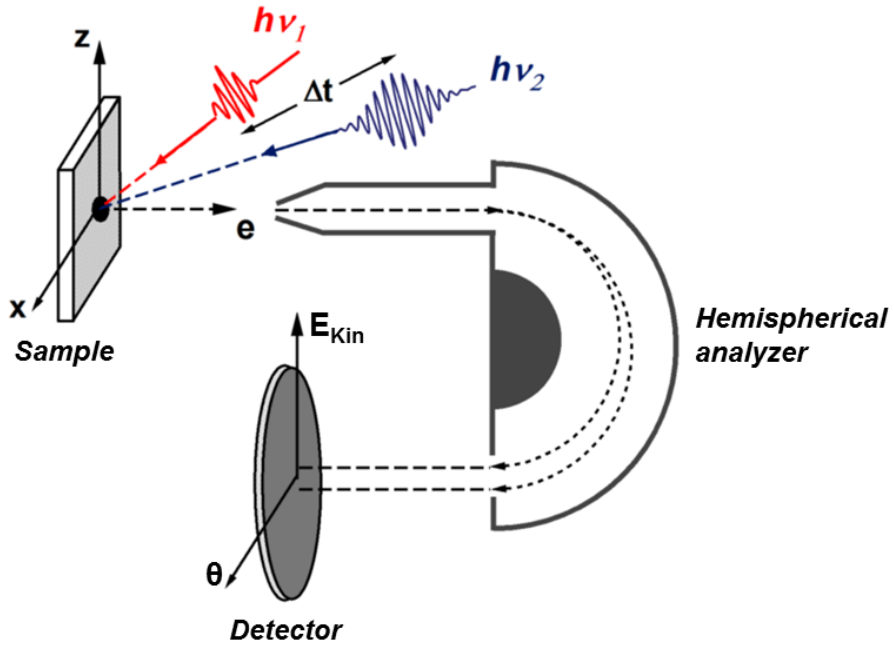

Figure 3.13: Schematic representation of a trARPES experimental setup. $h\nu_1$ and $h\nu_2$ are the pump and probe beams, respectively. From [84].

picted in figure 3.13, a femtosecond pump pulse ($h\nu_1$), typically infrared in frequency, creates a non-equilibrium excited state by driving the low energy electrons into empty electronic states, while a probe pulse ($h\nu_2$)—generally ultraviolet—photoemits excited electrons outside the sample into an electron analyzer where their kinetic energies and emission angles are measured. Varying the time delay between the pump and the probe pulses (represented as Δt in figure 3.13) makes it possible to study the temporal evolution of the transient electron population and the time-dependent processes (electron-electron scatering, electron-phonon interaction and diffusion) involved in the relaxation of the out-of-equilibrium excited state with a femtosecond time precision [86]. By gradually delaying the arrival time of the probe with respect to the pump, we can assemble a "film" of the occupied and unoccupied electronic band structure of the sample: this allows us to observe the dynamics in solid-state systems like topological insulators when they are out-of-equilibrium.

In a time-resolved study, the short-pulsed laser source has to fulfill several conditions [87]:

(i) The photon energy of the ultraviolet pulse should be higher than the work function of the material so that excited electrons can escape the surface.

(ii) To time-resolve the ultrarapid scattering processes which result in energy and momentum relaxation, the probe pulse has to be shorter than 100 fs.

(iii) In order to obtain fast data acquisition with good statistics, the photon flux should be high enough (10^{12} photons/s).

(iv) To avoid problems related to space charge effect while preserving a high photon flux, it is necessary to work with a high repetition rate of the laser source (> 100 kHz).

The time-resolved experimental measurements presented in this manuscript were carried out using the FemtoARPES setup, located at SOLEIL, in the framework of a collaboration of three partners of this project: Laboratoire de Physique des Solides (Université Paris-Sud), Laboratoire des Solides Irradiés (Ecole Polytechnique), and SOLEIL. Next, I will provide a detailed description of this setup.

3.4.2 FemtoARPES setup

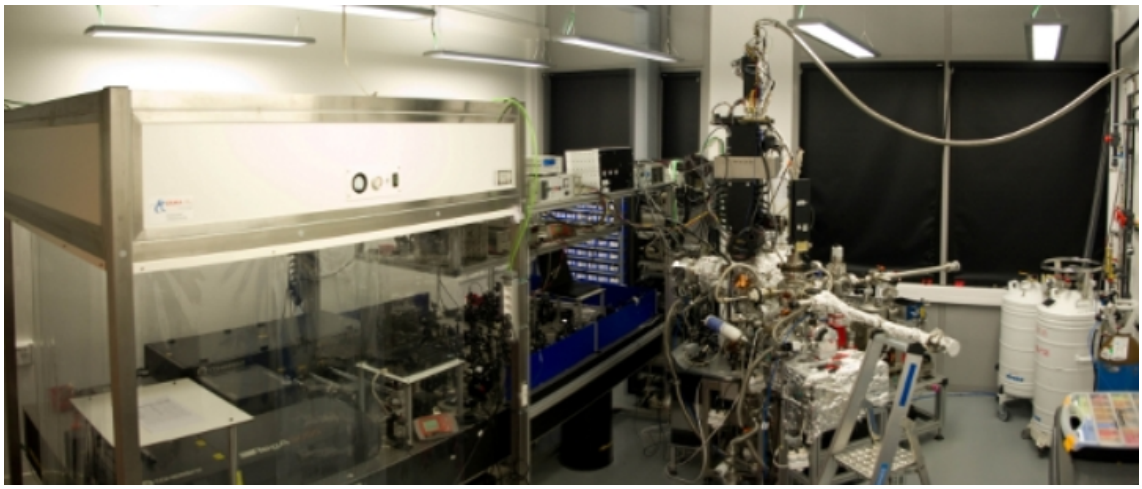

Figure 3.14: The FemtoARPES experimental setup located at the SOLEIL synchrotron.

The FemtoARPES setup is conceived to perform trARPES studies with a femtosecond time resolution (figure 3.14). The experimental setup is composed of a sample placed on a 5-axis manipulator (x, y, z, θ and ϕ) which is connected to a cryostat so that the sample can be cooled down to 35 K using liquid helium or to 130 K by means of liquid nitrogen inside an ultrahigh vacuum chamber (base pressure of a few 10^{-11} mbar to ensure a relatively long lifetime of the clean surfaces that are analyzed). As shown in figure 3.15, the sample is placed in front of a hemispherical electron analyzer and irradiated with two pulsed laser beams in a pump-probe configuration.

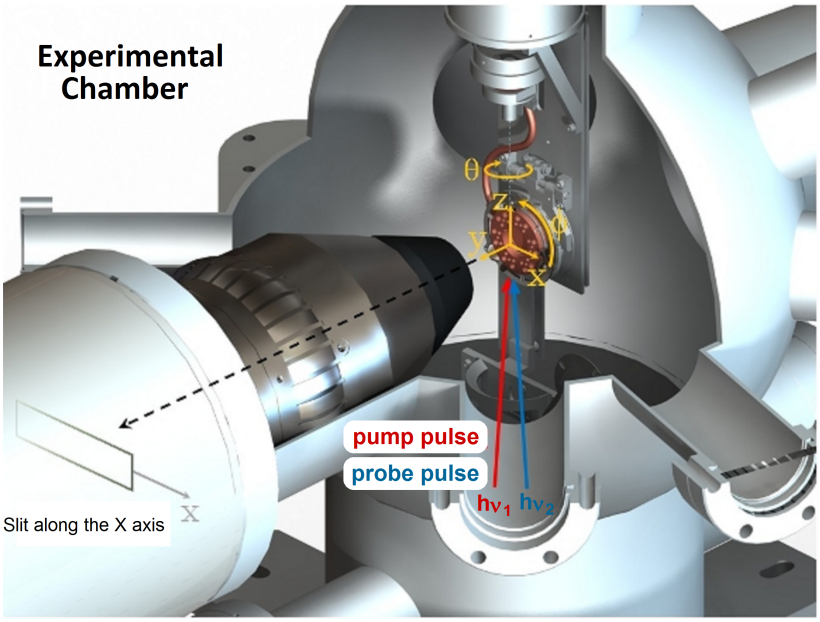

Figure 3.15: Pump-probe configuration of the FemtoARPES setup.

The laser system consists of a commercial Ti-Sapphire laser by Coherent made up of a Micra oscillator pumped by a Verdi laser (at 523 nm), and a RegA amplifier. Note that a Silhouette phase modulator allows us to measure and modify the temporal shape of the laser pulses. The laser source delivers 35 fs pulses (6 μJ per pulse) centered at 1.58 eV photons energy with a repetition rate of 250 kHz (figure 3.16(a)). As illustrated in figure 3.16(b), the fourth harmonic of 6.32 eV is generated by cascade frequency mixing in BBO non-linear crystals (β-BaB_2O_4) from the 1.58 eV initial output laser power that is used to pump the transient populated band structure [88]. Both 1.58 eV pump and 6.32 eV probe beams are focused almost collinearly at an angle of 45° with respect to the surface normal. The time between the pump and the probe is called delay and can be modified using a retarding stage. The pump-probe photoemission measurements can be performed with an overall temporal resolution of 80 fs and an energy resolution of 60 meV. (A full description of our experimental setup and of its specifics can be found in [87, 89].) The use of a 6.32 eV probe gives access to a narrow portion of k-space (typically $k_{||} < 0.5$ Å^{-1}), but sufficient in the case of Bi_2Te_3 and Sb_2Te to observe their unoccupied surface states at the $\bar{\Gamma}$ point.

3.4.3 Ultrafast carrier dynamics

On photoexcitation with an ultrashort laser source, a material undergoes various stages of relaxation before going back to its initial equilibrium state. The energy is transferred

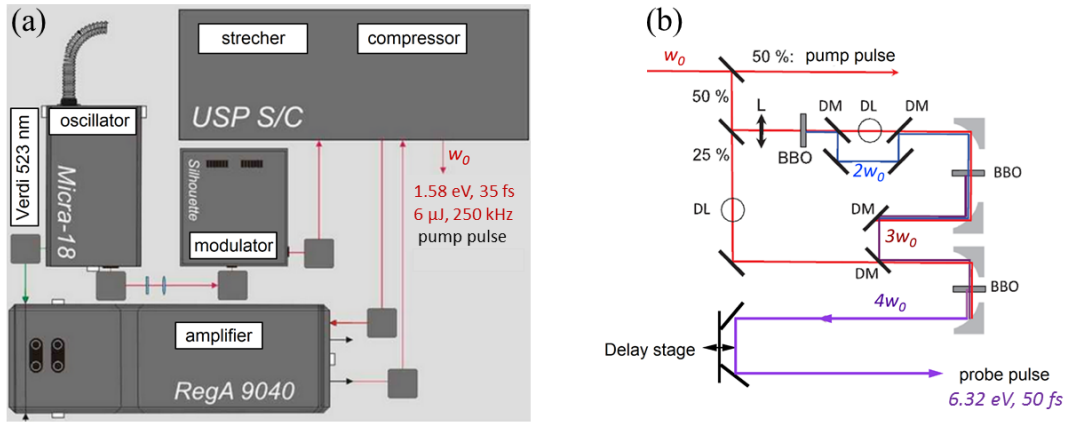

Figure 3.16: The laser source of the FemtoARPES setup. (a) A commercial Ti-Sapphire laser system generates 35 fs pulses (6µJ per pulse) centered at 1.58 eV photons energy at 250 kHz repetition rate (pump pulse). (b) Schematic for fourth harmonic generation by means of non-linear beta barium borate (BBO) crystals (probe pulse). L: lens with f = 20 cm, DM: dichroic mirror and DL: delay line.

first to the electrons and then to the lattice. The interaction process involves different regimes of carrier excitation and relaxation. We can discern four distinct regimes: (i) carrier excitation, (ii) thermalization, (iii) carrier removal, and (iv) structural and thermal effects. Figure 3.17 depicts a schematic diagram of the approximate timescales of various electron and lattice dynamical processes in solids over a range of carrier densities from 10^{17} to 10^{22} cm^{-3}. Several mechanisms of the electron dynamics through this regimes are elaborated in the following paragraphs.

3.4.3.1 Carrier excitation

Interband single photon absorption (figure 3.18(a), left) is the dominant process for exciting electrons from the valence band (VB) to the conduction band (CB) when the photon energy is larger than the smallest direct bandgap, i.e. the smallest gap between valence and conduction bands having the same wave vector $\boldsymbol{k}$. Some semiconductors, such as Si, possess an indirect bandgap: the minimum energy state in the conduction band and the maximum energy state in the valence band are each characterized by a certain crystal wave vector $\boldsymbol{k}$ in the Brillouin zone. In this case, single photon absorption can still take place with photons of energy greater than the gap, but phonon assistance is imperative to conserve momentum. Conservation of crystal wave vector yields: $\boldsymbol{k}_{VB} = \boldsymbol{k}_{CB} \pm \boldsymbol{q}$, where $\boldsymbol{q}$ is the phonon wave vector. Multiphoton absorption (figure 3.18(a), right) can be important if the direct gap is greater than the energy of the photon (e.g. transparent insulators) or if single photon absorption is inhibited by conduction band filling.

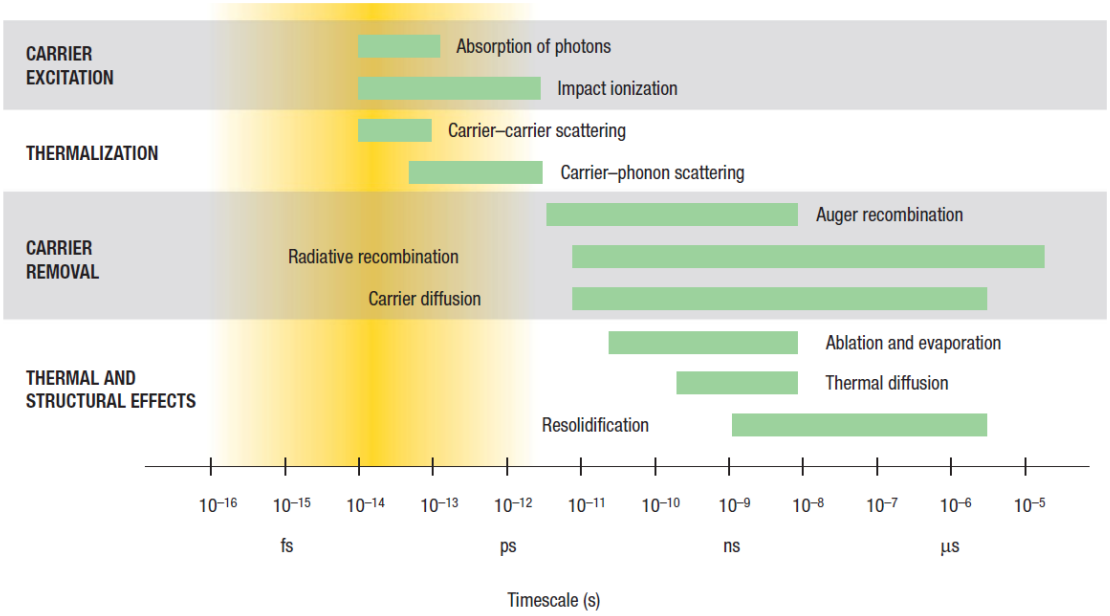

Figure 3.17: Timescale of the physical phenomena in laser-excited solids. The green bars represent an approximate range of characteristic times for the relevant process. Although the absorption of light occurs at the femtosecond timescale, the material can continue to undergo changes microseconds later. From [90].

Once carriers have been generated, they can absorb photons and move to higher energy states (intraband excitation by photons). This free carrier absorption, indicated by figure 3.18(b), increases the energy of carriers in the electron–hole plasma in a semiconductor or that of the initially free electrons in a metal. Although this free carrier absorption increments the energy of the free carrier population, it does not alter the number of free carriers.

If some of the carriers in a semiconductor or insulator are excited to an energy above the bottom of the conduction band that is larger than the bandgap (or Fermi level in a metal), then impact ionization (figure 3.18(c)) can occur. This process is due to the Coulomb interactions between carriers. In fact, an excited electron loses energy and falls lower in the conduction band. Identically, an excited hole can move higher in the valence band. The energy released excites an electron-hole pair. Thus, the impact ionization creates additional excited carriers [91].

3.4.3.2 Thermalization

After photoexcitation, electrons and holes are redistributed throughout the conduction and valence bands via carrier–carrier and carrier–phonon scattering. Both processes will be described in next paragraphs.

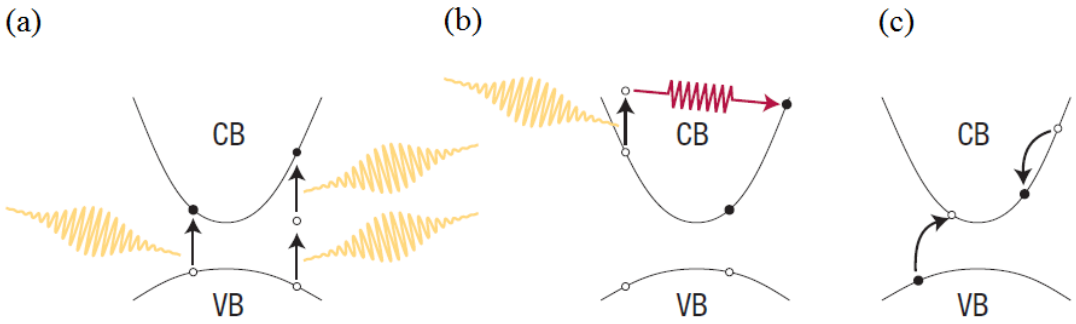

Figure 3.18: Mechanisms for exciting carriers in a direct bandgap material. CB is the conduction band and VB the valence band. The photons are marked in yellow and the phonons in red. (a) Single (left) and multiphoton (right) absorption. (b) Free-carrier absorption. (c) Impact ionization.

Carrier-carrier scattering

Carrier-carrier scattering is a two-body process based on electrostatic interactions between two carriers, which does not modify the total energy in the excited carrier system and the total number of free carriers. Therefore, energy and wave vector conservation laws must be satisfied for single collisions:

$$\boldsymbol{k}_1 + \boldsymbol{k}_2 = \boldsymbol{k'}_1 + \boldsymbol{k'}_2, \tag{3.23}$$

$$E(\boldsymbol{k}_1) + E(\boldsymbol{k}_2) = E(\boldsymbol{k'}_1) + E(\boldsymbol{k'}_2) \tag{3.24}$$

where $\boldsymbol{k}_1$ and $\boldsymbol{k}_2$ are the wave vectors of the two carriers before collision and $\boldsymbol{k'}_1$ and $\boldsymbol{k'}_2$ are their wave vectors afterwards. Figure 3.19(a) reveals intravalley scattering, i.e. carriers remain in the same conduction or valence band valley. Carrier–carrier scattering can cause dephasing in less than 10 fs, but it takes hundreds of femtoseconds for the carrier distribution to approach a Fermi–Dirac distribution.

The scattering of hot electrons [5] from other electrons can be approximated by considering the energy-loss rate of a fast electron with energy E to a cold gas of other electrons of density n. The carrier-carrier scattering rate is obtained from the stopping power of a metal for fast electrons:

$$[\frac{dE}{dt}]_e \approx \frac{4\pi n e^{*4}}{\sqrt{2mE}} \tag{3.25}$$

where n is the electron density, $e^{*2} = e^2/\varepsilon$ is an effective charge and ε is the dielectric of a semiconductor [92]. Note that the scattering rate increases with density. However, at

[5] Out-of-equilibrium electrons which have energies greater than the Fermi level.

high densities, screening effects become important and reduce the Coulomb interactions between carriers. Consequently, the scattering rate does not continue to increase at the same rate with increasing density, and the rate could decrease with density after some point.

Carrier-phonon scattering

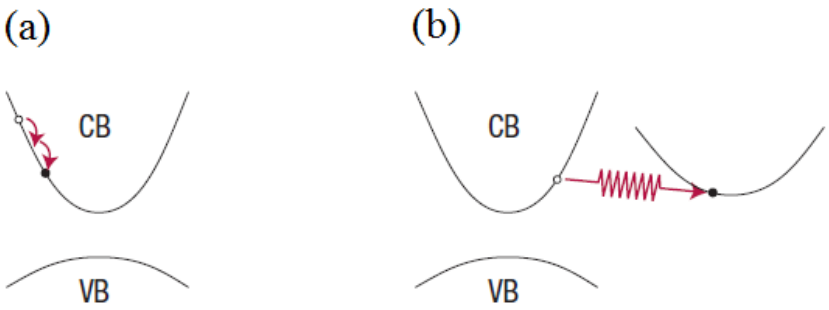

Figure 3.19: Carrier scattering mechanisms in a solid. (a) Carrier–carrier scattering. (b) Carrier–phonon scattering.

In a carrier–phonon scattering process (figure 3.19(b)), free carriers lose or gain energy and momentum by emission or absorption of a phonon (or lattice vibration). In crystalline semiconductors, this process is divided into two categories: intravalley and intervalley scattering. In the former case, as mentioned above, the carriers remain in the same valley around a local minimum in the conduction band or a local maximum in the valence band. In the latter case, the carriers transfer to a distinct valley (as represented in figure 3.19(b)). Therefore, the intervalley electron-phonon scattering is considered as one of the most important mechanisms for coupling electrons from the bulk bands into the surface states which are present in a different area of the Brillouin zone. The rate of the intervalley electron-phonon scattering between valleys i and j within a bulk Brillouin zone in homopolar semiconductors, such as Ge and Si, is given by:

$$R(\boldsymbol{k}) = \frac{\pi D_{ij}^2}{\rho_m \omega_{ij}} \{ n_{BE}(\omega_{ij}) N(E_k - \Delta E_{ij} + \hbar\omega_{ij}) + [n_{BE}(\omega_{ij}) + 1] N(E_k - \Delta E_{ij} - \hbar\omega_{ij}) \} \tag{3.26}$$

where D_{ij} is the deformation potential constant, ρ_m is the mass density, $\hbar\omega_{ij}$ is the phonon energy, ΔE_{ij} is the energy difference between the initial and final states in the two valleys and $N(E_k - \Delta E_{ij} \pm \hbar\omega_{ij})$ is the final density of states of the band to which the electron scatters. Basically, the scattering rate is proportional to $n_{BE}(\omega_{ij})$ when a phonon is absorbed and to $n_{BE}(\omega_{ij}) + 1$ when a phonon is emitted, where $n_{BE}(\omega_{ij}) = (e^{\hbar\omega_{ij}/k_B T} - 1)^{-1}$

is the temperature dependent Bose-Einstein (BE) occupation probability. The extension of the above expression to the case where an electron scatters from a bulk state with initial wave vector q_i to a surface state with final wave vector q_j is almost straightforward. For surfaces, a modification to the expression may involve distinct deformation-potential constants and phonon frequencies and constitutes an interesting domain for theoretical studies. The rate given above is temperature-dependent via the BE occupation probability and reveals that a variation of the specimen temperature can be employed to describe the role of phonons in scattering events which include dynamics of surface electrons. In polar materials, such as GaAs, the scattering process is known as the Frö1ich interaction which displays a $1/q^2$ dependence, where q is the phonon wave vector [92].

Although carrier–phonon scattering does not alter the number of carriers, it provokes a net decrease in their energy via a spontaneous phonon emission which transfers energy to the lattice (more phonons are emitted than absorbed). In semiconductors and metals, carrier–carrier and carrier-phonon scattering happen simultaneously during the first few hundred femtoseconds after excitation. Because the emitted phonons carry little energy, it takes many scattering processes, and therefore several picoseconds, before the carriers and the lattice reach thermal equilibrium.

3.4.3.3 Carrier removal

At a well-defined temperature of the material, the carriers and the lattice are in equilibrium. Even though the carrier distribution and the lattice present the same temperature, there is an excess of free carriers with respect to that in the thermal equilibrium. The excess carriers are removed either by recombination of electrons and holes or by diffusion out of the originally excited region in real space that a probe pulse investigates. In contrast to recombination processes, carrier diffusion does not reduce the total number of free carriers in the material. It does, however, remove them out of the excitation region. For carrier densities above $10^{18} cm^{-3}$, experiments and simulations showed that recombination and diffusion both occur on the picosecond timescales. For lower densities, diffusion is frequently the preponderant process for decreasing the excited carrier population, especially if the sample is free of defects, as all recombination mechanisms are slow, typically of the order of nanoseconds or longer. Even at low densities, recombination of the carriers takes place but in an area much larger than the one probed by the laser pulse.

3.5 Scanning photoemission microscopy (SPEM)

3.5.1 Fundamental concepts

In parallel with the development of high energy and momentum resolution PES and ARPES experiments, high spatial resolution PES also attracts considerable interest. By adding spatial resolution, a full characterization of most of the materials that are heterogeneous by nature or by design becomes possible. The advent of high brightness synchrotron radiation sources and the recent improvement of photoelectron microspectroscopes, which give the opportunity to obtain both quantitative and qualitative images of a solid surface components with a very high lateral resolution mapping and negligible irradiation damage effects by combining spectroscopy and high resolution mapping, has triggered the development of high spatial resolution PES. There are two different approaches for this purpose. One approach is the PhotoEmission Electron Microscopy (PEEM). In this case, the lateral resolution is achieved by using an electron optic system that magnifies the images of the illuminated surface region. The other approach is the Scanning PhotEemission Microscopy (SPEM) where the lateral resolution is achieved by focusing the excitation photon beam into an extremely small submicrometric spot using suitable photon optics and the image is obtained by scanning either the sample area or the photon focus region. In this case, standard analyzer can be employed for photoelectron detection. Fresnel zone plates or special spherical mirrors like Schwarzschild objectives (SO) [93] can be used to focus the beam down to a few nanometers. This technique is mainly used in synchrotron radiation facilities because the excellent photon beam quality facilitated such fine focusing. Both approaches present advantages and disadvantages and the choice should be made by considering the specifications of the study that is planned to be performed [94].

In this manuscript, I present SPEM experiments on Sb_2Te performed on the Spectromicroscopy beamline (described in section 3.5.2) at Elettra, using photons with an energy of 74 eV.

3.5.2 SPEM on the Spectromicroscopy beamline at Elettra

The Spectromicroscopy beamline at the Elettra synchrotron runs a scanning photoemission microscope based on a Schwarzschild objective. Such a device consists of two spherical mirrors: one is the convex primary and the other in the concave secondary. High reflectivity of the Schwarzschild objective is obtained by using periodic multilayer coating. The use of multilayers, required for high reflectivity at a certain wavelength, restricts the photon energy range available after the monochromator (20-200 eV) to specific narrow

lines. Currently, the beamline is equipped with two Schwarzschild objectives designed for 27 and 74 eV of photon energy. The sample is placed at the focus of the Schwarzschild objective. It is mounted on a scanning stage which allows fine and coarse movement. The beam is focused into a submicrometric spot on the sample and electrons arising from the photoemission process are collected and analyzed with respect to their angular and energy distributions (ARPES study) by means of a internal movable electron energy analyzer in ultrahigh vacuum in the temperature range of 40-470 K (figure 3.20).

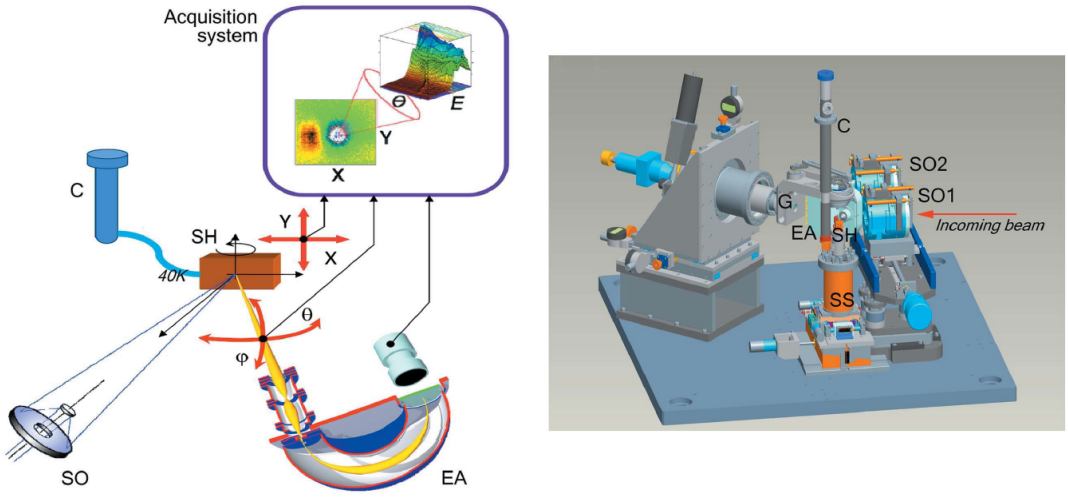

Figure 3.20: Instruments inside the experimental chamber of the Spectromicroscopy beamline at the Elettra synchrotron. The incoming beam is focused by one of the two Schwarzschild objectives on the sample which can be scanned across the beam to acquire the photoemission intensity maps. The main elements are: Schwarzschild objectives (SO1 and SO2), electron analyzer (EA), goniometer (G), sample holder (SH), scanning stage (SS), and cryostat (C). From [95].

The microscopic X-ray photoemission spectroscopy and angle-resolved photoemission spectroscopy (μ-XPS and μ-ARPES) experiments on the single crystals of Sb_2Te were performed on the Spectromicroscopy beamline, using photons with an energy of 74 eV. The incident photon beam was linearly *P*-polarized, and focused down to a submicrometric spot ($\sim$0.6 μm in diameter) on the sample surface using the Schwarzschild objective. The photoelectrons were detected with energy and angular resolutions of 50 meV and $\pm 0.3^\circ$, respectively, by means of the internal movable hemispherical electron energy analyzer mounted on a precision two axes goniometer setup [58, 95].

3.6 Conclusion

This chapter has given a general description of the different photoemission techniques and set-ups used in this thesis for the study of the electronic structure of our topological systems by means of light-matter interaction. I have revealed the processes that contribute to the carrier dynamics in solids. Besides, I have presented their relative timescales. After this brief overview on the essential specifications of this experimental techniques, I will present in the following chapters a photoemission study on the Bi_2Te_3 and the Sb_2Te topological materials.

Chapter 4

Bulk defects and surface state dynamics in Bi_2Te_3

In this chapter, I present a trARPES study of Bi_2Te_3 compounds under various irradiation conditions. Thanks to the combination of time, momentum and energy resolution, my results reveal the impact of the swift electron irradiation on the scattering and carrier relaxation dynamics in response to ultrafast optical excitation. In particular, I demonstrate that the induced disorder affects the ultrafast relaxation times of the out-of-equilibrium transient carrier population.

4.1 Bulk-insulating topological insulators

As already discussed in chapter 2, three-dimensional topological insulators (3D TIs) have attracted a lot of interest due to their unconventional and unique properties [1, 8, 27, 96, 97, 98]. While they are narrow-band semiconductors in the bulk, these materials possess gapless and topologically protected two-dimensional surface states (2D SSs), characterized by a Dirac-type linear energy-momentum electronic dispersion. Thanks to the combined action of spin-orbit coupling and of time-reversal symmetry, the relativistic fermions travelling in the spin-momentum locked SSs are insensitive to back-scattering in the presence of non-magnetic defects and impurities [36, 99, 100]. Distressingly, prototype narrow-gap TIs, such as Bi_2Te_3 and Bi_2Se_3 [15], commonly present lattice defects, i.e. antisites and vacancies, generated during crystal growth [101]. In undoped Bi_2Te_3, where antisites are prevalent, the conductivity is usually *p*-type, namely by hole carriers. In undoped Bi_2Se_3, where Se vacancies are presumed to dominate, the net conduction is by electron carriers or *n*-type. Consequently, the conduction through the surface channels is unavoidably intermixed with the detrimental bulk conductivity [102, 103]; this hinders the access to a genuine surface electronic transport indispensable for promising

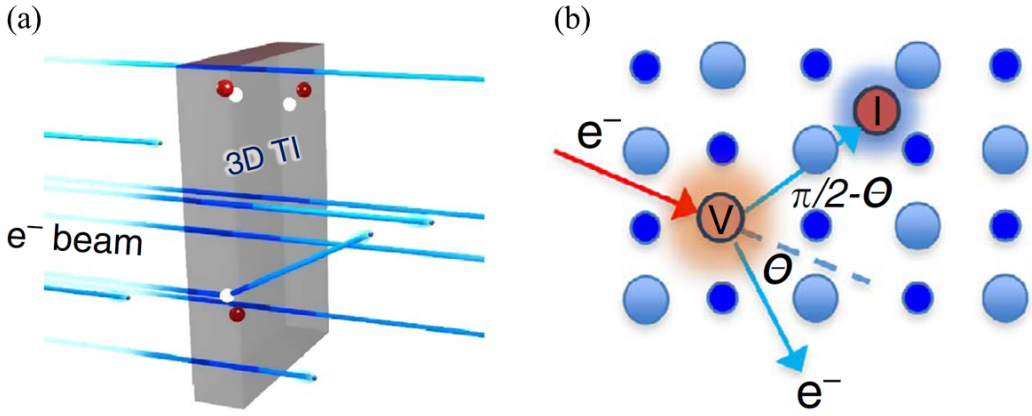

Figure 4.1: Tuning the bulk conductivity of 3D TIs by swift electron irradiation. (a) Energetic electron beams can penetrate solids to a depth of many tens of micrometers. Electron irradiation affects the bulk but not the robust topological SSs. (b) Impinging electrons induce the generation of Frenkel vacancy-interstitial pairs which act to compensate the intrinsic bulk defects. V: vacancy and I: intersititial. From [2].

technological applications, such as spintronics [104] or topological quantum computing [1].

Several attempts to decrease the significant bulk carrier contribution were based on chemical doping [17, 105], increasing the surface-to-bulk ratio using nanostructuring which can be performed through mechanical exfoliation or growth of TI nanowires and nanoribbons [106, 107], epitaxial growth of TI/II-VI semiconductor superlattices [108, 109], and irradiation by high-energy electron beams: in particular, intrinsic quantum transport measurements and ARPES revealed that a technique based on irradiation with swift ($\sim$ 2.5 MeV energy) electron beams at specific electron doses [2] does not affect the Dirac energy dispersion—immune to disorder—and offers a path to large scale transport in topological SSs (see figure 4.1(a)). Furthermore, this experimental study has indicated that it is possible, by following a thermal protocol, to tune the band position from the irradiation-induced *n*-type back towards the charge neutrality point (CNP) where the system remains for months. At the microscopic level, this is related to the creation of vacancy-interstitial pairs (Frenkel defects) in the bulk material (figure 4.1(b)). The combined effect of these pairs is to compensate the intrinsic charged defects responsible for the conductivity of the bulk without affecting the lattice parameters, i.e. the crystal lattice integrity is maintained.

In the following paragraphs, I will present the results, acquired by the study conducted by Zhao *et al.* [2], which reveal that stable surface conduction channels are achieved when a sufficient irradiation dose is followed by an optimally engineered annealing procedure,

thereby resolving one of the key limitations of bulk TIs.

4.1.1 Low irradiation dose

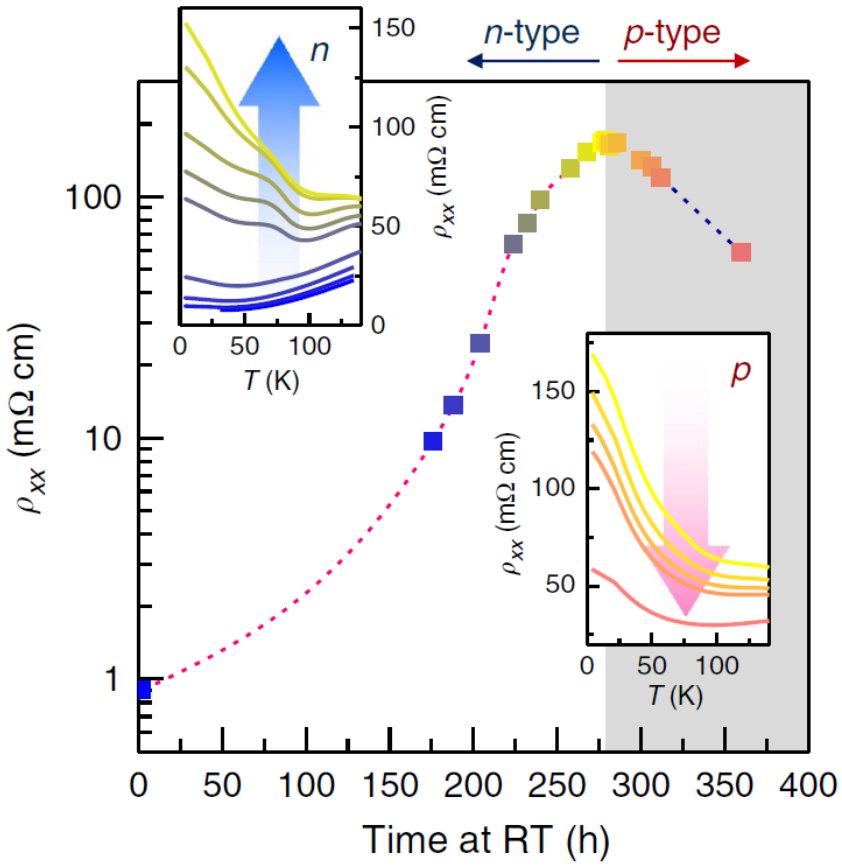

Figure 4.2: Evolution of the longitudinal resistivity ρ_{xx}, measured at 4.2 K after cycling to RT for a sample irradiated with an electron dose of 90 mC/cm^2, from the *n*-type region back to the *p*-type region. The maximum of ρ_{xx} marks the crossing of the CNP which can be attained by designing an appropriate thermal protocol. Each RT dwell time is represented with a distinct color. Insets display ρ_{xx}(T) for the *n*-type region (upper left) and the *p*-type region (lower right). From [2].

The stability of the net carrier density is imperatively determined by the terminal irradiation dose. For low terminal electron doses ($\phi \lesssim 0.1$ C/cm^2), the resistivity is not stable: it evolves from the *n*-region just after irradiation through the CNP back into the *p*-region. This was obtained by simply changing the dwelling time at room temperature (RT) to allow the migration of vacancies. As represented in figure 4.2, we observe a reverse conversion from a metallic-like resistivity on the *n*-side just after irradiation through an insulating resistivity at the CNP (after nearly 250 h at RT) and back to a

weakly semiconducting-like resistivity on the *p*-side. This is compatible with a slow diffusion (hundreds of hours at RT) of vacancies and is in accord with the estimated energy barriers ∼0.8 eV typical for vacancy migration in solids. Thus, at low terminal electron doses, the defect migration is sluggish and the equilibrium is not reached, i.e. the low irradiation does not guarantee a stable high resistance state.

4.1.2 High irradiation dose

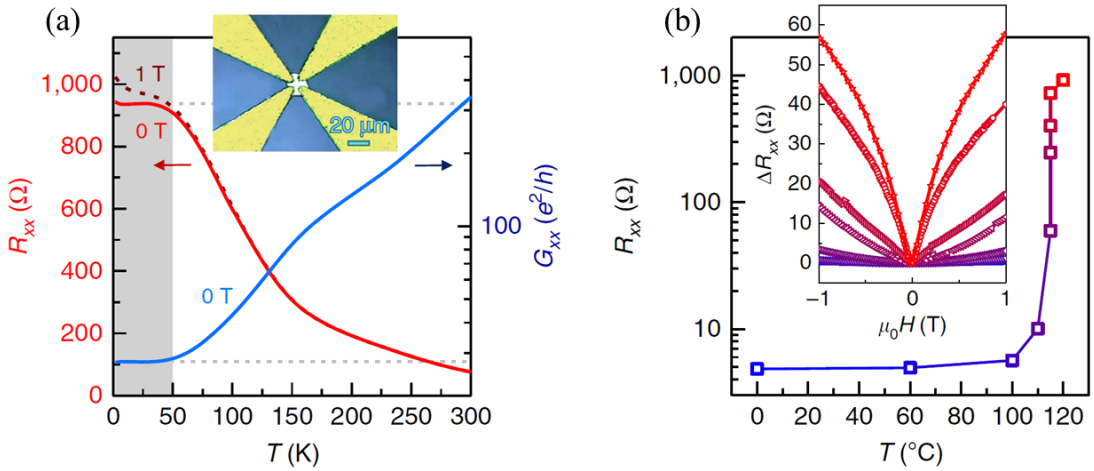

Figure 4.3: Stable CNP and 2D conductance in an irradiated Bi_2Te_3. (a) Sheet resistance R_{xx} as a function of temperature of a Bi_2Te_3 single crystal at the CNP (red line) revealing a plateau at low temperatures. Inset: optical image of the sample showing a van der Pauw contact configuration. (b) Annealing procedure with time steps of Δt = 30 min used to tune the Bi_2Te_3 crystal, irradiated with a dose of 1 C/cm^2, back to the stable CNP. Inset: magnetoresistance at 1.9 K after each annealing step with matched colors to indicate different annealing temperatures. From [2].

When the terminal electron dose is 10 times higher (ϕ = 1 C/cm^2), the stability can be controlled and enhanced in a reverse conversion mechanism by an annealing procedure. Figure 4.3(a) represents the temperature dependence of the sheet resistance R_{xx} and the conductance G_{xx} of Bi_2Te_3 tuned back to the CNP via an annealing process (figure 4.3(b)) where it remained for months of testing.

To confirm the results of the transport measurements, an ARPES study was conducted. Figure 4.4(a) illustrates an ARPES image taken along the $\overline{\Gamma M}$ high symmetry direction, before the annealing process of a Bi_2Te_3 crystal irradiated with an electron dose of 1.7 C/cm^2, revealing the electronic robustness of the topological SSs against the electron irradiation. As clearly represented in figure 4.4(b), under an annealing protocol, the Dirac dispersion is preserved. The effect of tuning the conduction from the irradiation-induced

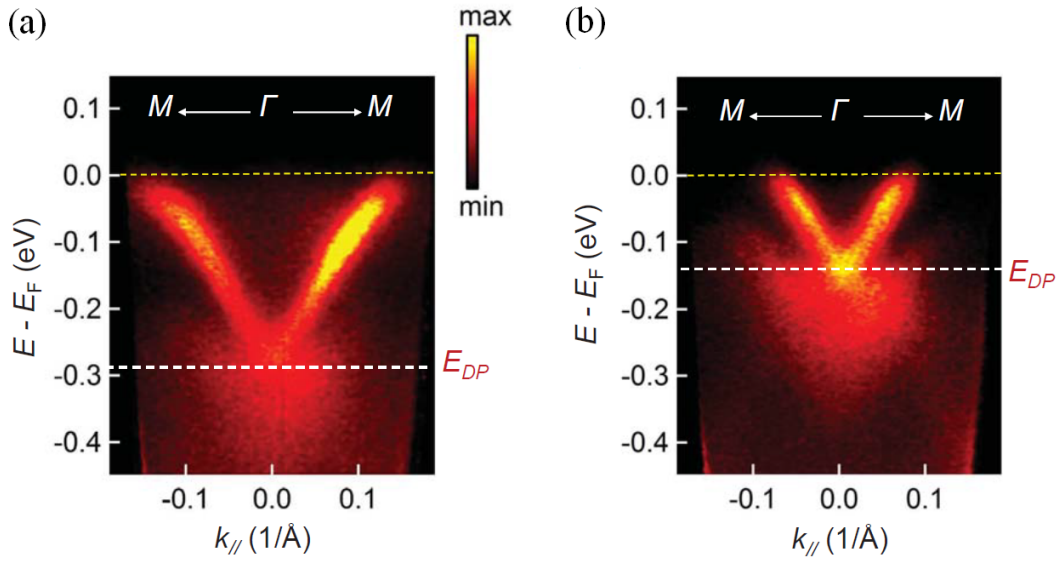

Figure 4.4: ARPES intensity maps taken at 130 K of a Bi_2Te_3 crystal, irradiated with an electron dose of 1.7 C/cm^2, along the $\overline{\Gamma M}$ direction in the Brillouin zone. (a) Before annealing, the DP is located at $E_{DP} \sim$ -290(10) meV with respect to E_F. (b) After 30 min of annealing at 120 °C, the DP upshifts to a binding energy of $E_{DP} \sim$ -160(10) meV. ARPES data demonstrate that the thermal protocol tunes the system back to the CNP and preserves the topological SSs. From [2].

n-type (figure 4.4(a)) back towards the CNP (figure 4.4(b)) by an annealing protocol is a relative shift of the surface chemical potential (E_F) toward the Dirac point (DP), chosen as a reference point, consistent with the transport data. Therefore, the combination of irradiation and thermal protocol (presented in figure 4.3(b)) leads to a conduction dominated by surface channels and brings E_F back into the bulk gap towards the CNP where the compound remains for months. It should be pointed out that if E_F is placed within the bulk bandgap, all conduction will ideally take place on the SSs, enabling the creation of devices which exploit the unusual properties of these surfaces. Thus, irradiation by energetic electron beams of Bi_2Te_3 constitutes an efficient method to suppress the bulk conduction.

Consequently, these results call for more extensive investigations to unveil if and how the irradiation procedure affects the properties of the surface Dirac fermions. In the following, I present trARPES measurements that I performed on Bi_2Te_3 crystals under several irradiation conditions.

4.2 Technique and experimental details

I investigated high-quality Bi_2Te_3 single crystals grown with a modified Bridgman method. Two of these crystals, namely BT1 and BT2, have been irradiated with a swift electron dose of 1 C/cm^2 and 1.7 C/cm^2, respectively. All studied crystals come from the same boule. Carrier density was calculated from *ex situ* transport and Shubnikov–de Haas oscillations measurements, and was evaluated to be 4×10^{18} cm^{-3} for the *p*-doped non-irradiated sample, designated as BT0. Directly after an irradiation dose of 1 C/cm^2 and 1.7 C/cm^2, the conduction becomes *n*-type and the carrier concentration is 1.7×10^{19} cm^{-3} and 1.97×10^{19} cm^{-3}, at 105 K, respectively.

All samples were precisely oriented along the $\overline{\Gamma M}$ high symmetry direction and cleaved *in situ* with a top-post at RT under ultrahigh vacuum conditions (base pressure better than 2.5×10^{-10} mbar). After cooling down the samples, all trARPES measurements were carried out at a base temperature of 130 K using the FemtoARPES setup. The out-of-equilibrium spectra were recorded using linear *S*-polarized 6.32 eV photons and were collected under an infrared pump fluence of 0.15 mJ/cm^2.

4.3 Spectral effects of the induced bulk defects

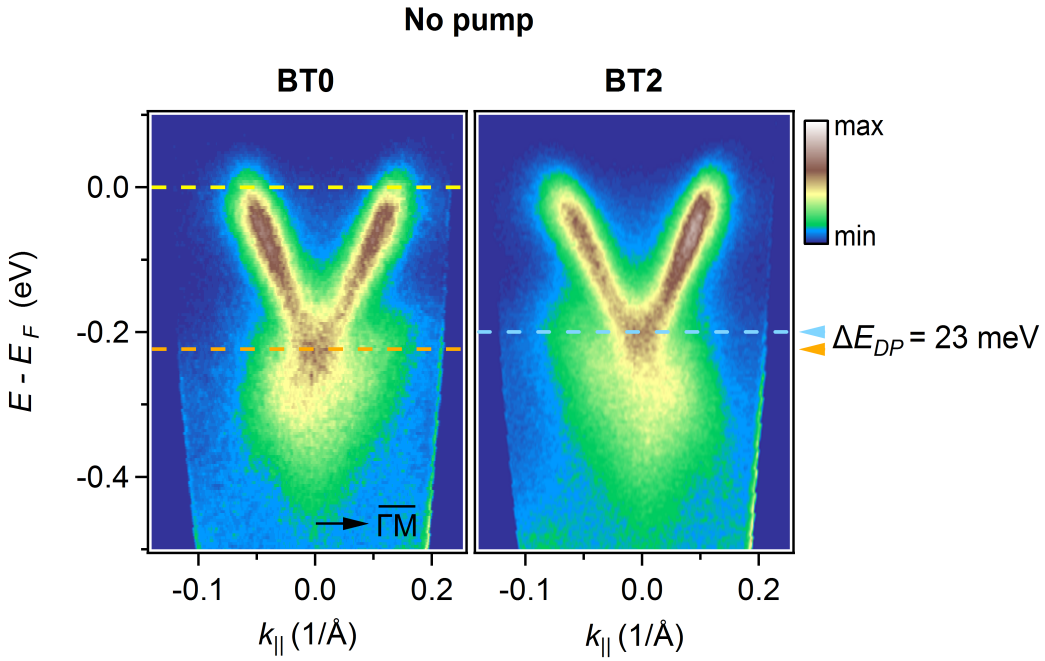

Figure 4.5: Comparison of the photoelectrons intensity maps along the $\overline{\Gamma M}$ direction for the non-irradiated BT0 and the irradiated BT2 crystals. The detected DP positions differ from a binding energy of 23 meV between the two ARPES images.

In figure. 4.5, I compare conventional ARPES yields of a non-irradiated and an irradiated sample. It should be noted that the BT2 sample, after irradiation with 1.7 C/cm^2 of terminal electron dose, was kept at RT for more than one month. The aim of this was to allow vacancies to diffuse in order to determine whether the irradiated compound would regain its initial properties. At first sight, we clearly remark that the binding energies of the DPs with respect to E_F, indicated by a yellow dashed line, are different for the two samples. Quantitatively, the DPs, delimited by orange and blue dashed lines, present a shift of 23 meV between the BT0 and the BT2 specimens. The presented spectra are relative to cleaved surfaces with significant pinning, which makes it possible to have the DPs at equivalent binding energies for the various samples [110]. The positions were found by fitting the energy distribution curves near $\bar{\Gamma}$ with a Gaussian function. This reflects that the irradiated sample does not retrieve its original state of equilibrium after defect migration despite the preservation of the electronic Dirac cone spectrum against irradiation.

4.4 Dynamical effects of the induced bulk defects

To better understand the consequences of the electron beam irradiation on the sample response to ultrafast light pulses, I have performed a series of trARPES measurements. As noticed in chapter 3, in the trARPES technique, pump photons excite hot electrons into the empty states, giving access to the band structure and the ultrafast time evolution of the transient electron population. As a representative example, I present in figure 4.6, images obtained for selected time delays on the freshly irradiated BT1 sample, i.e. the trARPES study was conducted immediately after the swift electron irradiation. Similar results were obtained also for the other samples, whose time evolution is presented in figure 4.7.

Before the arrival of the infrared pump beam, at negative delays—equivalent to a time scale of 4 μs, i.e. to a complete relaxation of the system—we probe the electronic structure in its ground state: by comparing the photoemission signal at negative delays with the one obtained with no pump (see the upper-left corner of figure 4.6), I verified that residual out-of-equilibrium effects such as surface photovoltage [111] were negligibly small. Thus, the photoelectron intensity spectrum taken at -0.40 ps time delay (figure 4.6) shows electronic band structure at equilibrium, right before any excitation effect. Following the pump photoexcitation at Δt = 0 ps, a transient excited electron population is observed at energies $\sim$0.6–0.8 eV above E_F. Note that the SSs and the lower-lying conduction band (CB) are not directly populated (as it was already discussed by [39]). These highly excited electronic states dissipate rapidly, triggering a cascade of intraband and interband transitions through recombination procedures acting as a source of electrons for the low-lying CB and SSs.

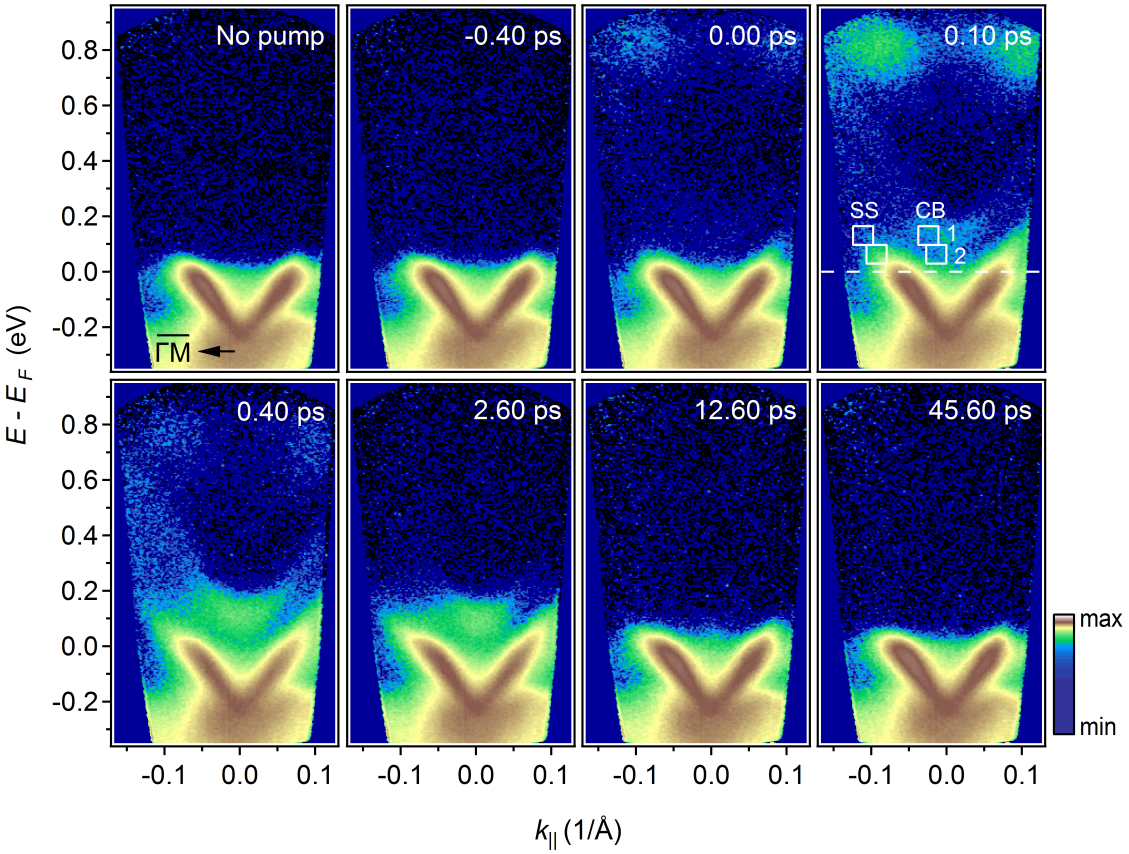

Figure 4.6: trARPES sequence near the $\bar{\Gamma}$ point for various pump-probe delays for the freshly irradiated specimen. White dashed line indicates the E_F. The color intensity is displayed in logarithmic scale to make the signal from the unoccupied electronic band structure more discernible.

In order to obtain a quantitative picture on the characteristic relaxation times of the involved transient electronic population, I integrated over different *k*-*E* integration windows delineated as 1 and 2 in figure 4.6. As discussed in previous works [45, 112], the dynamics depend on the precise choice of the energy-momentum window: for the sake of comparison, the SS_2 and CB_2 boxes were taken at 28 meV above E_F for all the Bi_2Te_3 samples and figure 4.7 depicts the respective transient electronic populations.

4.4.1 Ultrafast relaxation regime

Quantitatively, the relaxation times of SS_1 and CB_1 are summarized in table 4.1. The characteristic lifetimes of the excess electron population for the 1–2 *k*-*E* SS and CB regions were extracted by fitting the data with a single or a double decay exponential function. The fits, shown as black dashed lines, together with the residues are represented in figures 4.8–4.15 for all specimens. Note that the residue is the difference between the

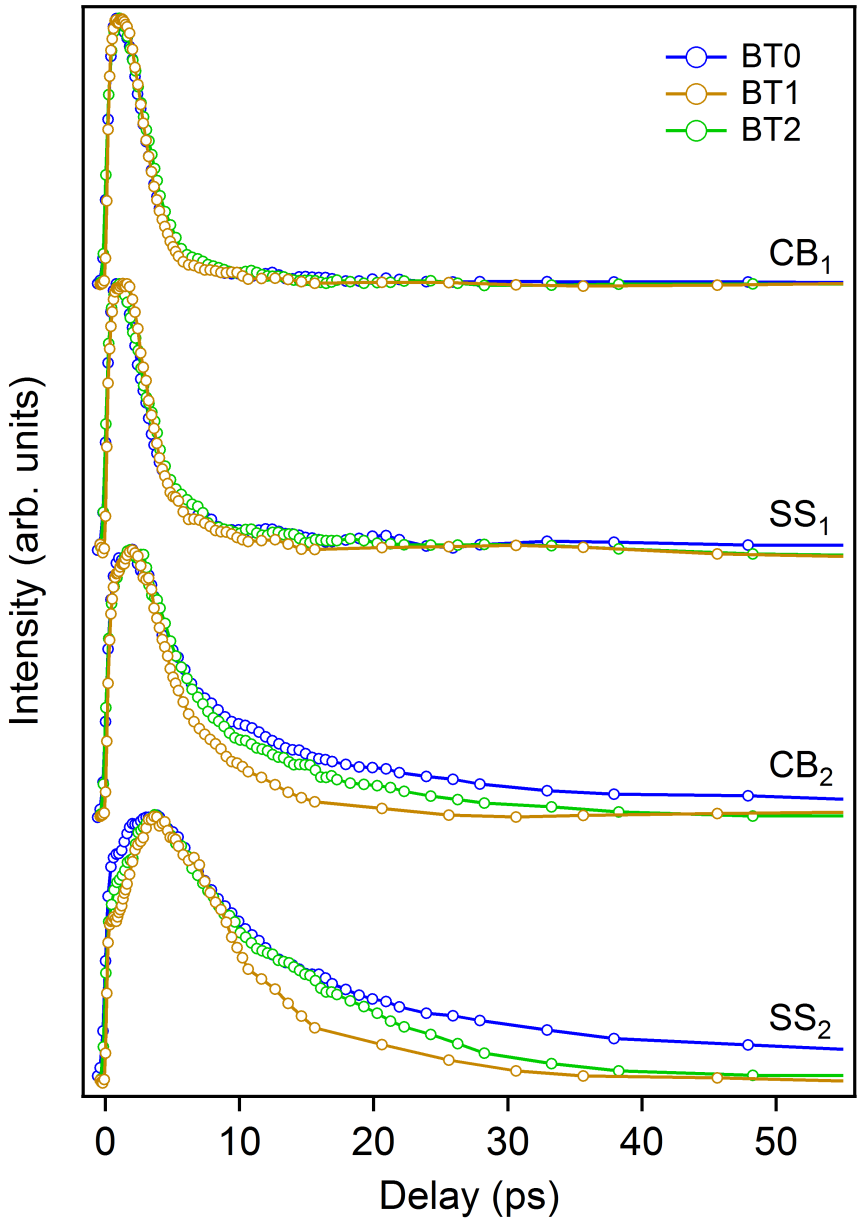

Figure 4.7: Transient photoemission intensity within the integration windows 1 and 2, presented at Δt = 10 ps time delay in figure 4.4, for the three sibling Bi_2Te_3 samples.

transient photoemission intensity and the fitting function. For each sample, the SS_1 and the CB_1 possess similar scattering times indicating that SS_1 and CB_1 present a parallel evolution and an effective carrier exchange takes place between the two bands (interband scattering). Evidently, for the ultrafast dynamics (during the first few picoseconds), these characteristic times τ_1 are mostly due to the electron-phonon coupling for both surface and bulk bands. Besides, we notice that the irradiation process does not affect the order of magnitude of the electron decay times of SS_1 and CB_1: the values are in the same range

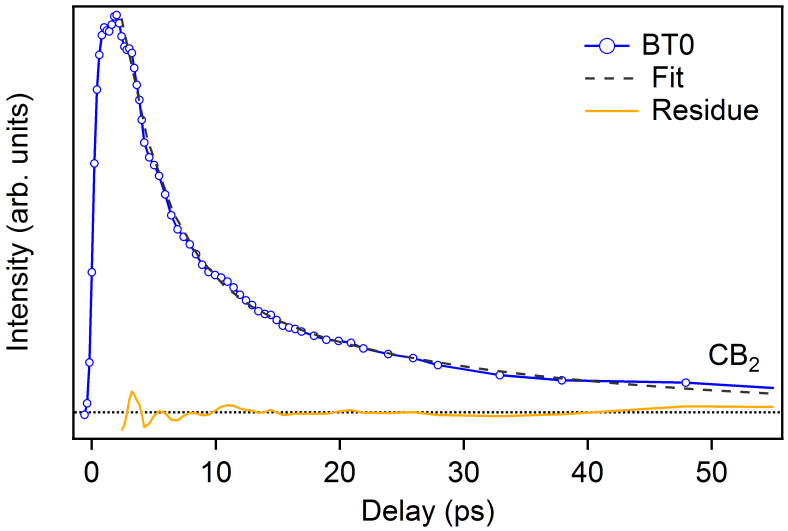

Figure 4.8: Ultrafast time evolution of the transient electronic population in the *k*-*E* CB_2 window for BT0.

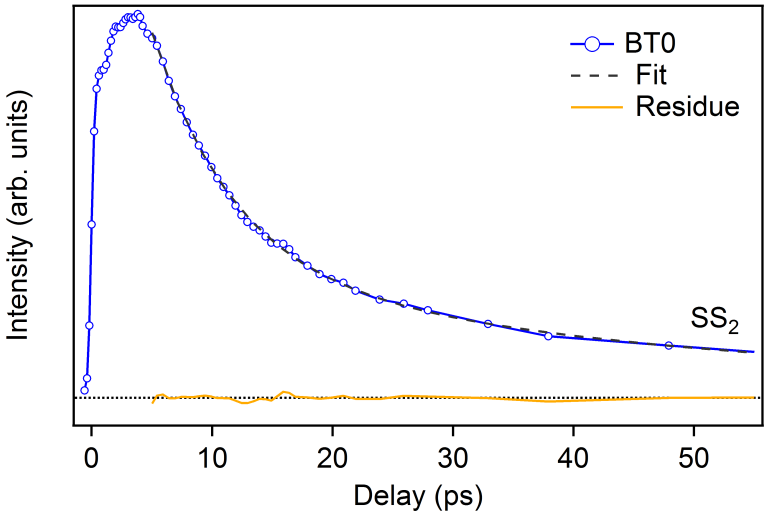

Figure 4.9: Ultrafast time evolution of the transient electronic population in the *k*-*E* SS_2 window for BT0.

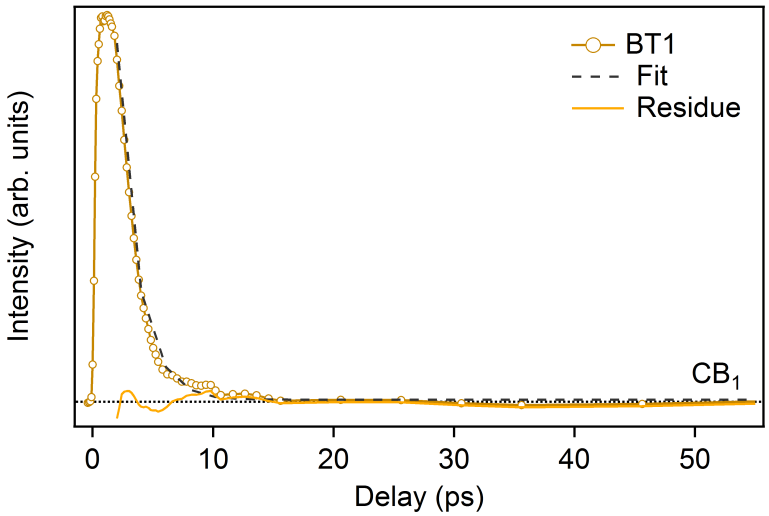

Figure 4.10: Ultrafast time evolution of the transient electronic population in the *k*-*E* CB_1 window for BT1.

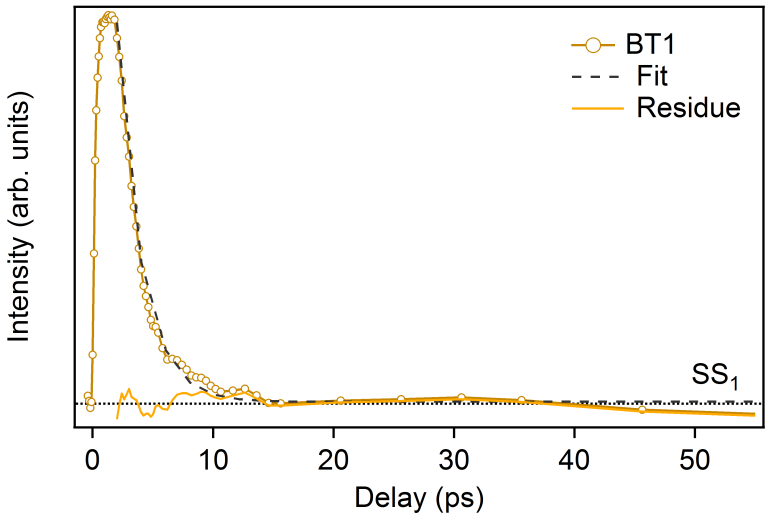

Figure 4.11: Ultrafast time evolution of the transient electronic population in the *k*-*E* SS_1 window for BT1.

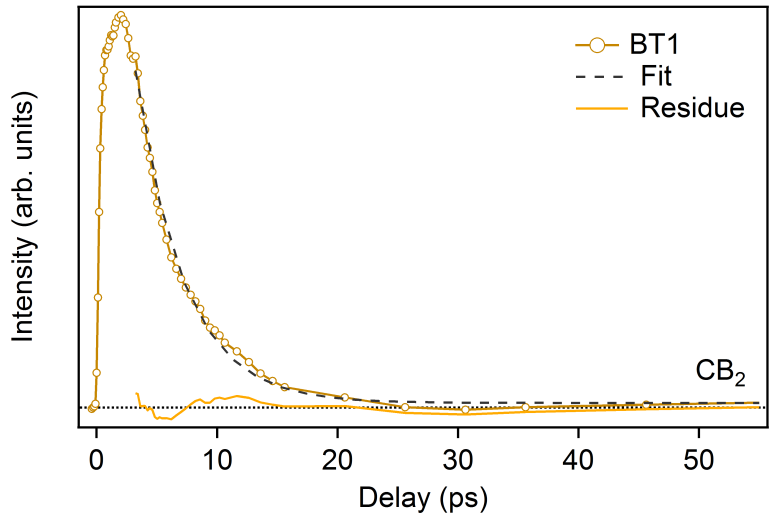

Figure 4.12: Ultrafast time evolution of the transient electronic population in the *k*-*E* CB_2 window for BT1.

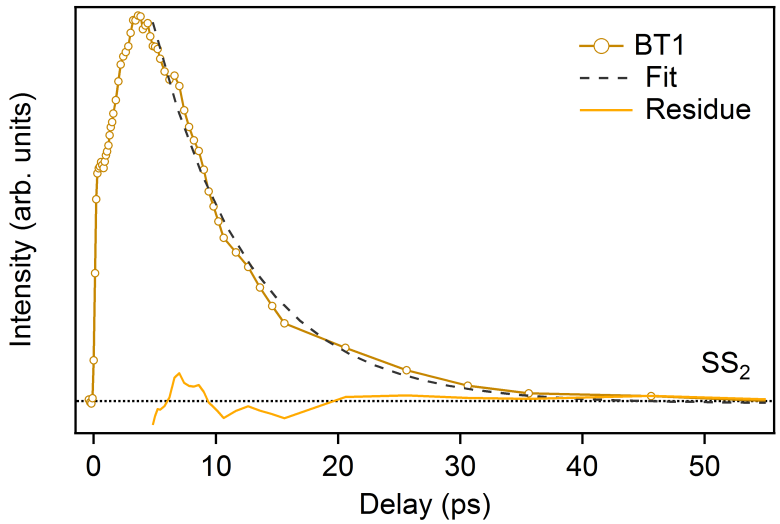

Figure 4.13: Ultrafast time evolution of the transient electronic population in the *k*-*E* SS_2 window for BT1.

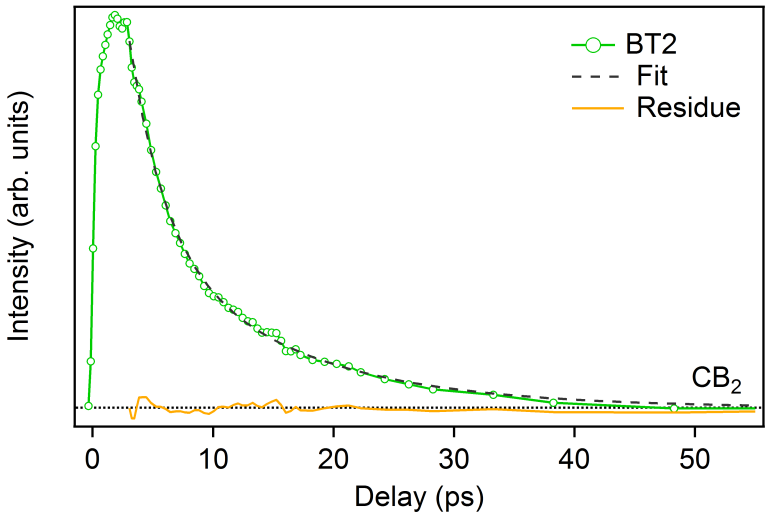

Figure 4.14: Ultrafast time evolution of the transient electronic population in the *k*-*E* CB_2 window for BT2.

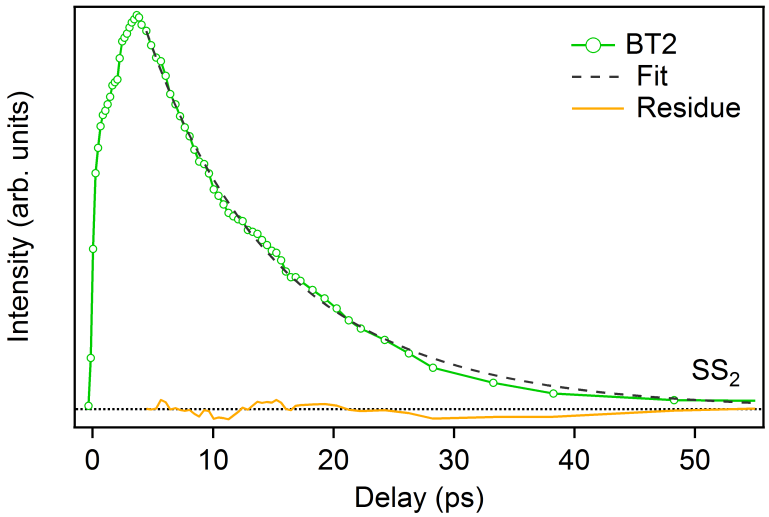

Figure 4.15: Ultrafast time evolution of the transient electronic population in the *k*-*E* SS_2 window for BT2.

and almost similar, i.e. around 2 ps for SS_1 and for CB_1 for the three crystals.

Next, I compare the temporal evolution of the excess electronic population in two isoenergy regions at 28 meV above E_F marked as SS_2 and CB_2 (table 4.1), which present a qualitatively similar behavior between them for all samples. This indicates a very strong and effective interband scattering between SS_2 and CB_2. In particular, for the ultrafast temporal decay dynamics, the relaxation lifetimes τ_1 for CB_2 for the three specimens are more or less identical ($\sim$3 ps). A parallel behavior for τ_1 can be also observed for SS_2, with a different numerical value ($\sim$7 ps).

Table 4.1: Characteristic decay times of SS_1, CB_1, SS_2 and CB_2 of the series of Bi_2Te_3 specimens. For each BT sample, the τ_1 (the ultrafast regime) and τ_2 (the long lasting regime) correspond to the values of the lifetimes of the first and the second raw, respectively.

Sample	τ_{SS_1} (ps)	τ_{CB_1} (ps)	τ_{SS_2} (ps)	τ_{CB_2} (ps)
BT0	2.58 ± 0.1	1.91 ± 0.1	6.78 ± 0.2 45.16 ± 3.7	3.66 ± 0.3 22.85 ± 3.5
BT1	2.03 ± 0.1	1.7 ± 0.1	7.88 ± 0.3	3.98 ± 0.1
BT2	2.65 ± 0.1	2.21 ± 0.1	6.5 ± 7.3 12.97 ± 3.3	2.86 ± 0.3 12.03 ± 1

4.4.2 Long lasting relaxation regime

For the prolonged temporal delays, the long decay rates τ_2 for CB_2 significantly differ from one sample to another: particularly, moving from BT0 to BT1, we can notably detect that τ_2 decreases for BT2 (12.03 ps) and completely vanishes for BT1. A parallel behavior for τ_2 can be also detected for SS_2, with distinct numerical quantities (45.16 ps and 12.97 ps).

Note that the long lifetimes τ_2 of SS_2 and CB_2 for BT0 and BT2 reflect the presence of an additional filling channel, probably a diffusion channel [43]. Whereas for BT1, the long lasting decay time τ_2 is suppressed for SS_2 and CB_2 by creating additional recombination channels by means of defects induced by the irradiation procedure. Moreover, the long lasting excited SS_2 population for BT0 persists for more than 10 ps; as already found in other similar prototypical materials like Bi_2Se_3 [113], $Bi_2Te_2Se_2$ [114], and even for the *n*-type Bi_2Te_3 [39]. This proves that the long-lived SS population is a general property of the Bi_2Te_3 compound regardless its chemical doping level (*n*-type or *p*-type), and may be a universal feature of TIs.

Effectively, from the temporal decay behaviors (table 4.1), we can conclude that there are two regimes: the "ultrafast regime" τ_1 where BT1 and BT2 behave like BT0, and the "long lasting regime" τ_2 which is very sensitive to the irradiation conditions of the specimen.

4.4.3 Visualization of the two relaxation regimes

Further insight into these two regimes can be obtained from the differences of the trARPES images with respect to negative delays, presented in figure 4.16. Blue and red areas correspond to a depleted and excess electronic populations, respectively, upon photoexcitation. At 5.5 ps, corresponding to the ultrafast regime, the three specimens show undifferentiated excess electronic population in the Dirac cone. For longer delays, precisely at 12 ps, we observe that the concentration of the Dirac fermions in BT0 and BT2 samples is higher than the one of the BT1 specimen. Moving to the extremely extended delays of the overlong regime, BT0 displays a persistent hot electron density in the Dirac SSs and a transient charge asymmetry—attributed to a spatial separation between excess electrons and holes. Irradiated samples, on the other hand, are relaxed back to equilibrium.

4.5 Tuning the topological surface state dynamics

The ultrafast relaxation of Dirac fermions in the SSs of Bi_2Te_3 is very sensitive to the irradiation conditions of the bulk of the specimen. While the very long τ_2 of SS_2 is a property that has already been observed and can be explained by the fact that in the non-irradiated BT0 sample there are less defects, the different τ_2 for the irradiated BT1 and BT2 samples means that this parameters depends on the nature of the defects created by irradiation. Even though not all the aspects related to the long-term evolution of irradiation induced defects are clear, it was suggested that the vacancy interstitial (Frenkel) pairs produced in the BT1 samples slowly evolve with time towards a majority of di-vacancies. It is consequently natural to associate the fastest relaxation time to the action of the former, while the latter makes it possible to maintain an intermediate regime for the SS_2 dynamics. Conversely, this also indicates that, by modifying the irradiation parameters (projectile dose, quantity of Frenkel pair-production, dwelling time at RT, etc.), we can control the decay dynamics of the topological SSs.

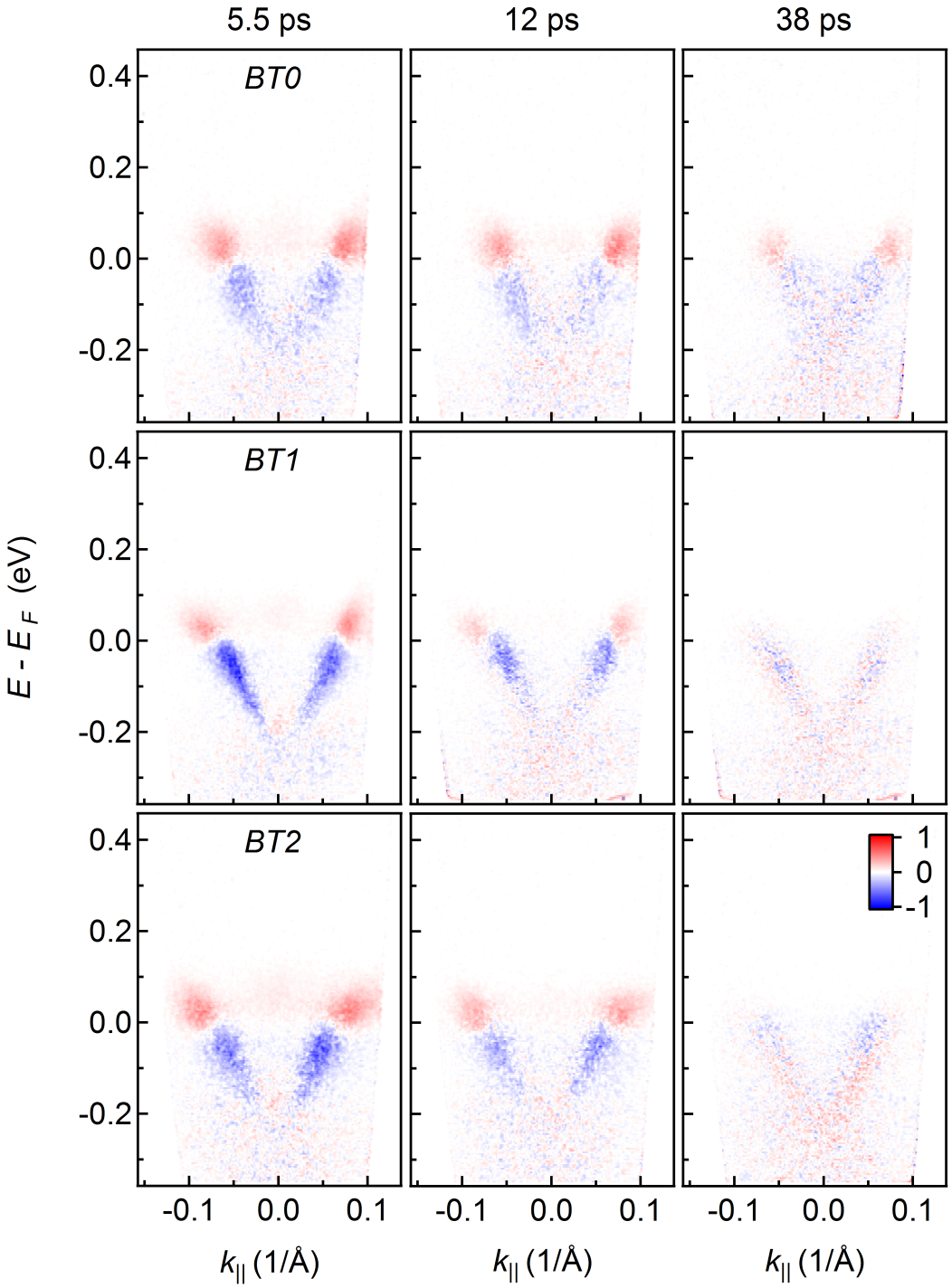

Figure 4.16: Comparison of the ultrafast trARPES images, at three selected pump-probe time delays, for the non-irradiated and the irradiated Bi_2Te_3 series. Excess electrons (red) and holes (blue) are obtained from the difference of trARPES images taken after and before excitation.

4.6 Conclusion

In summary, by means of an experimental trARPES study, I have investigated in detail the time-dependent electronic distribution after photoexcitation of a series of Bi_2Te_3 samples in different conditions of electronic irradiation. My results confirm that the topological nature of the SSs is robust against the exposure to high-energy particles. Two dominating relaxation regimes govern the temporal evolution of the electron population of the series: the faster one is common for the three samples, i.e. unaffected by defect generation, and is mainly determined by the characteristic time of the electron-phonon interaction; the slower one is related to the thermalization of the excess charge via diffusion and can be suppressed by adding disorder to the lattice. I conclude that we can modulate the electronic dynamics, in particular those of the topological SSs, by modifying the irradiation parameters. As all these parameters can be adjusted in a controlled way, they can potentially be used as a powerful tool in future devices based on photoconductive control of topological SSs with ultrafast light pulses.

Chapter 5

Electronic band structure for occupied and unoccupied states of Sb_2Te

In this chapter, I investigate the occupied and unoccupied electronic band structure of the natural topological superlattice phase Sb_2Te by making use of SPEM, XPS and trARPES. After cleaving several Sb_2Te single crystals, I have found various non-equivalent regions on the same surface, identifying three distinct terminations characterized by different Sb/Te surface stoichiometric ratios and with clear differences in their band structure. For the dominating Te-rich termination, I have studied the transient electronic structure for the topological surface states (SSs) and bulk bands. My results evidently reveal that the surface electronic structure is connected to the bulk properties of the superlattice [109].

5.1 Natural topological superlattices

As evoked in previous chapters, many features make topological insulators (TIs) fascinating and promising candidates for a new generation of electronic and spintronic devices [116]. Therefore, these materials are triggering novel efforts to be able to tune and engineer their topological SS band structure.

In this context, various theoretical studies have anticipated that multilayer structures, composed of an ordered stacking sequences of TIs interleaved with other compounds, sandwiched in a superlattice, present new topological properties [117, 118]. More recently, a theoretical and experimental study has indicated that the natural superlattice series $(Sb_2)_m$-Sb_2Te_3 (m = 0–3), made of an ordered stacking of integer numbers of Sb_2 bilayers (BLs) and Sb_2Te_3 quintuple layers (QLs), possesses tunable topological SSs for the whole range m = 0–3, with the surface termination playing a key role [3]. Figures 5.1(a)–5.1(d), taken from Johannsen *et al.* [3], display the evolution of the electronic band structure, particularly, the one of the topological SSs, obtained by first-principle calculations

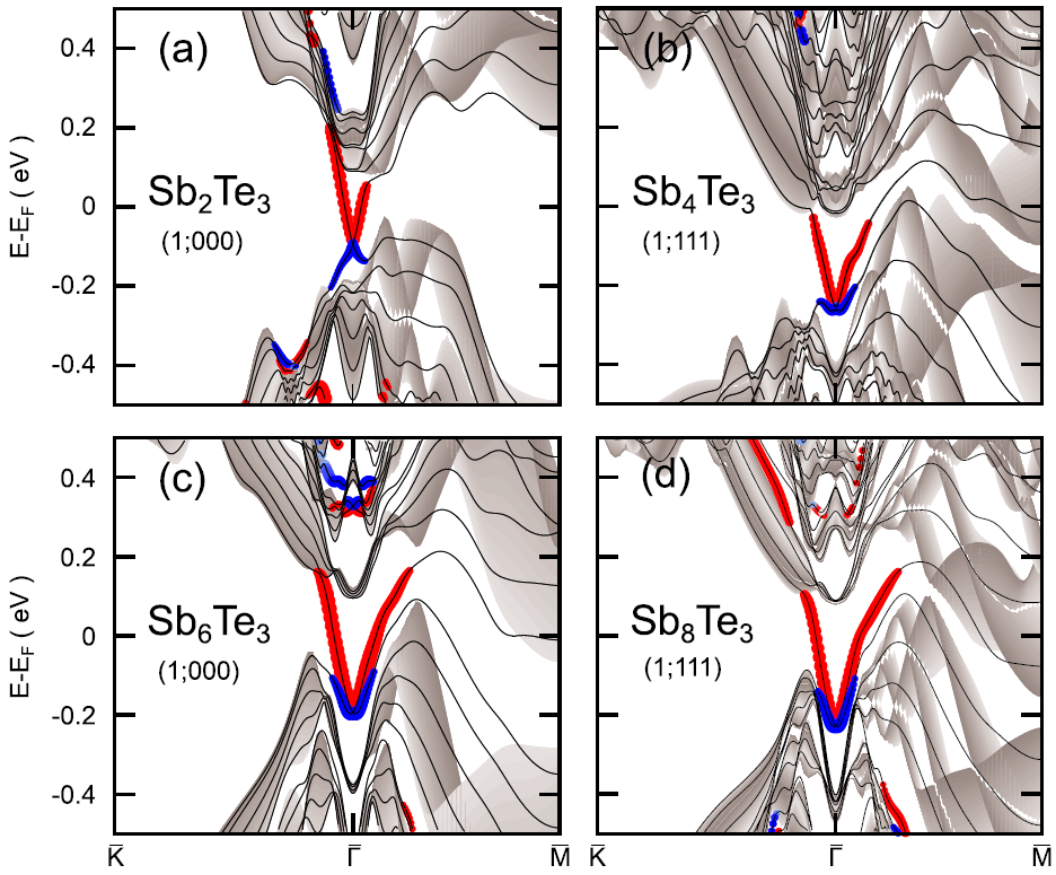

Figure 5.1: Semiconductor-to-semimetal transition in the natural superlattice series $(Sb_2)_m$-Sb_2Te_3 (m = 0–3). (a)–(d) First theoretical calculations of the electronic band structure for slab models (lines) of $(Sb_2)_m$-Sb_2Te_3 (m = 0–3) superimposed with the projected bulk states (gray shading). All energies are referred to the Fermi level (E_F) of the bulk band structure. From [3].

for the m = 0–3 elements of the $(Sb_2)_m$-Sb_2Te_3 series. Furthermore, this study has revealed that the band ordering, which varies through the series, results in a transition from a semiconducting phase of Sb_2Te_3 (m = 0) to a semimetal phase with a negative indirect band gap for Sb_8Te_3 (m = 3). This transition already takes place at m = 1 and is conducted by an elevation of the valence band (VB) maximum along the $\overline{\Gamma M}$ high symmetry direction that eventually overlaps in energy with the conduction band (CB) minimum. Thus, as m increases, the band dispersion of the lower branch of the topological SSs evolves from Dirac-like in Sb_2Te_3 to Rashba-like with a strong upper and lower branch asymmetry in the Sb-rich systems. This is due to the fact that the topological nature of the SSs requires that the lower and upper branches of the topological SS band connect to the VB and the CB, respectively. This results demonstrates that a control over the topological SS dispersion can be achieved in this natural topological superlattice series.

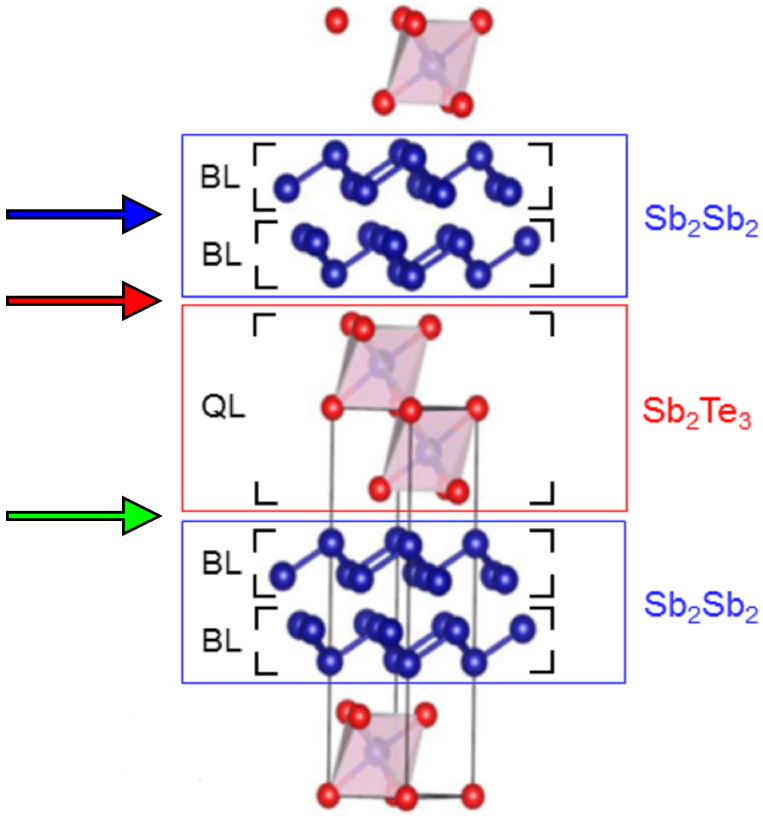

Figure 5.2: Crystal structure of Sb_2Te showing both Sb_2Te_3 QL and Sb_2 BLs building blocks [115], horizontal arrows indicate the different cleaving planes.

In this thesis, I focus my attention on the most representative material in the topological superlattice series $(Sb_2)_m$-Sb_2Te_3, namely diantimony-tellurium Sb_2Te (m = 2). This particular compound is made of two Sb_2 BLs interleaved with five-layer stacks of Sb_2Te_3 [115, 119] (see figure 5.2). Note that the electronic structure of Sb_2Te_3, a member of the series (m = 0), has already been investigated both experimentally and theoretically [3, 15, 18, 99, 120]. After cleaving a Sb_2Te single crystal, three different surfaces can be obtained (see figure 5.2), specifically: a "Sb-rich 1BL" termination obtained after breaking the van der Waals bonds between the two Sb_2 BLs, a "Sb-rich 2BLs" termination envisaged upon breaking the van der Waals bonds to a neighboring Sb_2Te_3 QL, and a "Te-rich QL" termination resulting from breaking the interaction between the building blocks [3]. Previous results suggest that these three distinct surface terminations are actually simultaneously present on real cleaved surfaces of Sb_2Te, but a clear evidence of their coexistence and a precise description of their properties has not been provided yet. The relevance of this issue for the overall properties of the system calls for more

detailed experimental studies of the interplay between surface terminations of Sb_2Te and its electronic properties.

In the following, I characterize the three surface terminations of Sb_2Te via μ-XPS, μ-ARPES and XPS, providing also a direct visualisation of the ultrafast transient carrier population after photoexcitation using trARPES. The combination of these experimental techniques gives access to thus far missing information on both the occupied and unoccupied electronic band structure of Sb_2Te.

5.2 Technique and experimental details

High-quality single crystals of Sb_2Te [121] were cleaved *in situ* with a top-post under UHV conditions (base pressure better than 2.5×10^{-10} mbar), and were measured with μ-XPS, μ-ARPES, XPS and trARPES.

As already mentionned in chapter 3, the μ-XPS and μ-ARPES experiments were performed on the Spectromicroscopy beamline, using photons with an energy of 74 eV, while the XPS measurements were conducted on the APE beamline at the Elettra synchrotron light source. The incident photon beam was linearly *P*-polarized.

The trARPES measurements were performed using the FemtoARPES experimental setup with an energy resolution of 60 meV and a temporal resolution of 80 fs. The out-of-equilibrium spectra were recorded using linear *S*-polarized 6.32 eV photons and were collected under incident pump fluence of 0.28 mJ/cm^2.

The μ-XPS, μ-ARPES and trARPES measurements were carried out at a base temperature of 110 K, while the XPS data were acquired at 77 K.

5.3 Occupied electronic band structure

The SPEM measurements were performed combining the two operating modes of the instrument: (i) imaging, where the specimen surface is mapped detecting photoelectrons in a selected kinetic energy window, and (ii) μ-XPS and μ-ARPES. All images were background subtracted and normalized to correct for topographic effects [122].

5.3.1 Imaging study

In figures 5.3(a) and 5.3(c), I present two typical SPEM images, obtained on two different cleaved surfaces by detecting photoelectrons in the XY-WZ window, corresponding to the Sb *4d* core levels. In order to investigate in more detail their properties, I selected two specific regions: S_1 (figure 5.3(a)) and S_2 (figure 5.3(c)), delimited by dashed contours.

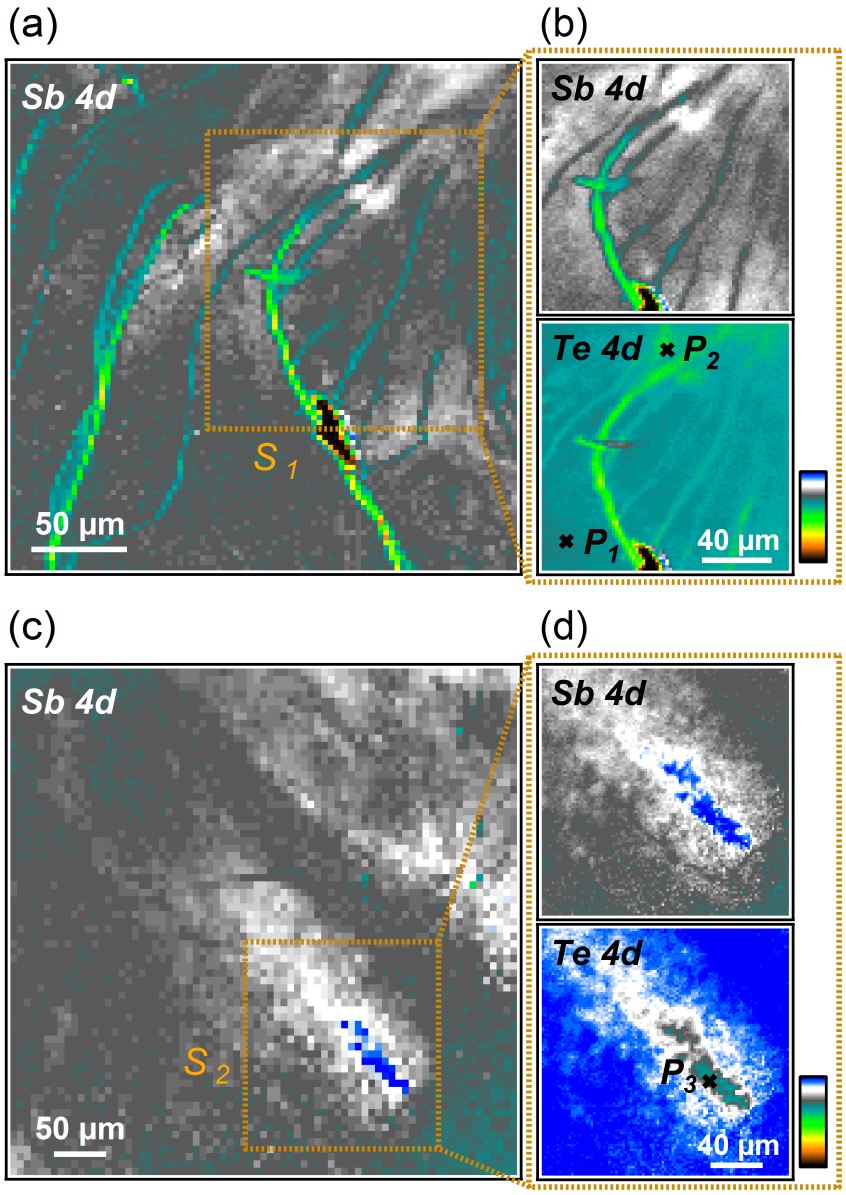

Figure 5.3: SPEM images taken at a photon energy of 74 eV. (a) SPEM image, recorded at photoelectron kinetic energy corresponding to Sb *4d* core level for the first cleave, revealing two terminations marked in white and grey intensity color scale; the S_1 box includes both terminations. (b) Upper and lower panel present higher resolution images of the S_1 regions, obtained at two distinct photoelectron kinetic energies corresponding to the Sb *4d* and Te *4d* core levels, respectively. The two images present reversed chemical contrast. (c) Sb *4d* SPEM image for another cleaved surface, clearly revealing a third kind of termination (appearing as blue in the image), contained in the S_2 contour defining the third terminated surface. (d) Same as (b) but for S_2 region.

In figure 5.3(b), I present a comparison of the images obtained from the S_1 region by measuring photoelectrons from the Sb *4d* core level (upper panel) and from the Te *4d* core level (lower panel). The reversed chemical contrast [123] between the two images makes it possible to directly identify the lateral variation of the Sb/Te stoichiometric ratio at the surface, and consequently the distribution of different surface terminations. In particular, the areas where the Sb/Te ratio is higher (more intensity in the upper panel and less intensity in the lower one) indicate a Sb-rich termination, while areas where the Sb/Te ratio is lower (less intensity in the Sb *4d* image and more intensity in the Te *4d* image) are typical of a Te-rich termination. In figure 5.3(d), I present a similar comparison for the Sb *4d* and Te *4d* microscopic concentration distributions within the S_2 region. Notably, we detect a microscopic area where the Sb/Te ratio is particularly high (blue in the Sb *4d* maps), considerably higher with respect to the values obtained in the region S_1.

5.3.2 μ-XPS study

The coexistence of different types of surface terminations is further confirmed by analyzing the photoemission spectra of the Sb *4d* and Te *4d* shallow core levels (figures 5.4(a) and 5.4(b)) taken from three specific points P_1, P_2 and P_3 (figures 5.3(b) and 5.3(d)), representative of the distinct microscopic termination domains. The comparison of the stoichiometric concentration becomes more straightforward by looking at the core level photoemission yield [124]: in particular, the Sb *4d*/Te *4d* intensity ratios (1.56, 2.54 and 4.86) from the regions represented by the three points P_1, P_2 and P_3 are consistent with an assignment to the three surface terminations: Te-rich QL, Sb-rich 1BL and Sb-rich 2BLs, respectively. It is worth noting that the Sb *4d* lineshape varies depending on the surface termination: we can in fact detect three components for the peak corresponding to three chemical inequivalent Sb species. The first one, at higher binding energy, corresponds to the Sb atoms embedded in the Sb_2Te_3 QL, while the other two correspond to the Sb atoms in the Sb_2 BL. Their intensity ratio varies according to their distance from the surface: in the case of Sb_2Te_3 QL termination the highest binding energy component becomes predominant, while it becomes the faintest in the case of the Sb_2 BL termination. Furthermore, a quantitative analysis of the lateral distribution of the three different terminations in the SPEM images indicates that the Te-rich termination is the dominating one when cleaving the specimen.

5.3.3 μ-ARPES study

Further information on the correlation between surface terminations and electronic properties could be obtained by operating the instrument in μ-ARPES mode. Figure 5.5 shows

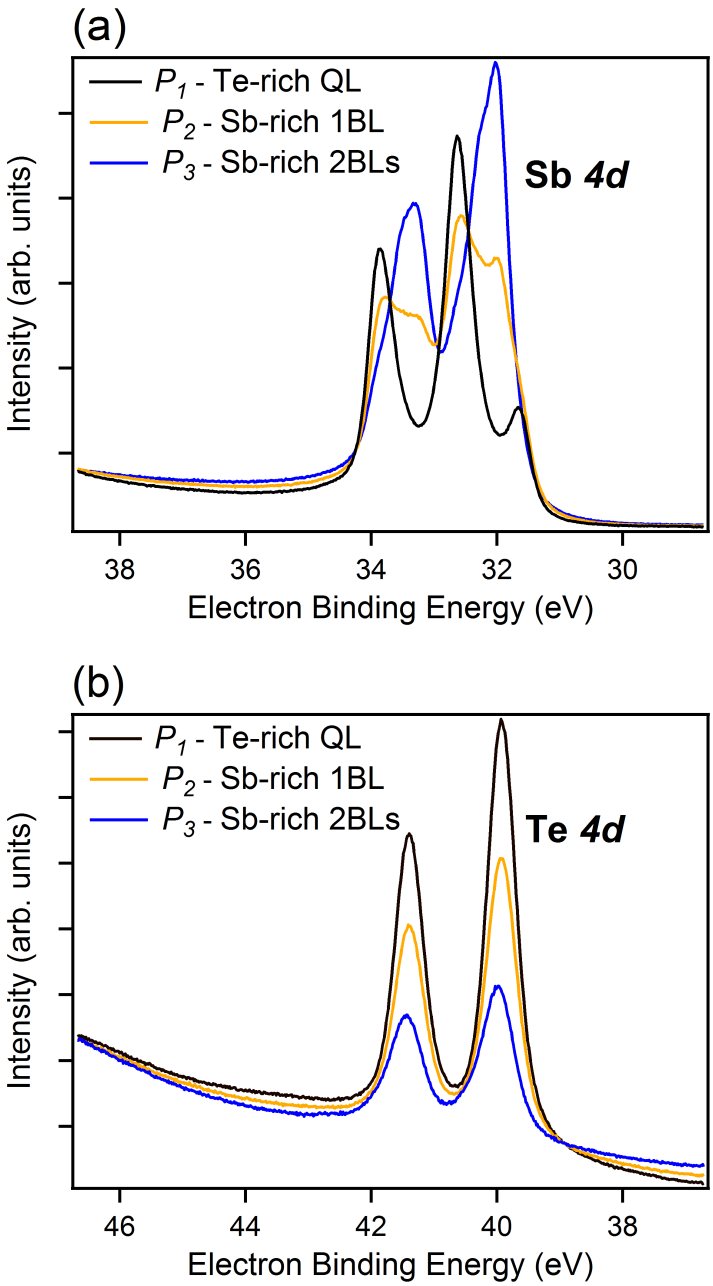

Figure 5.4: μ-XPS spectra of Sb_2Te taken at a photon energy of 74 eV. (a) and (b) are photoemission spectra of the Sb *4d* and Te *4d* core levels, obtained from points P_1, P_2 and P_3 and representative of the three coexisting terminations.

selected momentum dispersion images at different binding energies from a Sb_2Te_3 QL termination. The measured Fermi surface clearly shows the order three symmetry of Sb_2Te and makes it possible to identify the high symmetry points M and M' of the surface Brillouin zone.

In figure 5.6, I compare the photoelectron intensity maps obtained along $\overline{\Gamma M}$–$\overline{\Gamma M'}$ for

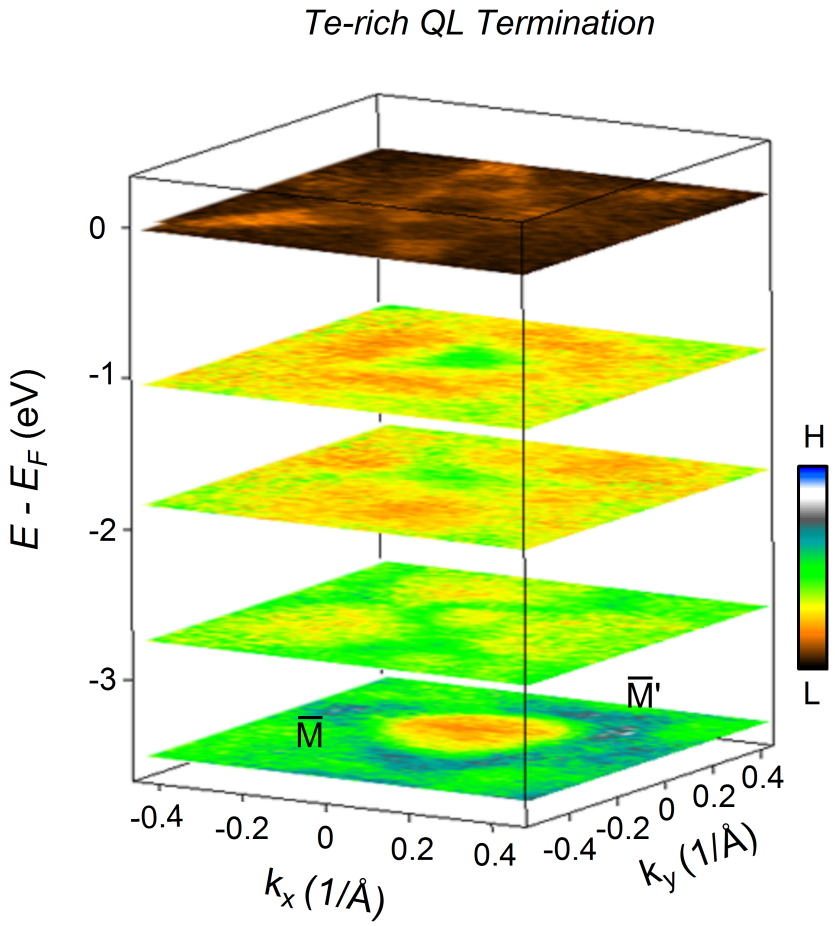

Figure 5.5: Constant energy cuts for the Te-rich termination showing the Fermi surface topography and presenting the high symmetry direction $\overline{\Gamma M}$–$\overline{\Gamma M'}$.

the three points P_1, P_2 and P_3. The μ-ARPES yields clearly indicate that the projected band structures significantly differ from one surface termination region to another: in particular, moving from the Te-rich QL to the Sb-rich 2BLs termination, we can see the bands closer to the Fermi level (E_F) becoming fainter, while the bands between 1 eV and 2 eV along $\overline{\Gamma M}$ become more intense. This could be due to the different relative weight of these states in the two sub-blocks constituting the superlattice: the former with a higher weight in the Sb_2Te_3 QL block, the latter with a higher weight in the Sb_2 BL block.

To visualize the different electronic structures in figure 5.6, I present in figure 5.7 energy distribution curves (EDCs) from the same microscopic regions and for selected wave vectors. The comparison among the EDCs is quite effective to provide a quantitative information about the different intensities of distinct spectral features in regions with various surface terminations.

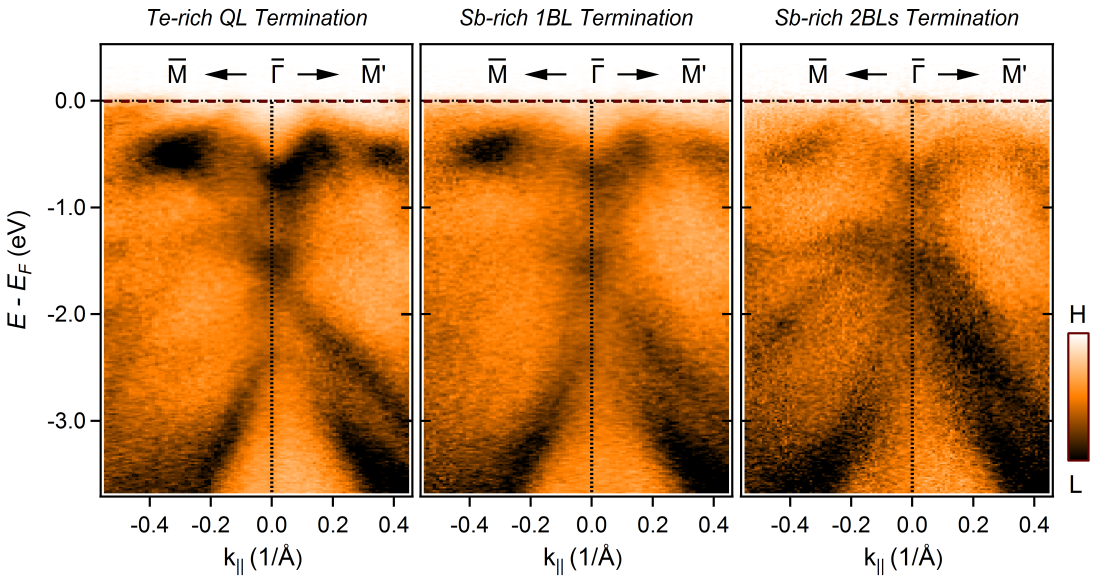

Figure 5.6: Occupied electronic band structure of Sb_2Te. Intensity maps of photoelectrons, emitted for parallel wave vector along the $\overline{\Gamma M}$–$\overline{\Gamma M'}$ direction for the three microscopic regions, corresponding to points P_1, P_2 and P_3 in figure 5.3.

5.3.4 XPS study

Apart from taking elemental and chemical maps of the surface under investigation with the analyzer tuned to a chosen photoelectron energy corresponding to a core electronic level, the other main capability of SPEM is taking EDCs from a microspot at a specific region on the surface. In the previous paragraphs, the local elemental and chemical composition of the three surface terminations was characterized by means of the two complementary operation modes of SPEM. The SPEM maps and the photoemission spectra, taken at distinct points on the three terminations, were shown in figures 5.3 and 5.4, respectively. Because it is worthwhile emphasizing the importance of the preceding Sb_2Te photoemission microscopic analysis, I performed a macroscopic XPS study to reveal that conventional XPS does not provide a precise information on each surface termination but presents an overall description of all terminated surfaces.

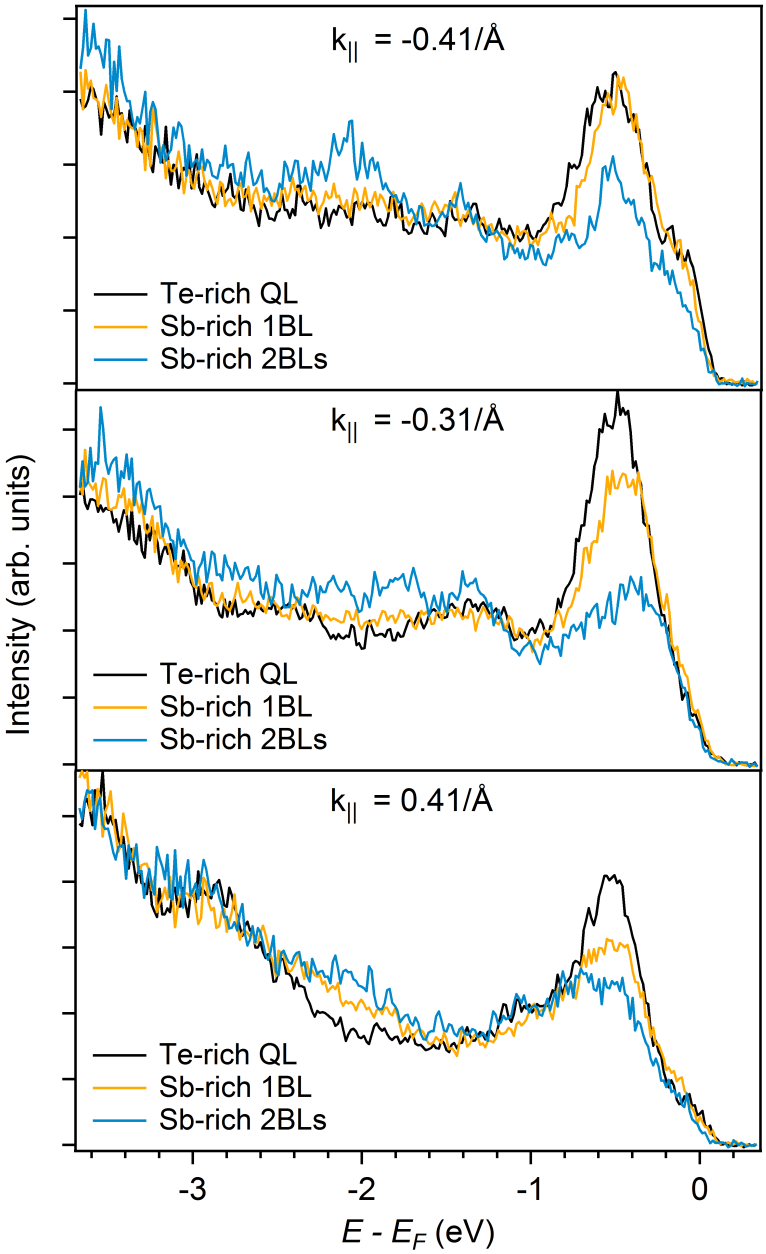

Figure 5.7: EDCs from the three same microscopic regions for k = -0.4 Å^{-1} (upper), k = -0.3 Å^{-1} (center), and k = 0.4 Å^{-1} (lower panel).

Figures 5.8, 5.9, 5.10 and 5.11 show representative Sb *4d* XPS spectra of Sb_2Te at different photon energies of 46 eV, 47 eV, 50 eV and 80 eV, respectively. The fitting components are plotted as well for each Sb *4d* XPS spectrum. The fitting of the Sb *4d* spectra was performed using a Lorentzian function convoluted with a Gaussian; where the Gaussian describes the measurement process (instrumental response, etc.), while the Lorentzian models the lifetime broadening (natural broadening) due to the uncertainty

principle relating lifetime and energy of the ejected electrons. The Lorentzian contribution to the spectral line shape produced by the lifetime broadening is given by:

$$I(E) = \frac{1}{\pi} \frac{\gamma}{(E - E_0)^2 + \gamma^2} \tag{5.1}$$

where E_0 is the center of the Lorentzian peak, γ is the hole lifetime and 2γ is the full width at half-maximum (FWHM) of the hole state Lorentzian line shape. The optimized fitting parameters are reported in each figure. Note that for all the XPS spectra, I employed a polynomial background except for the one acquired at a photon energy of 80 eV where a Shirley background was used to account for the effect of the inelastic scattering of electrons [125]. In the XPS spectrum acquired using photons with an energy of 50 eV, a secondary peak appear due to plasmon[1] excitation. To fit this peak, a Gaussian function was employed. It should also be noted that the photoemission intensity ratio between the $4d_{3/2}$ and the $4d_{5/2}$ spin orbit split states of the Sb *4d* core level, known as the branching ratio (BR), varies as a function of the photon energy and the surface termination in the measured XPS spectra. The variation of the BR has already been reported by several studies performed by Levinson *et al.* [126], Yeom *et al.* [127], Sieger *et al.* [128] and Luh *et al.* [129]. The last two studies, carried out specifically for the Sb *4d* core levels, revealed that the BR varies with respect to the emission angle, the photon energy and is also affected by the surface structure.

All the Sb *4d* spectra require four components (C1, C2, C3 and C4) to fit the XPS experimental data. As previously found in the μ-XPS study, the first component, namely C4, located at higher binding energies, is relative to the Sb atoms embedded in the Sb_2Te_3 QL. The second two components C1 and C2, at lower binding energies, correspond to the Sb atoms in the Sb_2 BL. The fourth one, C3, refers to the Sb atoms in both Sb_2Te_3 QL and Sb_2 BL. Since this study was conducted at the APE beamline with a spot size of approximately $50 \times 150\ \mu m^2$, larger than the domain size of the Sb-rich 1BL and the Sb-rich 2BLs, the core level spectra, obtained at all photon energies, were taken by averaging over a macroscopic region. For this reason, it is necessary to use μ-XPS to directly probe the appropriate surface termination and eliminate the fourth component present in all the XPS spectra, which is due to the simultaneous presence of several domains on the same cleaved surface.

According to the inelastic mean free path, described in chapter 3, the surface or bulk contributions can be enhanced or suppressed by tuning the photon energy. At 80 eV, the surface sensitivity increases. Thus, the C4 component becomes prominent because the Sb_2Te_3 QL termination is the dominating one when cleaving the crystal. Whereas, at

[1] Plasmon is a quasiparticle due to collective quantum oscillations of the free electron gas density or plasma.

lower photon energies, the bulk sensitivity becomes higher. Consequently, we also probe the Sb atoms in the Sb_2 BL and thus the photoemission intensity of the C2 component automatically increases.

To conclude, the XPS results are in good agreement with those obtained by the μ-XPS study. However, since XPS is a macroscopic photoemission technique, the provided information corresponds to an average over different sample features.

5.4 Unoccupied electronic band structure

One of the most interesting Sb_2Te features, i.e. the topological SSs, are located above E_F [3], making them inaccessible using synchrotron-based ARPES. To overcome this issue, I used trARPES: as previously mentioned in chapter 3, with this technique, pump photons excite hot electrons into the empty electronic states, giving access to the unoccupied band structure and the temporal evolution of the transient electron population. I explored various k-space directions in the surface Brillouin zone (in figure 5.12), I present results obtained at a pump-probe delay t = 0.25 ps, revealing the dispersion of the empty states: the white dashed line indicates the dispersion of the topological SSs. Also in the unoccupied bulk CB, the threefold symmetry of the occupied states is retrieved. The signal in the trARPES experiment comes mainly from the Te-rich QL termination, because the spot size of the probe beam (approximately 50 micron diameter) is considerably larger than the typical domain size for the other terminations.

In figure 5.13, I report the evolution of the ARPES yield acquired along the $\overline{\Gamma M}$–$\overline{\Gamma M'}$ high symmetry direction at various pump-probe time delays following the ultrafast optical pump excitation. The images presented here are differences between positive and negative time delays, corresponding to excess carriers (electrons in red, and holes in blue). In the upper left corner of figure 5.13, I display a schematic view of the bulk bands and the topological SSs that can be used as a guide to the eye to interpret my experimental results. Because Sb_2Te is an intrinsically p-doped semimetal, the bulk VB crosses E_F. At negative time delays—corresponding to a real delay of about 4 μs, i.e. to a complete relaxation of the system—the electronic band structure is probed in its ground state. Thus, the photoelectron intensity map taken at -0.10 ps time delay shows the topological SSs and bulk CB non occupied, at equilibrium. Immediately after the pump photo-excitation from the VB at t = 0 ps, the first transient populated feature is the CB located at $E - E_F$ = 0.5 eV. Notice that at zero delay, the topological SSs are only marginally populated, because they cannot be directly photoexcited.

To follow the relaxation processes, I studied as a function of time delay the photoemission yield from different k-E integration windows, as indicated for the t = 0.10 ps

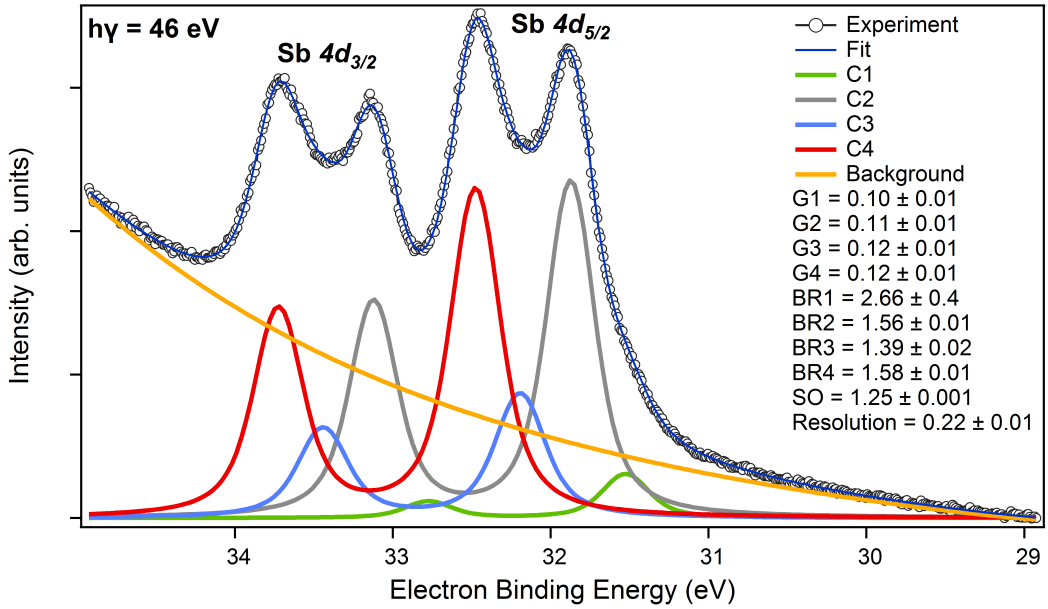

Figure 5.8: Sb *4d* core level spectrum taken at a photon energy of 46 eV. G: hole lifetime γ, BR: branching ratio, SO: spin orbit splitting.

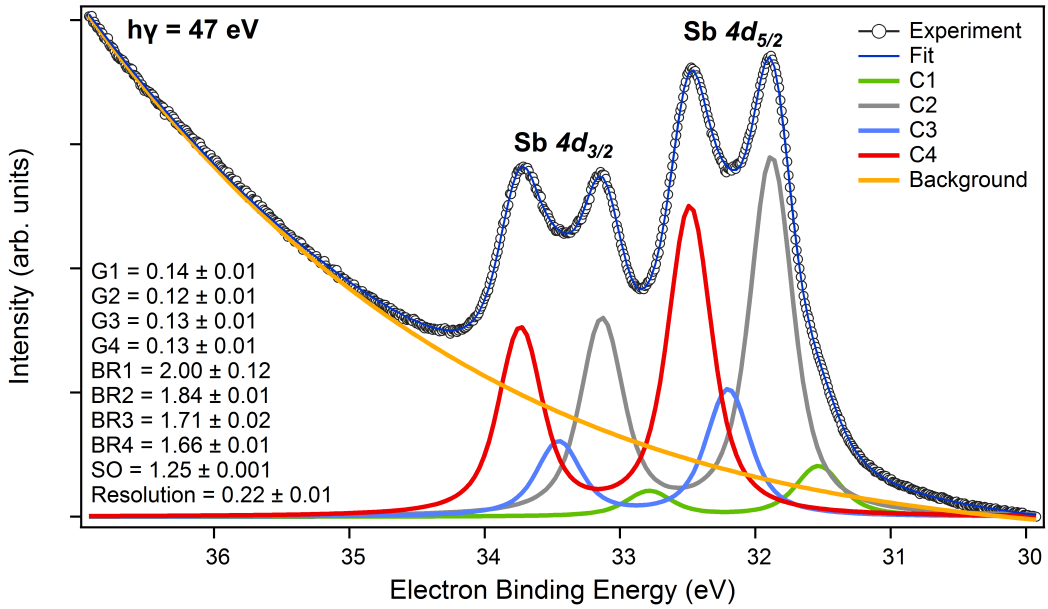

Figure 5.9: Sb *4d* core level spectrum taken at a photon energy of 47 eV.

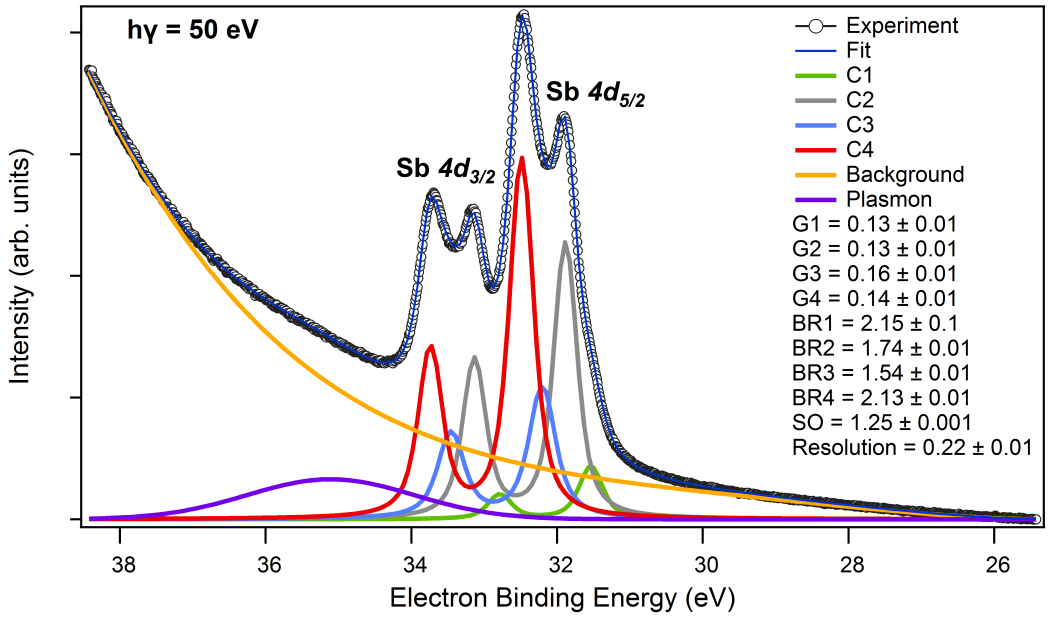

Figure 5.10: Sb *4d* core level spectrum taken at a photon energy of 50 eV.

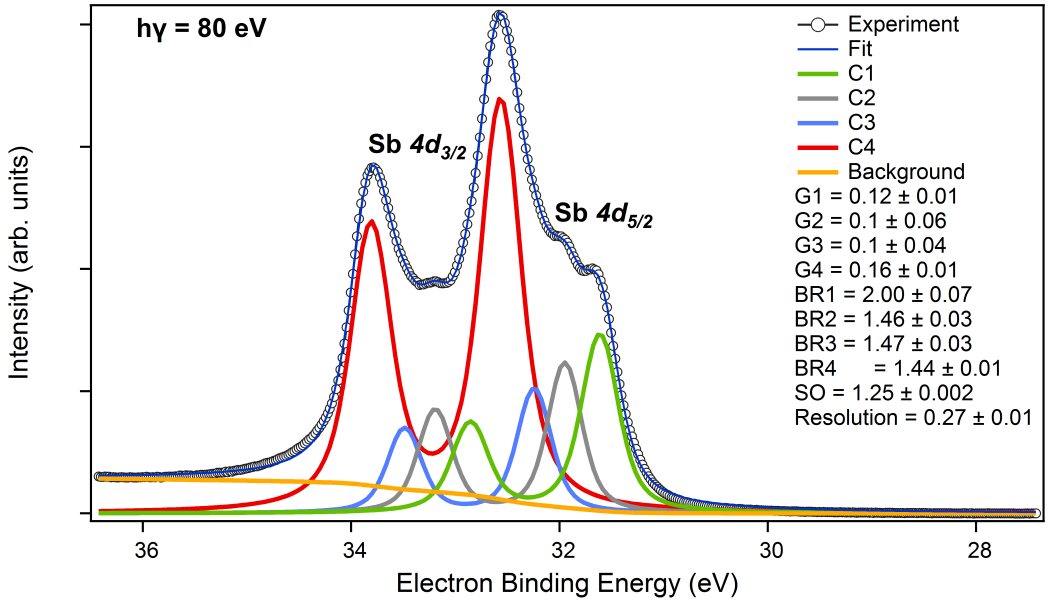

Figure 5.11: Sb *4d* core level spectrum taken at a photon energy of 80 eV.

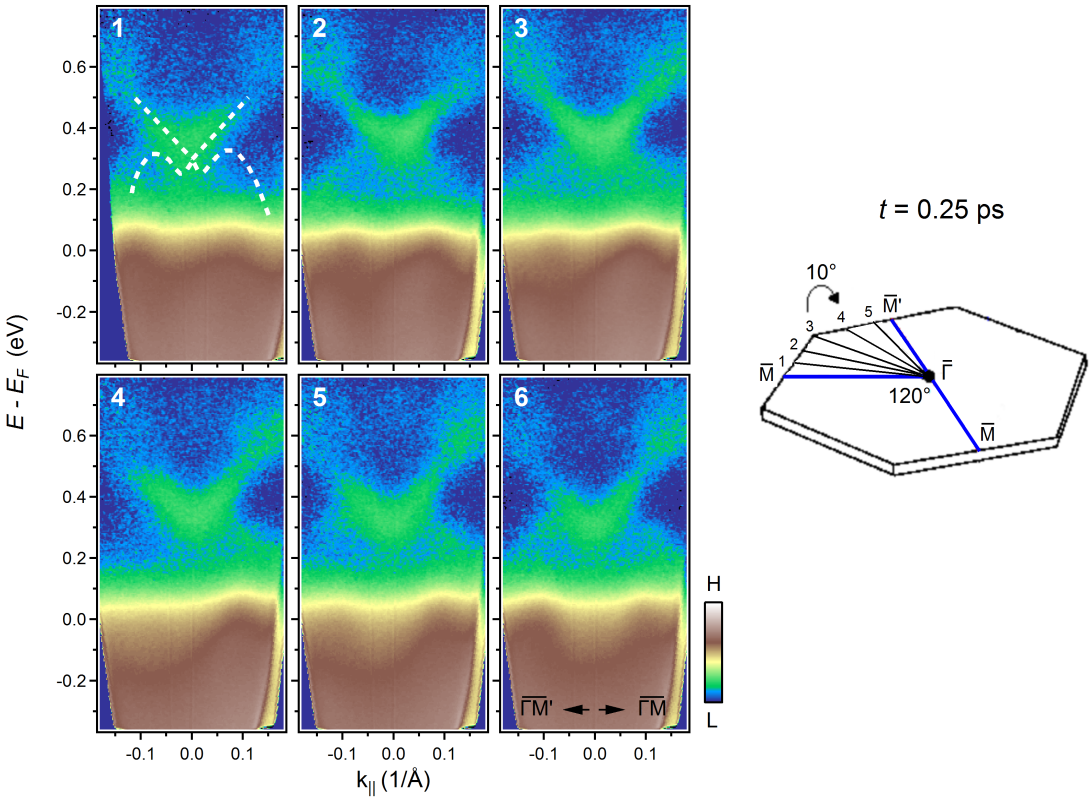

Figure 5.12: trARPES sequence acquired after photoexcitation from the pump pulses for Sb_2Te. The color intensity is presented in logarithmic scale to make the signal from the unoccupied electronic states more evident. The intensity maps have been extracted at emission angles near $\bar{\Gamma}$, every 10 degrees, at +0.25 ps pump-probe time delay.

time delay in figure 5.13, and corresponding to the unoccupied topological SSs, CB and VB, and to the occupied VB (see figure 5.14). We can clearly notice that the primary maximum of the photo-excited electron population observed in the bulk CB (for window number 1 at t = 0.10 ps) is at about 50 fs, whereas the other regions attain their maxima only later; as already found in other similar cases, the initial photoexcitation into the bulk CB triggers a cascade of intra-band and inter-band scattering processes towards low-lying states both in the bulk CB and topological SSs [39, 43].

Quantitatively, the characteristic lifetime of the excess electron population for the 1 to 8 k-E windows varies from τ_1 = 110 fs (for window CB1) to τ_8 = 330 fs (for window CB8) (these values are extracted by fitting the data with a single exponential). It takes about 150 fs for the topological SSs to reach their maximum population. The excess electrons in the topological SSs relax through the bulk VB thanks to their strong inter-band scattering processes and decay with an average lifetime of about 560 fs. It should also be pointed out that the time evolution of the excess populations in the bulk VB is very well balanced for electrons and holes at all time delays, and the characteristic decay time

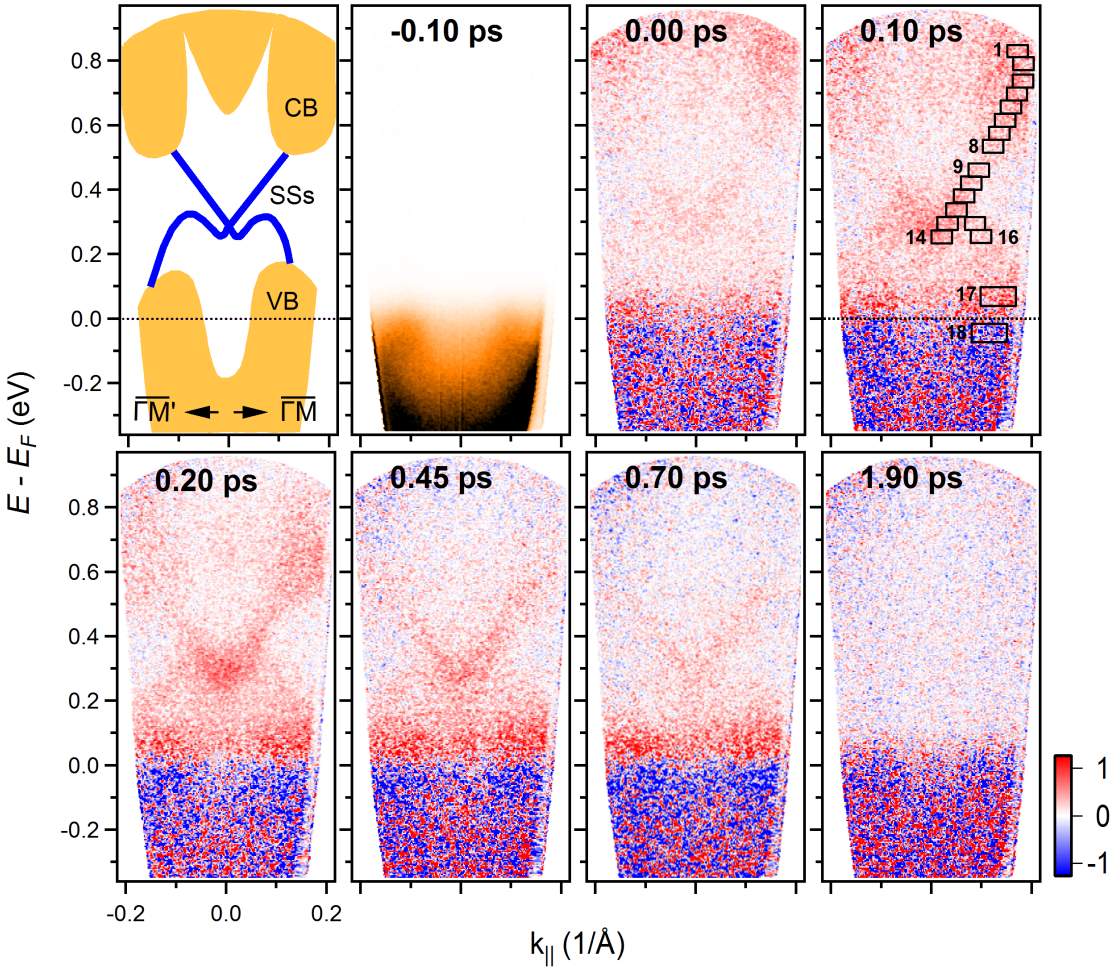

Figure 5.13: Ultrafast dynamics of the photoexcited electronic states. In the upper left corner, a schematic view of the electronic band structure of the Te-rich terminated region along $\overline{\Gamma M}$–$\overline{\Gamma M'}$ is exhibited. Excess electron (red) and hole (blue) populations are detected from the difference time-resolved ARPES images obtained after and before photoexcitation. Dashed lines indicate E_F.

for the relaxation of the bulk VB is 755 fs. As thoroughly discussed in previous studies, the relaxation of the topological SSs and bulk bands is due to various processes, including intra- and inter-band scattering, with the electron-phonon scattering playing a key role. In particular, the electron-phonon coupling seems stronger that for 3D TIs, since for this system the topological SSs do not present the markedly longer lifetime with respect to the bulk bands observed in prototype materials like Bi_2Se_3 and Bi_2Te_3 [44, 112, 116]. In fact, since this system is a semimetal, the phase space available for electrons to relax is much wider than the one available in Bi_2Se_3 and Bi_2Te_3, making possible for electrons to couple with a large number of available phonons.

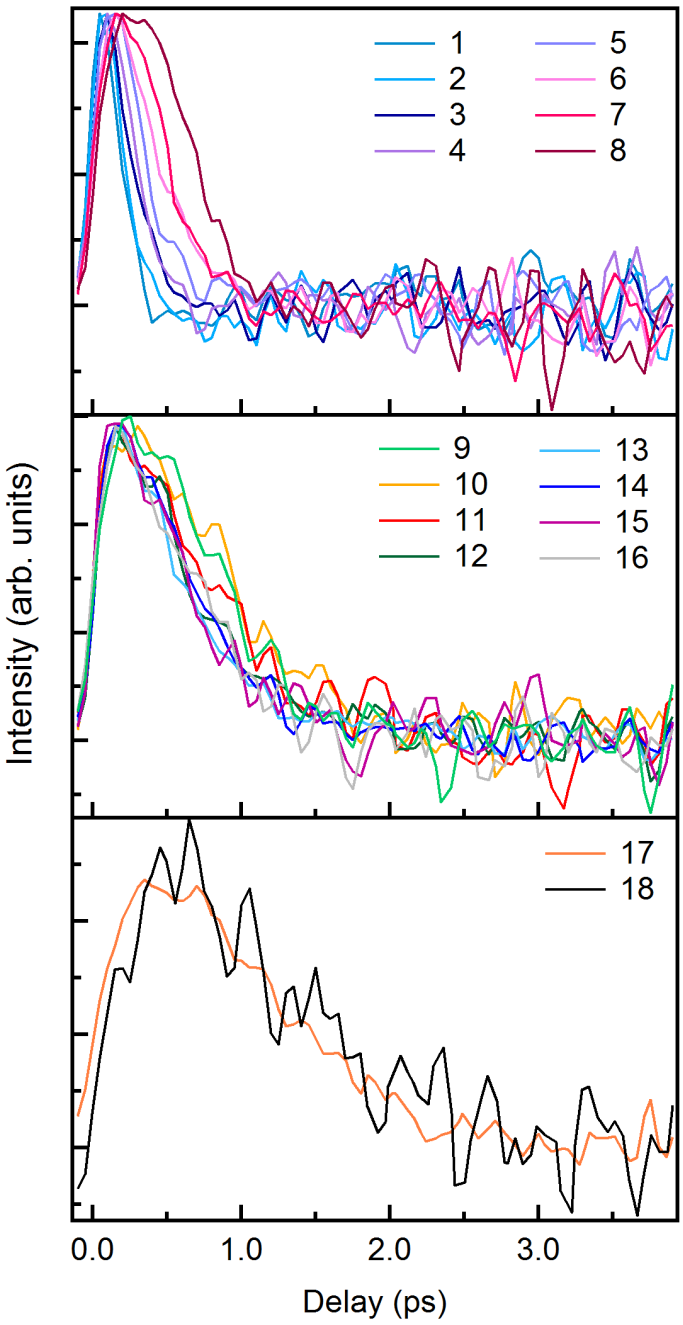

Figure 5.14: Ultrafast time evolution of the populations in the *k*-E integration windows 1 to 18 presented at $t = 0.10$ ps pump-probe delay in figure 5.13.

5.5 Bulk contribution

Since the trARPES yield is essentially representative of the Te-rich QL termination, this means that the results presented in figures 5.13 and 5.14 correspond to a Sb_2Te_3 surface slab (see figure 5.2). If one compares my data with the corresponding experimental [18,

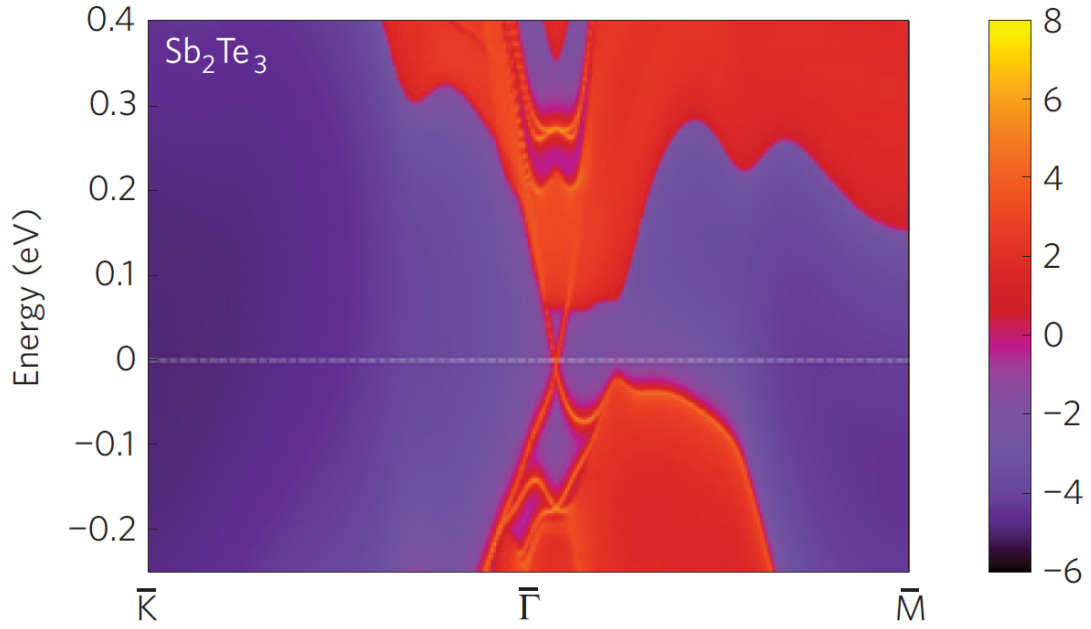

Figure 5.15: Calculated electronic band structure for Sb_2Te_3. The red regions indicate bulk energy bands and the blue regions indicate bulk energy gaps. The SSs can be clearly seen around the $\bar{\Gamma}$ point as red lines dispersing in the bulk gap. These theoretical calculations differ from my experimental data for the "Sb_2Te_3-terminated" Sb_2Te along the $\overline{\Gamma M}$ high symmetry direction, specifically for the topological SSs. From [15].

120] and theoretical data [15] for Sb_2Te_3, it is clear that the surface electronic structure of "Sb_2Te_3-terminated" Sb_2Te is markedly different from Sb_2Te_3, in particular for the topological SSs (see figure 5.15). This confirms that, as in the case of Bi_4Se_3 [121], it is the bulk band structure that determines the topological SSs, not the structure of the first QL of the host.

Furthermore, the dynamics presented in figure 5.14 indicate a strong coupling between SSs and bulk, which can be explained by a penetration depth of the Dirac state of more than a structural unit slab, consistent to what is found for prototype materials like Bi_2Te_3 [39] and more recently for other TIs like $SnSb_2Te_4$ [130]. Besides, the dynamics of figure 5.14 are obviously distinct from those of Sb_2Te_3 represented in figure 5.16(a). In fact, Zhu *et al.* [120] have described a population inversion after pumping the electrons into the unoccupied electronic states in Sb_2Te_3, i.e. the photoexcited electrons in the upper Dirac cone stay longer than those below the DP to form an inverted population (figure 5.16(b)). This is attributed to a reduced density of states near the DP due to the linear dispersion of the topological SSs which is not the case of the Te-rich termination of Sb_2Te. This proves that Sb_2Te_3-terminated surface of Sb_2Te and Sb_2Te_3 are not identical.

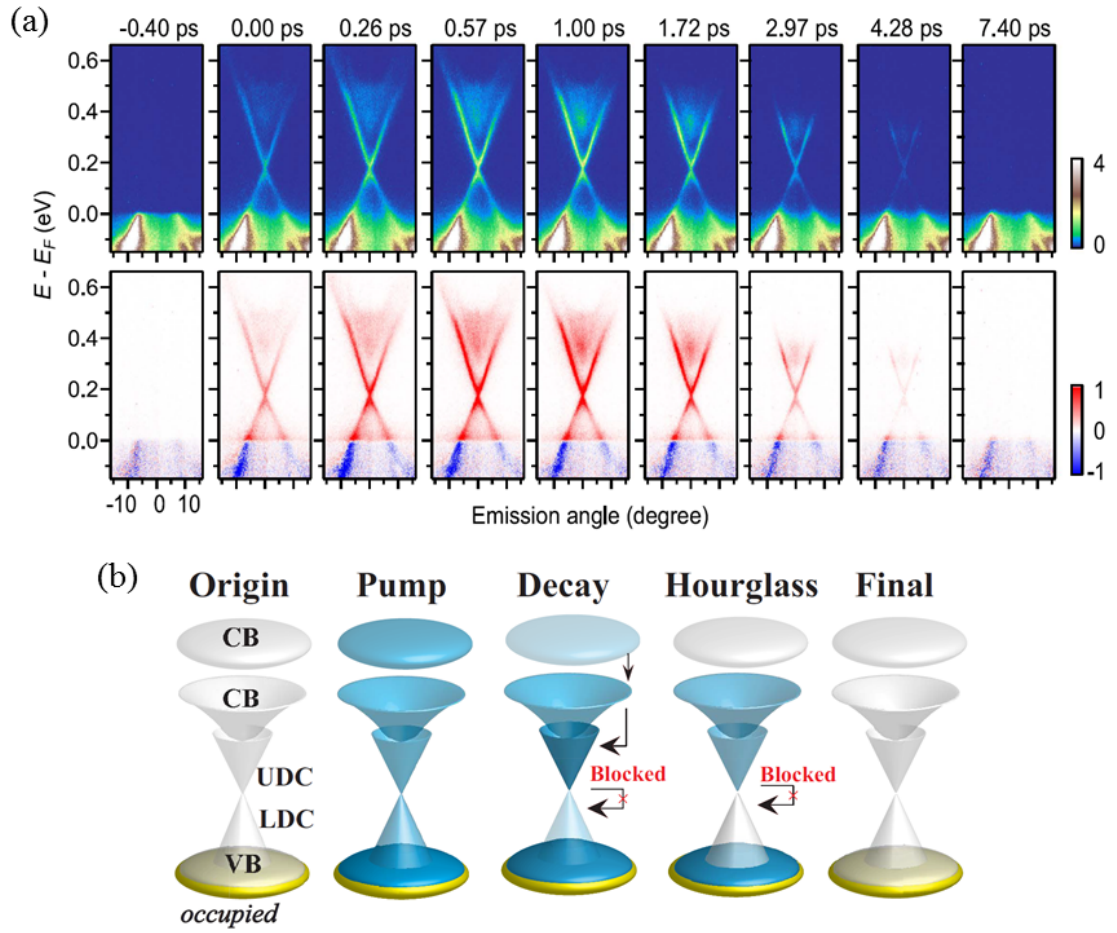

Figure 5.16: trARPES study of Sb_2Te_3 along the $\overline{\Gamma K}$ direction. (a) Upper panel shows a trARPES sequence at different temporal delays. Lower panel displays the trARPES images of difference between positif and negative delays. (b) Schematics of the pump and decay processes. An hourglass-shaped electron distribution occurs after photoexcitation. The color gradation represents the electron density. From [120].

5.6 Conclusion

In conclusion, I performed a combined μ-ARPES and trARPES study of the natural topological superlattice phase Sb_2Te. The μ-ARPES results clearly show that three distinct types of surface termination can coexist after cleaving a single crystal of this material, each one presenting a different surface and bulk band dispersion. Based on this microscopic analysis, we can also conclude that the preponderant termination is the Te-rich one, that I was able to study also by means of trARPES. The analysis of the transient electronic structure for the topological SSs and bulk bands along high symmetry directions in the Brillouin zone shows that the topological SSs of "Sb_2Te_3-terminated" Sb_2Te are considerably different from simple Sb_2Te_3, confirming that the surface properties of topological multilayers are determined by more than one structural unit. Futher theoret-

ical efforts, taking into account all these factors, are required to understand in detail the interplay between multilayer structures and surface electronic properties of this new class of topological materials.

Chapter 6

Conclusion and perspectives

The surface bands of three-dimensional topological insulators consist of a non-degenerate band of linearly dispersing surface states with a special spin texture. Stemming from these unique band properties, topological insulators constitute fascinating and promising candidates for a new generation of electronic and spintronic devices, and are triggering novel efforts to be able to tune and engineer the topological surface states band structure. In this thesis, I have used photoemission spectroscopy to investigate the electronic properties of two topological systems, namely, the irradiated three-dimensional topological insulator Bi_2Te_3 and the natural topological superlattice phase Sb_2Te. First, I have studied a series of Bi_2Te_3 compounds. The Bi_2Te_3 specimens have been irradiated by high-energy electron beams, in order to realize materials that are really insulating in the bulk required for future technological applications. Second, I have explored the electronic band structure of Sb_2Te, which is the most representative material in the topological superlattice series $(Sb_2)_m$-Sb_2Te_3 ($m = 2$). This series of topological superlattices provides a promising avenue to engineer the topological states for realizing different quantum phenomena and spintronics applications. To examine the unconventional electronic states of these two materials that could contribute to many future applications, I have employed experimental methods based on photoemission spectroscopy, which represents a powerful technique to directly visualize the electronic band structure in solids.

In the first part of this work, I have presented trARPES measurements on a series of Bi_2Te_3 crystals under several irradiation conditions. The femtosecond time, energy, and momentum resolution allows us to probe the fundamental scattering processes and the carrier relaxation dynamics in order to reveal the impact of the swift electron irradiation on the electronic properties of the irradiated materials. In this study, I have demonstrated that although the Dirac spectrum presents an electronic robustness against electron irradiation, the induced disorder affects the ultrafast relaxation times of the out-of-equilibrium transient carrier population. In fact, I have found that two dominating relaxation regimes

govern the temporal evolution of the electron population of the series: the faster one is identical for all samples, i.e. unaffected by defect generation, and is principally determined by the characteristic time of the electron-phonon scattering; the slower one (more than 10 ps) corresponds to the thermalization of the excess charge via diffusion and can be suppressed by adding disorder to the lattice. This proves that the ultrafast relaxation dynamics are very sensitive to the related modifications of the bulk properties. By modifying the irradiation parameters (projectile dose, quantity of Frenkel pair-production, dwelling time at room temperature, etc.), I conclude that we can tune the electronic dynamics, in particular those of the topological surface states. As all these parameters can be adjusted in a controlled way, they appear to be essential tools for future devices based on the photoconductive control of the Dirac fermions in the topological surface states with ultrafast light pulses.

In the second part, I have studied the effects of surface termination on the electronic structure of the natural topological superlattice phase Sb_2Te. Three observable nonequivalent regions coexisting on the same cleaved surface, specifically, a "Sb-rich 1BL" termination, a "Sb-rich 2BLs" termination and a "Te-rich QL" termination, were investigated by SPEM. These three distinct terminations are characterized by different Sb/Te surface stoichiometric ratios and have clear differences in their band structure. Based on the microscopic analysis, I have found that the preponderant termination is the Te-rich one, that I was able to study also by means of trARPES. For this dominating Te-rich termination, I have provided a direct visualization of the photoexcited electronic states and of their relaxation dynamics. The analysis of the transient electronic structure for the topological surface states and bulk bands along high symmetry directions in the Brillouin zone reveals that the surface electronic structure of "Sb_2Te_3-terminated" Sb_2Te is markedly distinct from simple Sb_2Te_3, confirming that the surface properties of topological multilayers are determined by more than one structural unit. This evidently indicates that the surface electronic structure is strongly affected by the bulk properties of the superlattice. In perspective, further ultrafast ARPES experiments, possibly with spin resolution, are required to investigate the dynamics of the topological surface states of the other two surface terminations, information of fundamental interest with important practical implications. In addition, further theoretical efforts are needed to understand in detail the interplay between multilayer structures and surface electronic properties of this new class of topological systems.

Appendix A

Résumé étendu en français

La complexité de certains matériaux se traduit par l'apparition d'états électroniques non conventionnels ayant des propriétés émergentes et fascinantes qui pourraient contribuer à répondre à des enjeux sociétaux majeurs du XXI^e siècle liés à l'électronique, l'énergie et l'environnement. La compréhension de ces systèmes complexes reste aujourd'hui un challenge pour la communauté scientifique. Pourtant, depuis le début du XX^e siècle, les propriétés électroniques des matériaux ont été au cœur des problématiques de la physique de la matière condensée et ont fait l'objet d'intenses investigations: modèle de Drude et théorie des bandes de Wigner, Seitz et Bloch. Ces propriétés font intervenir, non seulement les électrons et par là même les orbitales et les spins, mais également toutes les charges du système et plus généralement le réseau atomique. Tous ces degrés de liberté de la matière et leurs couplages sont à considérer pour comprendre les propriétés électroniques. Ceci rend le problème extrêmement complexe. Aujourd'hui, on comprend bien les propriétés des matériaux conventionnels tels que le cuivre, le silicium et le diamant, classifiés selon leurs structures de bandes en métal, semi-conducteur et isolant. Le défi maintenant est la compréhension des systèmes complexes présentant des états électroniques non conventionnels comme ceux observés en présence de fortes corrélations entre les électrons, ou encore à cause d'effets liés à la topologie.

Les états électroniques non conventionnels dans des systèmes sans corrélations électroniques sont observés en présence d'effets de surface et d'interface. Par exemple, depuis 2005, on a prédit théoriquement puis vérifié expérimentalement que certains systèmes présentent des phases "topologiques", isolantes en volume mais possédant des états métalliques de surface. Ces états de surface sont polarisés en spin, et leurs propriétés de transport sont très robustes vis-à-vis des impuretés non magnétiques. Ces systèmes sont appelés isolants topologiques et peuvent apparaître dans des matériaux massifs comme Bi_2Te_3, mais aussi dans des super-réseaux tel que Sb_2Te (voir figure A.1).

La présence de surfaces métalliques sur un isolant, avec une protection topologique

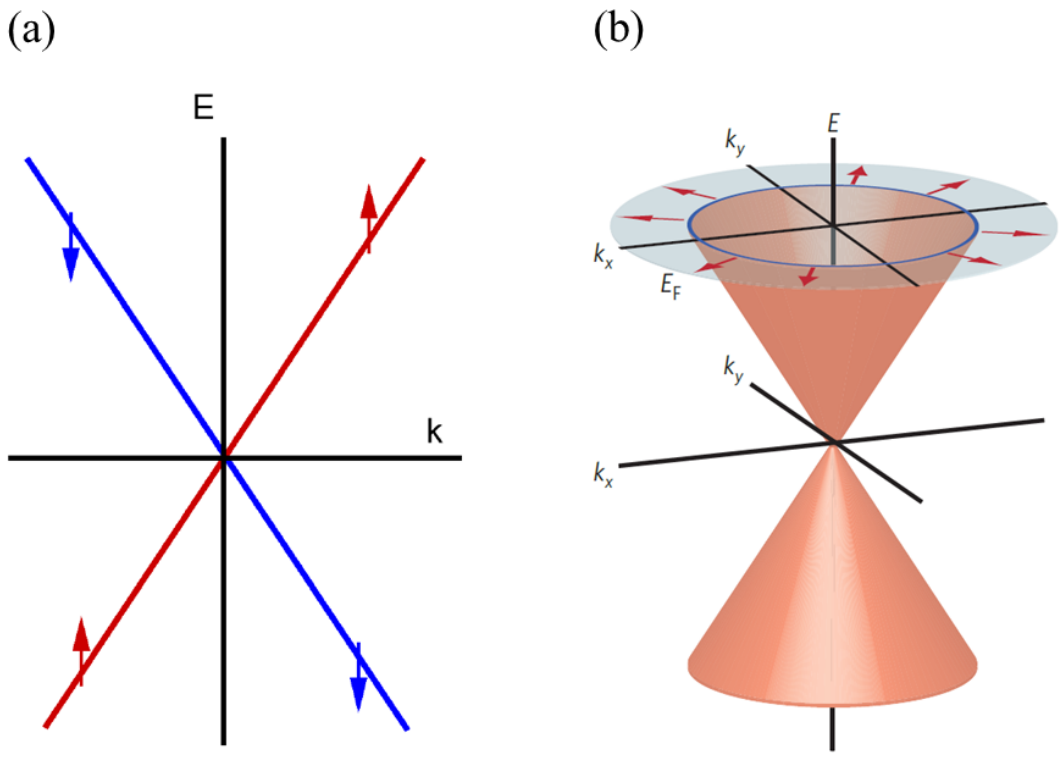

Figure A.1: Structure électronique d'un isolant topologique bidimensionnel et tridimensionnel. (a) Les états de bord se dispersent linéairement dans un isolant topologique bidimensionnel. (b) Relation de dispersion pour les états de surface bidimensionnels d'un isolant topologique tridimensionnel [1].

spéciale, constitue un phénomène nouveau qui ne se trouve pas dans d'autres matériaux. Il existe de nombreuses idées et suggestions pour de futures applications de ces surfaces métalliques en électronique, en spintronique et en information quantique [1]. Mais avant que ces applications puissent être réalisées, il faudrait répondre à de multiples questions fondamentales, et résoudre divers problèmes. Le défi principal dans l'utilisation électrique de ces surfaces est que le volume d'un isolant topologique n'est pas souvent isolant comme prévu. En raison d'une multitude de défauts cristallins électriquement actifs, le volume est la plupart du temps si conducteur que le courant électrique passe non seulement à travers les surfaces métalliques, mais à travers tout le matériau, empêchant de nombreuses applications potentielles. Ce problème est l'un des principaux défis à relever en utilisant de nouvelles approches telles que l'irradiation par des faisceaux d'électrons de haute énergie qui permet de compenser les défauts cristallins responsables de la conductivité dans le volume (voir figure A.2). Récemment, une étude expérimentale a prouvé que la conductivité du volume dans l'isolant topologique tridimensionnel Bi_2Te_3 peut être réduite de plusieurs ordres de grandeur en utilisant d'une façon contrôlée des fais-

ceaux énergétiques d'électrons (énergie de ∼2.5 MeV) [2]. Par conséquent, l'irradiation avec des faisceaux d'électrons est une approche très prometteuse pour obtenir des isolants topologiques vraiment isolants dans le volume.

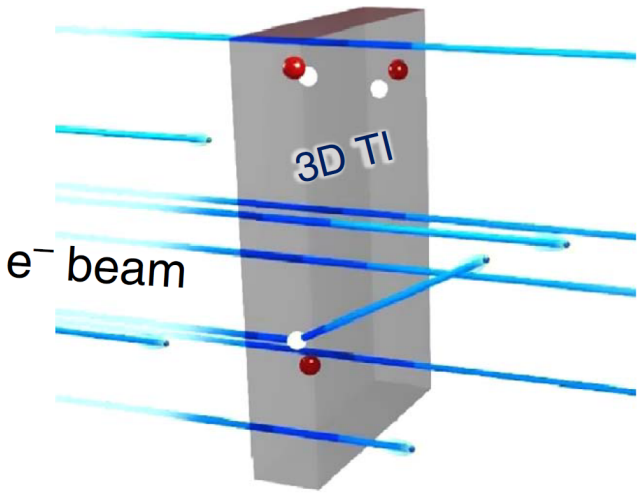

Figure A.2: Contrôle de la conductivité du volume des isolants topologiques tridimensionnels par irradiation avec des faisceaux d'électrons de haute énergie [2].

De plus, de possibles applications dépendent de la capacité de contrôler et d'élaborer la structure de bandes électronique des états de surface topologiques. Dans ce contexte, il a été proposé que des structures multicouches, constituées d'une séquence d'empilements ordonnés d'isolants topologiques avec d'autres composés, entrelacées dans un super-réseau, présentent de nouvelles propriétés topologiques. Récemment, une étude théorique et expérimentale a démontré la possibilité d'ingénierie de la structure de bandes des états de surface topologiques dans la série des super-réseaux topologiques naturels $(Sb_2)_m$-Sb_2Te_3, composée d'un empilement ordonné de nombres entiers de deux couches de Sb_2 et de cinq couches de Sb_2Te_3 [3]. Les résultats ont révélé que les états topologiques sont remarquablement robustes et que leurs dispersions peuvent être contrôlées dans toute la gamme explorée m = 0–3 (voir figure A.3). Par conséquent, ces matériaux présentent une voie intéressante pour l'ingénierie des états topologiques qui constitue une condition cruciale pour la réalisation de différents phénomènes quantiques et applications spintroniques.

Le travail de cette thèse vise à étudier les états électroniques non conventionnels de deux matériaux topologiques, notamment l'isolant topologique irradié Bi_2Te_3 et le super-réseau topologique naturel Sb_2Te, qui constitue le matériau le plus représentatif de la série de super-réseaux topologiques $(Sb_2)_m$-Sb_2Te_3 (m = 2). Les deux systèmes ont été étudiés par des techniques basées sur la spectroscopie de photoémission qui représente une méthode expérimentale puissante pour visualiser directement la structure de bandes électron-

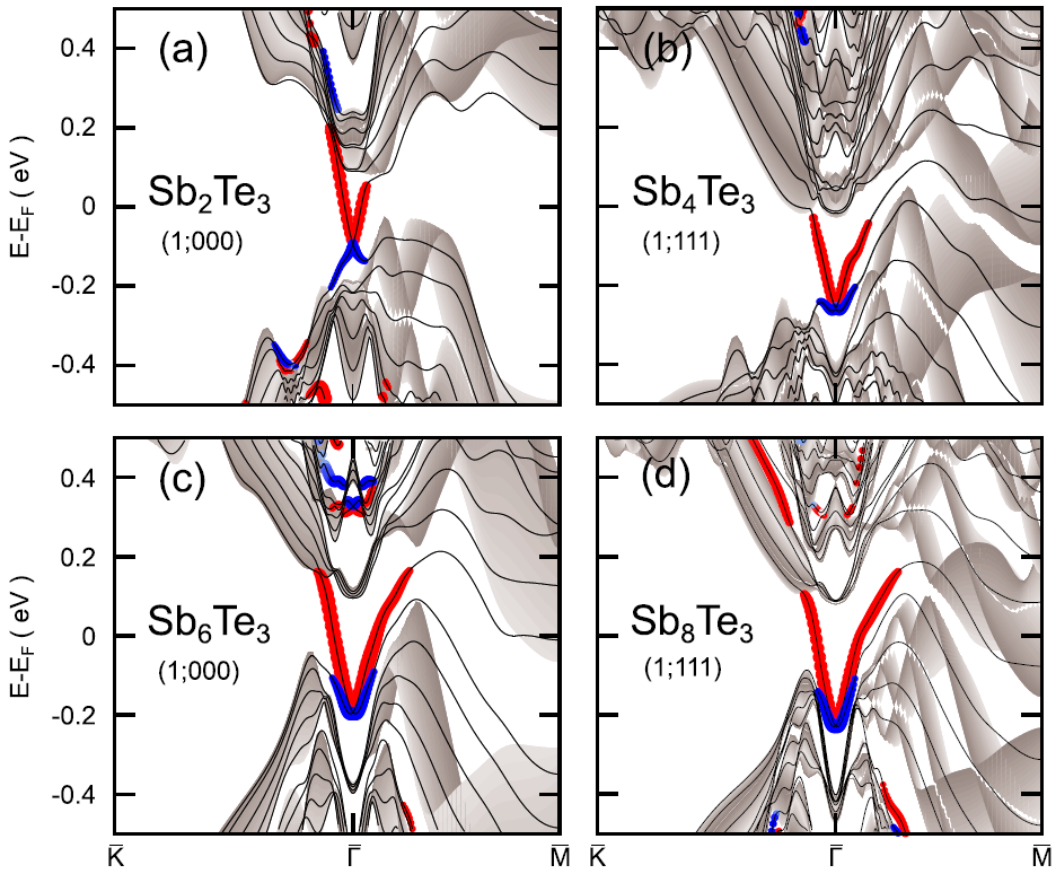

Figure A.3: Transition d'une phase semi-conductrice à une phase semi-métallique dans la série de super-réseaux topologiques naturels $(Sb_2)_m$-Sb_2Te_3 (m = 0–3). (a)–(d) Premiers calculs théoriques de la structure de bandes électronique de cette série [3].

ique dans les solides. Dans cette thèse, je présente une étude de photoémission principalement via deux techniques: la première est la spectroscopie de photoémission résolue en temps et en angle (trARPES) utilisée pour étudier les états de surface topologiques inoccupés de l'isolant topologique irradié Bi_2Te_3 et du super-réseau Sb_2Te; la seconde est la microscopie de photoémission d'électrons à balayage (SPEM) utilisée pour analyser l'hétérogénéité de la surface clivée du Sb_2Te en comparant les structures électroniques de diverses régions possédant des terminaisons différentes à la surface. En outre, la spectroscopie de photoémission des rayons X (XPS) a été également employée pour sonder les niveaux de cœur du Sb_2Te afin de révéler l'importance de l'étude SPEM.

Dans la première partie de ce travail de thèse, je présente des mesures trARPES sur une série de cristaux de Bi_2Te_3 dans plusieurs conditions d'irradiation. La résolution en temps, en énergie et en moment permet de sonder les processus fondamentaux de diffusion et la dynamique de relaxation des porteurs, afin de révéler l'impact de l'irradiation électronique sur les propriétés électroniques des matériaux irradiés. Dans cette étude je

démontre que, bien que le spectre de Dirac présente une robustesse électronique envers l'irradiation par des électrons, le désordre induit affecte les temps de relaxation ultra-rapides de la population des porteurs transitoire hors d'équilibre. En fait, deux régimes de relaxation dominants régissent l'évolution temporelle de la population d'électrons de la série: le premier est le régime rapide qui est commun pour tous les échantillons, autrement dit, il n'est pas affecté par la génération de défauts et est principalement déterminé par la diffusion électron-phonon; le second est le régime lent (qui dure plus que 10 ps) correspondant à la thermalisation de l'excès des charges par diffusion et peut être supprimé en ajoutant un désordre au réseau. Cela prouve que la dynamique de relaxation ultra-rapide est très sensible aux modifications liées aux propriétés du volume. En modifiant les paramètres d'irradiation (dose des projectiles, quantité de production des paires de Frenkel, temps au cours duquel les échantillons irradiés sont gardés à température ambiante, etc.), je conclus que nous pouvons ajuster les dynamiques électroniques, en particulier celles des états de surface topologiques. Comme tous ces paramètres peuvent être ajustés d'une manière contrôlée, ils semblent être des outils essentiels pour de futurs dispositifs basés sur le contrôle photoconducteur des fermions de Dirac dans les états de surface topologiques avec des impulsions de lumière ultra-rapides.

Dans la deuxième partie de cette thèse, les effets des terminaisons de surface sur la structure de bandes électronique du super-réseau topologique naturel Sb_2Te ont été étudiés. Trois régions non équivalentes, spécifiquement, une terminaison riche en antimoine présentant un empilement de deux couches de Sb_2, une terminaison riche en antimoine avec deux empilements de deux couches de Sb_2, et une terminaison riche en tellure formée d'un empilement de cinq couches de Sb_2Te_3, ont été observées simultanément sur la même surface clivée et ont été étudiées par SPEM. Ces trois terminaisons distinctes sont caractérisées par des rapports stœchiométriques de surface Sb/Te différents et présentent des différences claires dans leurs structures de bandes. Sur la base de l'analyse microscopique, je trouve que la terminaison prépondérante est celle qui est riche en tellure, que j'ai pu étudier aussi en utilisant la technique trARPES. Pour cette terminaison dominante riche en tellure, je fourni une visualisation directe des états électroniques photoexcités et de leurs dynamiques de relaxation. L'analyse de la structure électronique transitoire des états de surface topologiques et des bandes de volume le long des directions de haute symétrie dans la zone de Brillouin révèle que la structure électronique de surface du Sb_2Te riche en tellure est nettement distincte de celle du Sb_2Te_3, confirmant que les propriétés des multicouches sont déterminées par plus d'une unité structurelle. Ceci indique évidemment que la structure électronique de surface est fortement affectée par les propriétés de volume du super-réseau. En perspective, d'autres expériences ARPES ultra-rapides, éventuellement résolues en spin, sont nécessaires pour étudier la

dynamique des états de surface topologiques des deux autres terminaisons de surface, donnant des informations d'intérêt fondamental avec des implications pratiques importantes. En outre, d'autres efforts théoriques sont nécessaires pour comprendre en détail l'interaction entre les structures multicouches et les propriétés électroniques de surface de cette nouvelle classe de systèmes topologiques.

Bibliography

[1] J. E. Moore. The birth of topological insulators. *Nature*, 464:194–198, 2010.

[2] L. Zhao, M. Konczykowski, H. Deng, I. Korzhovska, M. Begliarbekov, Z. Chen, E. Papalazarou, M. Marsi, L. Perfetti, A. Hruban, A. Wołoś, and L. Krusin-Elbaum. Stable topological insulators achieved using high energy electron beams. *Nat. Commun.*, 7:10957, 2016.

[3] J. C. Johannsen, G. Autès, A. Crepaldi, S. Moser, B. Casarin, F. Cilento, M. Zacchigna, H. Berger, A. Magrez, Ph. Bugnon, J. Avila, M. C. Asensio, F. Parmigiani, O. V. Yazyev, and M. Grioni. Engineering the topological surface states in the $(Sb_2)_m$-Sb_2Te_3 (m = 0–3) superlattice series. *Phys. Rev. B*, 91(20):201101(R), 2015.

[4] P. W. Anderson. *Basic Notions of Condensed Matter Physics*. Westview Press/Addison-Wesley, 1997.

[5] S. Rachel. Interacting Topological Insulators: a review. *arXiv*, 2018.

[6] K. v. Klitzing, G. Dorda, and M. Pepper. New Method for High-Accuracy Determination of the Fine-Structure Constant Based on Quantized Hall Resistance. *Phys. Rev. Lett.*, 45(6):494–497, 1980.

[7] D. J. Thouless, M. Kohmoto, M. P. Nightingale, and M. den Nijs. Quantized Hall Conductance in a Two-Dimensional Periodic Potential. *Phys. Rev. Lett.*, 49(6):405–408, 1982.

[8] X.-L. Qi and S.-C. Zhang. Topological insulators and superconductors. *Rev. Mod. Phys.*, 83(4):1057–1110, 2011.

[9] F. D. M. Haldane. Model for a Quantum Hall Effect without Landau Levels: Condensed-Matter Realization of the "Parity Anomaly". *Phys. Rev. Lett.*, 61(18):2015–2018, 1988.

[10] B. A. Bernevig and S.-C. Zhang. Quantum Spin Hall Effect. *Phys. Rev. Lett.*, 96(10):106802, 2006.

[11] B. A. Bernevig, T. L. Hughes, and S.-C. Zhang. Quantum Spin Hall Effect and Topological Phase Transition in HgTe Quantum Wells. *Science (80-.).*, 314(5806):1757–1761, 2006.

[12] M. König, S. Wiedmann, C. Brüne, A. Roth, H. Buhmann, L. W. Molenkamp, X.-L. Qi, and S.-C. Zhang. Quantum Spin Hall Insulator State in HgTe Quantum Wells. *Science (80-.).*, 318(5851):766–770, 2007.

[13] L. Fu and C. L. Kane. Topological insulators with inversion symmetry. *Phys. Rev. B*, 76(4):045302, 2007.

[14] D. Hsieh, D. Qian, L. Wray, Y. Xia, Y. S. Hor, R. J. Cava, and M. Z. Hasan. A topological Dirac insulator in a quantum spin Hall phase. *Nature*, 452:970–974, 2008.

[15] H. Zhang, C.-X. Liu, X.-L. Qi, X. Dai, Z. Fang, and S.-C. Zhang. Topological insulators in Bi_2Se_3, Bi_2Te_3 and Sb_2Te_3 with a single Dirac cone on the surface. *Nat. Phys.*, 5:438–442, 2009.

[16] Y. Xia, D. Qian, D. Hsieh, L. Wray, A. Pal, H. Lin, A. Bansil, D. Grauer, Y. S. Hor, R. J. Cava, and M. Z. Hasan. Observation of a large-gap topological-insulator class with a single Dirac cone on the surface. *Nat. Phys.*, 5:398–402, 2009.

[17] Y. L. Chen, J. G. Analytis, J.-H. Chu, Z. K. Liu, S.-K. Mo, X. L. Qi, H. J. Zhang, D. H. Lu, X. Dai, Z. Fang, S. C. Zhang, I. R. Fisher, Z. Hussain, and Z.-X. Shen. Experimental Realization of a Three-Dimensional Topological Insulator, Bi_2Te_3. *Science (80-.).*, 325(5937):178–181, 2009.

[18] J. Reimann, J. Güdde, K. Kuroda, E. V. Chulkov, and U. Höfer. Spectroscopy and dynamics of unoccupied electronic states of the topological insulators Sb_2Te_3 and Sb_2Te_2S. *Phys. Rev. B*, 90(8):081106(R), 2014.

[19] D. C. Tsui. Nobel Lecture: Interplay of disorder and interaction in two-dimensional electron gas in intense magnetic fields. *Rev. Mod. Phys.*, 71(4):891–895, 1999.

[20] B. I. Halperin. Quantized Hall conductance, current-carrying edge states, and the existence of extended states in a two-dimensional disordered potential. *Phys. Rev. B*, 25(4):2185–2190, 1982.

[21] M. Büttiker. Absence of backscattering in the quantum Hall effect in multiprobe conductors. *Phys. Rev. B*, 38(14):9375–9389, 1988.

[22] S. Murakami. Phase transition between the quantum spin Hall and insulator phases in 3D: emergence of a topological gapless phase. *New J. Phys.*, 9:356, 2007.

[23] X.-L. Qi and S.-C. Zhang. The quantum spin Hall effect and topological insulators. *Phys. Today*, 63(1):33–38, 2010.

[24] J. Maciejko, T. L. Hughes, and S.-C. Zhang. The Quantum Spin Hall Effect. *Annu. Rev. Condens. Matter Phys.*, 2:31–53, 2011.

[25] C. L. Kane and E. J. Mele. Z_2 Topological Order and the Quantum Spin Hall Effect. *Phys. Rev. Lett.*, 95(14):146802, 2005.

[26] R. Roy. Z_2 classification of quantum spin Hall systems: An approach using time-reversal invariance. *Phys. Rev. B*, 79(19):195321, 2009.

[27] M. Z. Hasan and C. L. Kane. Colloquium: Topological insulators. *Rev. Mod. Phys.*, 82(4):3045–3067, 2010.

[28] C. L. Kane and E. J. Mele. Quantum Spin Hall Effect in Graphene. *Phys. Rev. Lett.*, 95(22):226801, 2005.

[29] Y. Yao, F. Ye, X.-L. Qi, S.-C. Zhang, and Z. Fang. Spin-orbit gap of graphene: First-principles calculations. *Phys. Rev. B*, 75(4):041401(R), 2007.

[30] A. Roth, C. Brüne, H. Buhmann, L. W. Molenkamp, J. Maciejko, X.-L. Qi, and S.-C. Zhang. Nonlocal Transport in the Quantum Spin Hall State. *Science (80-.).*, 325(5938):294–297, 2009.

[31] M. König, H. Buhmann, L. W. Molenkamp, T. Hughes, C.-X. Liu, X.-L. Qi, and S.-C. Zhang. The Quantum Spin Hall Effect: Theory and Experiment. *J. Phys. Soc. Japan*, 77(3):031007, 2008.

[32] E. G. Novik, A. Pfeuffer-Jeschke, T. Jungwirth, V. Latussek, C. R. Becker, G. Landwehr, H. Buhmann, and L. W. Molenkamp. Band structure of semimagnetic $Hg_{1-y}Mn_yTe$ quantum wells. *Phys. Rev. B*, 72(3):035321, 2005.

[33] L. Fu, C. L. Kane, and E. J. Mele. Topological Insulators in Three Dimensions. *Phys. Rev. Lett.*, 98(10):106803, 2007.

[34] J. E. Moore and L. Balents. Topological invariants of time-reversal-invariant band structures. *Phys. Rev. B*, 75(12):121306(R), 2007.

[35] D. Hsieh, Y. Xia, L. Wray, D. Qian, A. Pal, J. H. Dil, J. Osterwalder, F. Meier, G. Bihlmayer, C. L. Kane, Y. S. Hor, R. J. Cava, and M. Z. Hasan. Observation of Unconventional Quantum Spin Textures in Topological Insulators. *Science (80-.).*, 323(5916):919–922, 2009.

[36] P. Roushan, J. Seo, C. V. Parker, Y. S. Hor, D. Hsieh, D. Qian, A. Richardella, M. Z. Hasan, R. J. Cava, and A. Yazdani. Topological surface states protected from backscattering by chiral spin texture. *Nature*, 460:1106–1109, 2009.

[37] C. Howard, M. El-Batanouny, R. Sankar, and F. C. Chou. Anomalous behavior in the phonon dispersion of the (001) surface of Bi_2Te_3 determined from helium atom-surface scattering measurements. *Phys. Rev. B*, 88(3):035402, 2013.

[38] Y. Feutelais, B. Legendre, N. Rodier, and V. Agafonov. A study of the phases in the bismuth - tellurium system. *Mater. Res. Bull.*, 28(6):591–596, 1993.

[39] M. Hajlaoui, E. Papalazarou, J. Mauchain, G. Lantz, N. Moisan, D. Boschetto, Z. Jiang, I. Miotkowski, Y. P. Chen, A. Taleb-Ibrahimi, L. Perfetti, and M. Marsi. Ultrafast Surface Carrier Dynamics in the Topological Insulator Bi_2Te_3. *Nano Lett.*, 12(7):3532–3536, 2012.

[40] H.-J. Noh, H. Koh, S.-J. Oh, J.-H. Park, H.-D. Kim, J. D. Rameau, T. Valla, T. E. Kidd, P. D. Johnson, Y. Hu, and Q. Li. Spin-orbit interaction effect in the electronic structure of Bi_2Te_3 observed by angle-resolved photoemission spectroscopy. *Europhys. Lett.*, 81(5):57006, 2008.

[41] D. Hsieh, Y. Xia, D. Qian, L. Wray, J. H. Dil, F. Meier, J. Osterwalder, L. Patthey, J. G. Checkelsky, N. P. Ong, A. V. Fedorov, H. Lin, A. Bansil, D. Grauer, Y. S. Hor, R. J. Cava, and M. Z. Hasan. A tunable topological insulator in the spin helical Dirac transport regime. *Nature*, 460:1101–1105, 2009.

[42] S. R. Park, W. S. Jung, Chul Kim, D. J. Song, C. Kim, S. Kimura, K. D. Lee, and N. Hur. Quasiparticle scattering and the protected nature of the topological states in a parent topological insulator Bi_2Se_3. *Phys. Rev. B*, 81(4):041405(R), 2010.

[43] J. A. Sobota, S. Yang, J. G. Analytis, Y. L. Chen, I. R. Fisher, P. S. Kirchmann, and Z.-X. Shen. Ultrafast Optical Excitation of a Persistent Surface-State Population in the Topological Insulator Bi_2Se_3. *Phys. Rev. Lett.*, 108(11):117403, 2012.

[44] J. A. Sobota, S.-L. Yang, A. F. Kemper, J. J. Lee, F. T. Schmitt, W. Li, R. G. Moore, J. G. Analytis, I. R. Fisher, P. S. Kirchmann, T. P. Devereaux, and Z.-X. Shen.

Direct Optical Coupling to an Unoccupied Dirac Surface State in the Topological Insulator Bi_2Se_3. *Phys. Rev. Lett.*, 111(13):136802, 2013.

[45] A. Crepaldi, B. Ressel, F. Cilento, M. Zacchigna, C. Grazioli, H. Berger, Ph. Bugnon, K. Kern, M. Grioni, and F. Parmigiani. Ultrafast photodoping and effective Fermi-Dirac distribution of the Dirac particles in Bi_2Se_3. *Phys. Rev. B*, 86(20):205133, 2012.

[46] A. Crepaldi, F. Cilento, B. Ressel, C. Cacho, J. C. Johannsen, M. Zacchigna, H. Berger, Ph. Bugnon, C. Grazioli, I. C. E. Turcu, E. Springate, K. Kern, M. Grioni, and F. Parmigiani. Evidence of reduced surface electron-phonon scattering in the conduction band of Bi_2Se_3 by nonequilibrium ARPES. *Phys. Rev. B*, 88(12):121404(R), 2013.

[47] C. Cacho, A. Crepaldi, M. Battiato, J. Braun, F. Cilento, M. Zacchigna, M. C. Richter, O. Heckmann, E. Springate, Y. Liu, S. S. Dhesi, H. Berger, Ph. Bugnon, K. Held, M. Grioni, H. Ebert, K. Hricovini, J. Minár, and F. Parmigiani. Momentum-Resolved Spin Dynamics of Bulk and Surface Excited States in the Topological Insulator Bi_2Se_3. *Phys. Rev. Lett.*, 114(9):097401, 2015.

[48] S. Hüfner. *Very High Resolution Photoelectron Spectroscopy*, volume 715. Springer-Verlag Berlin Heidelberg, 2007.

[49] H. Hertz. Ueber einen Einfluss des ultravioletten Lichtes auf die electrische Entladung. *Ann. Phys.*, 267(8):983–1000, 1887.

[50] A. Einstein. Über einen die Erzeugung und Verwandlung des Lichtes betreffenden heuristischen Gesichtspunkt. *Ann. Phys.*, 322(6):132–148, 1905.

[51] H.-S. Huang, W.-Y. Chan, W.-B. Su, G. Hoffmann, and C.-S. Chang. Measurement of work function difference between Pb/Si(111) and Pb/Ge/Si(111) by high-order Gundlach oscillation. *J. Appl. Phys.*, 114(21):214308, 2013.

[52] Y.-W. Chung. *Practical guide to surface science and spectroscopy*, volume 1. Academic Press, 2001.

[53] A. Damascelli. Probing the Electronic Structure of Complex Systems by ARPES. *Phys. Scr.*, T109:61–74, 2004.

[54] W. S. Lee, I. M. Vishik, D. H. Lu, and Z.-X. Shen. A brief update of angle-resolved photoemission spectroscopy on a correlated electron system. *J. Phys. Condens. Matter*, 21(16):164217, 2009.

[55] S. Mathias, L. Miaja-Avila, M. M. Murnane, H. Kapteyn, M. Aeschlimann, and M. Bauer. Angle-resolved photoemission spectroscopy with a femtosecond high harmonic light source using a two-dimensional imaging electron analyzer. *Rev. Sci. Instrum.*, 78(8):083105, 2007.

[56] G. L. Dakovski, Y. Li, T. Durakiewicz, and G. Rodriguez. Tunable ultrafast extreme ultraviolet source for time- and angle-resolved photoemission spectroscopy. *Rev. Sci. Instrum.*, 81(7):073108, 2010.

[57] C. L. Smallwood, C. Jozwiak, W. Zhang, and A. Lanzara. An ultrafast angle-resolved photoemission apparatus for measuring complex materials. *Rev. Sci. Instrum.*, 83(12):123904, 2012.

[58] F. Barbo, M. Bertolo, A. Bianco, G. Cautero, S. Fontana, T. K. Johal, S. La Rosa, G. Margaritondo, and K. Kaznacheyev. Spectromicroscopy beamline at ELETTRA: Performances achieved at the end of commissioning. *Rev. Sci. Instrum.*, 71(1):5–10, 2000.

[59] M. K. Abyaneh, L. Gregoratti, M. Amati, M. Dalmiglio, and M. Kiskinova. Scanning Photoelectron Microscopy: a Powerful Technique for Probing Micro and Nano-Structures. *e-Journal Surf. Sci. Nanotechnol.*, 9:158–162, 2011.

[60] S. Hagström, C. Nordling, and K. Siegbahn. Electron Spectroscopic Determination of the Chemical Valence State. *Zeitschrift für Phys.*, 178(5):439–444, 1964.

[61] C. Nordling, S. Hagström, and K. Siegbahn. Application of Electron Spectroscopy to Chemical Analysis. *Zeitschrift für Phys.*, 178(5):433–438, 1964.

[62] J. G. Jenkin, R. C. G. Leckey, and J. Liesegang. The development of x-ray photoelectron spectroscopy: 1900–1960. *J. Electron Spectros. Relat. Phenomena*, 12(1):1–35, 1977.

[63] S. Leadley, L.-A. O'Hare, and C. McMillan. Surface Analysis of Silicones. In *Silicone Surf. Sci.*, chapter 12. Springer Netherlands, 2012.

[64] T. A. Carlson. *Photoelectron and Auger Spectroscopy*. Springer US, 1975.

[65] C. D. Wagner, W. M. Riggs, L. E. Davis, J. F. Moulder, and G. E. Muilenberg. *Handbook of X-ray Photoelectron Spectroscopy: A Reference Book of Standard Data for Use in X-ray Photoelectron Spectroscopy*. Perkin-Elmer, 1979.

[66] D. K. Schroder. *Semiconductor Material and Device Characterization*. Wiley-IEEE Press; Third Edition, 2006.

[67] J. F. Watts and J. Wolstenholme. *An Introduction to Surface Analysis by XPS and AES*. Wiley, 2003.

[68] K. W. Kolasinski. *Surface Science: Foundations of Catalysis and Nanoscience*. John Wiley and Sons, 2012.

[69] A. Balerna and S. Mobilio. Introduction to Synchrotron Radiation. In *Synchrotron Radiat. Basics, Methods Appl.*, chapter 1. Springer-Verlag Berlin Heidelberg, 2015.

[70] H. Wiedemann. *Synchrotron Radiation*. Springer-Verlag Berlin Heidelberg, 2003.

[71] C. Bigi, P. K. Das, D. Benedetti, F. Salvador, D. Krizmancic, R. Sergo, A. Martin, G. Panaccione, G. Rossi, J. Fujii, and I. Vobornik. Very efficient spin polarization analysis (VESPA): New exchange scattering-based setup for spin-resolved ARPES at APE-NFFA beamline at Elettra. *J. Synchrotron Radiat.*, 24(4):750–756, 2017.

[72] G. D. Mahan. Theory of photoemission in simple metals. *Phys. Rev. B*, 2(11):4334–4350, 1970.

[73] A. Damascelli, Z. Hussain, and Z.-X. Shen. Angle-resolved photoemission studies of the cuprate superconductors. *Rev. Mod. Phys.*, 75(2):473–541, 2003.

[74] M. Lindroos and A. Bansil. Surface States and Angle-Resolved Photoemission Spectra from $Nd_{2-x}Ce_xCuO_4$ Superconductor. *Phys. Rev. Lett.*, 75(6):1182–1185, 1995.

[75] M. Lindroos and A. Bansil. A Novel Direct Method of Fermi Surface Determination Using Constant Initial Energy Angle-Scanned Photoemission Spectroscopy. *Phys. Rev. Lett.*, 77(14):2985–2988, 1996.

[76] A. Bansil and M. Lindroos. Importance of Matrix Elements in the ARPES Spectra of BISCO. *Phys. Rev. Lett.*, 83(24):5154–5157, 1999.

[77] C. N. Berglund and W. E. Spicer. Photoemission Studies of Copper and Silver: Theory. *Phys. Rev.*, 136(4A):A1030–A1044, 1964.

[78] P. J. Feibelman and D. E. Eastman. Photoemission spectroscopy-Correspondence between quantum theory and experimental phenomenology. *Phys. Rev. B*, 10(12):4932–4947, 1974.

[79] B. Feuerbacher and R. F. Willis. Photoemission and electron states at clean surfaces. *J. Phys. C Solid State Phys.*, 9(2):169–216, 1976.

[80] S. Hüfner. *Photoelectron Spectroscopy: Principles and Applications*, volume 82. Springer-Verlag Berlin Heidelberg, 2003.

[81] M. P. Seah and W. A. Dench. Quantitative electron spectroscopy of surfaces: A standard data base for electron inelastic mean free paths in solids. *Surf. Interface Anal.*, 1(1):2–11, 1979.

[82] H. Lüth. *Solid Surfaces, Interfaces and Thin Films*. Springer; Fifth Edition, 2010.

[83] R. Matzdorf. Investigation of line shapes and line intensities by high-resolution UV-photoemission spectroscopy — Some case studies on noble-metal surfaces. *Surf. Sci. Rep.*, 30(4-5):153–206, 1998.

[84] M. Hajlaoui, E. Papalazarou, J. Mauchain, Z. Jiang, I. Miotkowski, Y. P. Chen, A. Taleb-Ibrahimi, L. Perfetti, and M. Marsi. Time resolved ultrafast ARPES for the study of topological insulators: The case of Bi_2Te_3. *Eur. Phys. J. Spec. Top.*, 222(5):1271–1275, 2013.

[85] M. H. Berntsen, O. Götberg, and O. Tjernberg. An experimental setup for high resolution 10.5 eV laser-based angle-resolved photoelectron spectroscopy using a time-of-flight electron analyzer. *Rev. Sci. Instrum.*, 82(9):095113, 2011.

[86] L. Perfetti, P. A. Loukakos, M. Lisowski, U. Bovensiepen, H. Berger, S. Biermann, P. S. Cornaglia, A. Georges, and M. Wolf. Time Evolution of the Electronic Structure of 1T-TaS_2 through the Insulator-Metal Transition. *Phys. Rev. Lett.*, 97(6):067402, 2006.

[87] J. Faure, J. Mauchain, E. Papalazarou, W. Yan, J. Pinon, M. Marsi, and L. Perfetti. Full characterization and optimization of a femtosecond ultraviolet laser source for time and angle-resolved photoemission on solid surfaces. *Rev. Sci. Instrum.*, 83(4):043109, 2012.

[88] A. Borsutzky, R. Brünger, Ch. Huang, and R. Wallenstein. Harmonic and Sum-Frequency Generation of Pulsed Laser Radiation in BBO, LBO, and KD*P. *Appl. Phys. B*, 52(1):55–62, 1991.

[89] E. Papalazarou, J. Faure, J. Mauchain, M. Marsi, A. Taleb-Ibrahimi, I. Reshetnyak, A. van Roekeghem, I. Timrov, N. Vast, B. Arnaud, and L. Perfetti. Coherent Phonon Coupling to Individual Bloch States in Photoexcited Bismuth. *Phys. Rev. Lett.*, 108(25):256808, 2012.

[90] S. K. Sundaram and E. Mazur. Inducing and probing non-thermal transitions in semiconductors using femtosecond laser pulses. *Nat. Mater.*, 1:217–224, 2002.

[91] J. P. Callan. Ultrafast Dynamics and Phase Changes in Solids Excited by Femtosecond Laser Pulses. *PhD Thesis, Harvard Univ. Cambridge, MA*, 2000.

[92] R. Haight. Electron dynamics at surfaces. *Surf. Sci. Rep.*, 21(8):275–325, 1995.

[93] I. Lovas, W. Santy, E. Spiller, R. Tibbetts, and J. Wilczynski. Design and assembly of a high resolution schwarzschild microscope for soft x rays. *High Resolut. Soft X-Ray Opt. Proc. SPIE*, 316:90–97, 1981.

[94] S. Suga and A. Sekiyama. *Photoelectron Spectroscopy: Bulk and Surface Electronic Structures*, volume 176. Springer-Verlag Berlin Heidelberg, 2014.

[95] P. Dudin, P. Lacovig, C. Fava, E. Nicolini, A. Bianco, G. Cautero, and A. Barinov. Angle-resolved photoemission spectroscopy and imaging with a submicrometre probe at the SPECTROMICROSCOPY-3.2L beamline of Elettra. *J. Synchrotron Radiat.*, 17(4):445–450, 2010.

[96] J. Moore. Topological insulators: The next generation. *Nat. Phys.*, 5:378–380, 2009.

[97] M. Fruchart and D. Carpentier. An introduction to topological insulators. *Comptes Rendus Phys.*, 14(9–10):779–815, 2013.

[98] A. Bansil, H. Lin, and T. Das. Colloquium: Topological band theory. *Rev. Mod. Phys.*, 88(2):021004, 2016.

[99] D. Hsieh, Y. Xia, D. Qian, L. Wray, F. Meier, J. H. Dil, J. Osterwalder, L. Patthey, A. V. Fedorov, H. Lin, A. Bansil, D. Grauer, Y. S. Hor, R. J. Cava, and M. Z. Hasan. Observation of Time-Reversal-Protected Single-Dirac-Cone Topological-Insulator States in Bi_2Te_3 and Sb_2Te_3. *Phys. Rev. Lett.*, 103(14):146401, 2009.

[100] J. Seo, P. Roushan, H. Beidenkopf, Y. S. Hor, R. J. Cava, and A. Yazdani. Transmission of topological surface states through surface barriers. *Nature*, 466:343–346, 2010.

[101] D. O. Scanlon, P. D. C. King, R. P. Singh, A. De La Torre, S. McKeown Walker, G. Balakrishnan, F. Baumberger, and C. R. A. Catlow. Controlling Bulk Conductivity in Topological Insulators: Key Role of Anti-Site Defects. *Adv. Mater.*, 24(16):2154–2158, 2012.

[102] J. G. Analytis, R. D. McDonald, S. C. Riggs, J.-H. Chu, G. S. Boebinger, and I. R. Fisher. Two-dimensional Dirac fermions in a topological insulator. *Nat. Phys.*, 6:960–964, 2010.

[103] N. P. Butch, K. Kirshenbaum, P. Syers, A. B. Sushkov, G. S. Jenkins, H. D. Drew, and J. Paglione. Strong surface scattering in ultrahigh-mobility Bi_2Se_3 topological insulator crystals. *Phys. Rev. B*, 81(24):241301(R), 2010.

[104] M. Caputo, M. Panighel, S. Lisi, L. Khalil, G. Di Santo, E. Papalazarou, A. Hruban, M. Konczykowski, L. Krusin-Elbaum, Z. S. Aliev, M. B. Babanly, M. M. Otrokov, A. Politano, E. V. Chulkov, A. Arnau, V. Marinova, P. K. Das, J. Fujii, I. Vobornik, L. Perfetti, A. Mugarza, A. Goldoni, and M. Marsi. Manipulating the Topological Interface by Molecular Adsorbates: Adsorption of Co-Phthalocyanine on Bi_2Se_3. *Nano Lett.*, 16(6):3409–3414, 2016.

[105] J. G. Checkelsky, Y. S. Hor, M.-H. Liu, D.-X. Qu, R. J. Cava, and N. P. Ong. Quantum Interference in Macroscopic Crystals of Nonmetallic Bi_2Se_3. *Phys. Rev. Lett.*, 103(24):246601, 2009.

[106] D. Kong, J. C. Randel, H. Peng, J. J. Cha, S. Meister, K. Lai, Y. Chen, Z.-X. Shen, H. C. Manoharan, and Y. Cui. Topological Insulator Nanowires and Nanoribbons. *Nano Lett.*, 10(1):329–333, 2010.

[107] D. Kim, S. Cho, N. P. Butch, P. Syers, K. Kirshenbaum, S. Adam, J. Paglione, and M. S. Fuhrer. Surface conduction of topological Dirac electrons in bulk insulating Bi_2Se_3. *Nat. Phys.*, 8:459–463, 2012.

[108] Z. Chen, L. Zhao, K. Park, T. A. Garcia, M. C. Tamargo, and L. Krusin-Elbaum. Robust Topological Interfaces and Charge Transfer in Epitaxial Bi_2Se_3/II-VI Semiconductor Superlattices. *Nano Lett.*, 15(10):6365–6370, 2015.

[109] L. Khalil, E. Papalazarou, M. Caputo, N. Nilforoushan, L. Perfetti, A. Taleb-Ibrahimi, V. Kandyba, A. Barinov, Q. D. Gibson, R. J. Cava, and M. Marsi. Electronic band structure for occupied and unoccupied states of the natural topological superlattice phase Sb_2Te. *Phys. Rev. B*, 95(8):085118, 2017.

[110] V. N. Brudnyi, S. N. Grinyaev, and V. E. Stepanov. Local neutrality conception: Fermi level pinning in defective semiconductors. *Phys. B Condens. Matter*, 212(4):429–435, 1995.

[111] M. Marsi, L. Nahon, M. E. Couprie, D. Garzella, T. Hara, R. Bakker, M. Billardon, A. Delboulbé, G. Indlekofer, and A. Taleb-Ibrahimi. Surface photovoltage in semiconductors under pulsed optical excitation, and its relevance to synchrotron radiation spectroscopy. *J. Electron Spectros. Relat. Phenomena*, 94(1-2):149–157, 1998.

[112] M. Hajlaoui, E. Papalazarou, J. Mauchain, L. Perfetti, A. Taleb-Ibrahimi, F. Navarin, M. Monteverde, P. Auban-Senzier, C. R. Pasquier, N. Moisan, D. Boschetto, M. Neupane, M. Z. Hasan, T. Durakiewicz, Z. Jiang, Y. Xu, I. Miotkowski, Y. P. Chen, S. Jia, H. W. Ji, R. J. Cava, and M. Marsi. Tuning a Schottky barrier in a photoexcited topological insulator with transient Dirac cone electron-hole asymmetry. *Nat. Commun.*, 5:3003, 2014.

[113] J. A. Sobota, S.-L. Yang, D. Leuenberger, A. F. Kemper, J. G. Analytis, I. R. Fisher, P. S. Kirchmann, T. P. Devereaux, and Z.-X. Shen. Ultrafast electron dynamics in the topological insulator Bi_2Se_3 studied by time-resolved photoemission spectroscopy. *J. Electron Spectros. Relat. Phenomena*, 195:249–257, 2014.

[114] M. Neupane, S.-Y. Xu, Y. Ishida, S. Jia, B. M. Fregoso, C. Liu, I. Belopolski, G. Bian, N. Alidoust, T. Durakiewicz, V. Galitski, S. Shin, R. J. Cava, and M. Z. Hasan. Gigantic Surface Lifetime of an Intrinsic Topological Insulator. *Phys. Rev. Lett.*, 115(11):116801, 2015.

[115] H. Luo, Q. Gibson, J. Krizan, and R. J. Cava. Ferromagnetism in Mn-doped Sb_2Te. *J. Phys. Condens. Matter*, 26(20):206002, 2014.

[116] Y. Wang, F. Xiu, L. Cheng, L. He, M. Lang, J. Tang, X. Kou, X. Yu, X. Jiang, Z. Chen, J. Zou, and K. L. Wang. Gate-Controlled Surface Conduction in Na-Doped Bi_2Te_3 Topological Insulator Nanoplates. *Nano Lett.*, 12(3):1170–1175, 2012.

[117] A. A. Burkov and L. Balents. Weyl Semimetal in a Topological Insulator Multilayer. *Phys. Rev. Lett.*, 107(12):127205, 2011.

[118] H. Jin, J. Im, J.-H. Song, and A. J. Freeman. Multiple Dirac fermions from a topological insulator and graphene superlattice. *Phys. Rev. B*, 85(4):045307, 2012.

[119] V. Agafonov, N. Rodier, R. Céolin, R. Bellissent, C. Bergman, and J. P. Gaspard. Structure of Sb_2Te. *Acta Crystallogr. Sect. C Struct. Chem.*, C47:1141–1143, 1991.

[120] S. Zhu, Y. Ishida, K. Kuroda, K. Sumida, M. Ye, J. Wang, H. Pan, M. Taniguchi, S. Qiao, S. Shin, and A. Kimura. Ultrafast electron dynamics at the Dirac node of the topological insulator Sb_2Te_3. *Sci. Rep.*, 5:13213, 2015.

[121] Q. D. Gibson, L. M. Schoop, A. P. Weber, H. Ji, S. Nadj-Perge, I. K. Drozdov, H. Beidenkopf, J. T. Sadowski, A. Fedorov, A. Yazdani, T. Valla, and R. J. Cava. Termination-dependent topological surface states of the natural superlattice phase Bi_4Se_3. *Phys. Rev. B*, 88(8):081108(R), 2013.

[122] G. Lantz, M. Hajlaoui, E. Papalazarou, V. L. R. Jacques, A. Mazzotti, M. Marsi, S. Lupi, M. Amati, L. Gregoratti, L. Si, Z. Zhong, and K. Held. Surface Effects on the Mott-Hubbard Transition in Archetypal V_2O_3. *Phys. Rev. Lett.*, 115(23):236802, 2015.

[123] L. Gregoratti, S. Günther, J. Kovaĉ, M. Marsi, R. J. Phaneuf, and M. Kiskinova. Ni/Si(111) system: Formation and evolution of two- and three-dimensional phases studied by spectromicroscopy. *Phys. Rev. B*, 59(3):2018–2024, 1999.

[124] M. Marsi, L. Casalis, L. Gregoratti, S. Günther, A. Kolmakov, J. Kovac, D. Lonza, and M. Kiskinova. ESCA Microscopy at ELETTRA: what it is like to perform spectromicroscopy experiments on a third generation synchrotron radiation source. *J. Electron Spectros. Relat. Phenomena*, 84(1-3):73–83, 1997.

[125] D. A. Shirley. High-Resolution X-Ray Photoemission Spectrum of the Valence Bands of Gold. *Phys. Rev. B*, 5(12):4709–4714, 1972.

[126] H. J. Levinson, I. T. McGovern, and T. Gustafsson. Photoelectron studies of the xenon 5p branching ratio using synchrotron radiation. *J. Phys. B At. Mol. Phys.*, 13(2):253–258, 1980.

[127] H. W. Yeom, T. Abukawa, Y. Takakuwa, S. Fujimori, T. Okane, Y. Ogura, T. Miura, S. Sato, A. Kakizaki, and S. Kono. Anisotropy of the spin-orbit branching ratio in angle-resolved photoemission from adsorbate layers. *Surf. Sci.*, 395(2–3):L236–L241, 1998.

[128] M. T. Sieger, T. Miller, and T.-C. Chiang. Site-Dependent Fine Structure in Photoemission Branching Ratios. *Phys. Rev. Lett.*, 75(10):2043–2046, 1995.

[129] D.-A. Luh, M. T. Sieger, T. Miller, and T.-C. Chiang. Sb on Si(111) studied by branching-ratio photoelectron holography. *Surf. Sci.*, 374(1-3):345–349, 1997.

[130] D. Niesner, S. Otto, V. Hermann, Th. Fauster, T. V. Menshchikova, S. V. Eremeev, Z. S. Aliev, I. R. Amiraslanov, M. B. Babanly, P. M. Echenique, and E. V. Chulkov. Bulk and surface electron dynamics in a p-type topological insulator $SnSb_2Te_4$. *Phys. Rev. B - Condens. Matter Mater. Phys.*, 89(8):081404(R), 2014.

université PARIS-SACLAY
ÉCOLE DOCTORALE
Physique en Île-de-France (EDPIF)

Titre : Etude ultra-rapide des fermions de Dirac dans les isolants topologiques

Mots clés : isolant topologique, super-réseau topologique naturel, spectroscopie de photoémission résolue en temps et en angle, microscopie de photoémission d'électrons à balayage, structure électronique, dynamiques ultra-rapides.

Résumé : Cette thèse présente une étude expérimentale des propriétés électroniques de deux matériaux topologiques, notamment l'isolant topologique tridimensionnel irradié Bi_2Te_3 et le super-réseau topologique naturel Sb_2Te. Les deux systèmes ont été étudiés par des techniques basées sur la spectroscopie de photoémission. Les composés Bi_2Te_3 ont été irradiés par des faisceaux d'électrons de haute énergie. L'irradiation avec des faisceaux d'électrons est une approche très prometteuse pour réaliser des matériaux qui sont vraiment isolants dans le volume, afin de mettre en évidence le transport quantique dans les états de surface protégés. En étudiant une série d'échantillons de Bi_2Te_3 par la technique de spectroscopie de photoémission résolue en temps et en angle (trARPES), nous montrons que les propriétés topologiques des états de surface de Dirac sont conservées après irradiation électronique, mais leurs dynamiques ultra-rapides de relaxation sont très sensibles aux modifications reliées aux propriétés du volume. De plus, nous avons étudié la structure électronique des bandes occupées et inoccupées du Sb_2Te. En utilisant la microscopie de photoémission d'électrons à balayage (SPEM), nous avons constamment trouvé diverses régions non équivalentes sur la même surface après avoir clivé plusieurs monocristaux de Sb_2Te. Nous avons pu identifier trois terminaisons distinctes caractérisées par différents rapports stœchiométriques de surface Sb/Te et possédant des différences claires dans leurs structures de bandes. Pour la terminaison dominante riche en tellure, nous avons également fourni une observation directe des états électroniques excités et de leurs dynamiques de relaxation en ayant recours à la technique trARPES. Nos résultats indiquent clairement que la structure électronique de surface est fortement affectée par les propriétés du volume du super-réseau. Par conséquent, pour les deux systèmes, nous montrons que la structure électronique de surface est absolument connectée aux propriétés du volume.

Title : Ultrafast study of Dirac fermions in topological insulators

Keywords : topological insulator, natural topological superlattice, time- and angle-resolved photoemission spectroscopy, scanning photoemission microscopy, electronic structure, ultrafast dynamics.

Abstract : This thesis presents an experimental study of the electronic properties of two topological materials, namely, the irradiated three-dimensional topological insulator Bi_2Te_3 and the natural topological superlattice phase Sb_2Te. Both systems were investigated by techniques based on photoemission spectroscopy. The Bi_2Te_3 compounds have been irradiated by high-energy electron beams. Irradiation with electron beams is a very promising approach to realize materials that are really insulating in the bulk, in order to emphasize the quantum transport in the protected surface states. By studying a series of samples of Bi_2Te_3 using time- and angle-resolved photoemission spectroscopy (trARPES) we show that, while the topological properties of the Dirac surface states are preserved after electron irradiation, their ultrafast relaxation dynamics are very sensitive to the related modifications of the bulk properties. Furthermore, we have studied the occupied and unoccupied electronic band structure of Sb_2Te. Using scanning photoemission microscopy (SPEM), we have consistently found various nonequivalent regions on the same surface after cleaving several Sb_2Te single crystals. We were able to identify three distinct terminations characterized by different Sb/Te surface stoichiometric ratios and with clear differences in their band structure. For the dominating Te-rich termination, we also provided a direct observation of the excited electronic states and of their relaxation dynamics by means of trARPES. Our results clearly indicate that the surface electronic structure is strongly affected by the bulk properties of the superlattice. Therefore, for both systems, we show that the surface electronic structure is absolutely connected to the bulk properties.

Université Paris-Saclay
Espace Technologique / Immeuble Discovery
Route de l'Orme aux Merisiers RD 128 / 91190 Saint-Aubin, France